学位論文

Studies of astro-physical properties of Ultra Luminous X-ray sources

（超高光度 X 線源の X 線スペクトルの研究）

平成２８年１２月博士（理学）申請

東京大学大学院理学系研究科
物理学専攻
小林翔悟

Abstract

Since their discovery with the *Einstein Observatory*, numerous observations of Ultra Luminous X-ray Sources (ULXs), unusually luminous X-ray point sources in arms of nearby galaxies, have been carried out with various X-ray observatories such as *Suzaku*, *XMM-Newton*, and *NuSTAR*. However, it is still unclear whether ULXs are intermediate-mass ($100 - 1000\ M_{\odot}$) black holes (BHs) shining at sub-Eddington conditions or stellar-mass ($\sim\ 10\ M_{\odot}$) BHs shining at super-Eddington luminosities. To better understand their X-ray nature in quantitative and unified way, analysis on 10 luminous ULXs in nearby galaxies were performed in this thesis.

Regardless of their strong variability in luminosities and spectral shapes, all 60 ULX spectra were successfully explained by a combination of multi-color disk model and its thermal Comptonization. None of them required additional model components for local features such as emission lines. All ULXs showed similar variability. The spectra below 1 keV were rather stable, giving low and stable absorption column densities of $N_{\rm H} = (1.0 - 5.0) \times 10^{21}$ cm^{-2}. The spectra commonly required coronae with cool electron temperature ($T_{\rm e} = 1.0 - 3.0$ keV) and large optical depth ($\tau > 10$). As the source made a transition from a spectral state with power law shaped continuum (PL state) to more luminous and convex shaped one (Disk-like state), the inner-disk temperature $T_{\rm in}$ increased from 0.2 keV to 0.9 keV.

In order to quantitatively characterize the spectral change, the temperature ratio $Q \equiv T_{\rm e}/T_{\rm in}$ was introduced. Since the difference between $T_{\rm e}$ and $T_{\rm in}$ is large in the PL-state spectra, they gave $Q > 10$, while the Disk like state showed smaller values $Q \sim 3$. Thus, the parameter successfully discriminated the two states. By plotting this Q against luminosity, critical luminosity $L_{\rm c}$, where the spectral transitions occur was determined for each source. As a result, $L_{\rm c}$ scattered over an order of magnitude among the ULX sample. Assuming that $L_{\rm c}$ corresponds to a particular Eddington ratio, like in the BH binaries, this suggests that the masses of the present ULXs also distribute over similarly wide range. This provide a model-independent argument that the most massive ULXs possibly have $\sim 100\ M_{\odot}$, without regard to whether they are super-Eddington or sub-Eddington objects.

Compared to Galactic X-ray binaries with high mass companions, ULX spectra are considerably featureless and less absorbed. Although this can be explained if the surrounding materials are completely ionized due to high illumination from the central objects, such a condition would not be realized in super-critical accretion flows wherein the matter emissivity is low. Therefore a new accretion picture that avoids the presence of surrounding thick materials is required. Combining the observational facts, as a possibility, ULXs could be interpreted as isolated intermediate-mass ($> 100\ M_{\odot}$) BHs, spanning a wide range in their mass, accreting directly from dense interstellar media via Bondi-Hoyle-Lyttleton accretion.

Contents

List of Figures

1 INTRODUCTION

Since the discovery of Cygnus X-1, now more than 20 X-ray sources in our Galaxy are categorized as mass exchanging binaries which harbor stellar mass ($< 20\ M_\odot$) black holes (BHs). In addition to that, it turned out that super-massive ($10^{5-9}\ M_\odot$) BHs exist at the core of almost all galaxies, and their formation has been one of the biggest mysteries in astrophysics. The most natural ways of explaining the formation of such massive BHs are to assume repeated mergers of lighter BHs, and/or their growth via copious mass accretion. If these are the cases, we should expect a population of BHs with intermediate masses ($100 - 1000\ M_\odot$). Although such BHs are still speculative objects, the epic detection of the first gravitational wave event GW150914 with the Laser Interferometer Gravitational-Wave Observatory (LIGO) clearly showed the existence of BHs which are considerably heavier than the ordinary stellar-mass BHs ($\sim 60\ M_\odot$; Abbot et al. 2016), and suggests that such massive BHs are wandering the space with a larger number than has been expected.

In 1978, the *Einstein observatory* found several strong X-ray sources at off-center regions of nearby spiral galaxies (Fabbiano and Trinchieri 1987). Since their luminosities 10^{39-41} erg sec^{-1} exceed the Eddington limit of neutron stars or ordinary stellar mass BHs, they became good candidates for the missing intermediate mass BHs. However, the nature of the sources remained a mystery, since the formation of such massive BHs were unknown at that time (although it is still not clear).

By the launch of the *ASCA* observatory, wide band ($0.5 - 10$ keV) X-ray spectroscopy with higher energy resolution became available, which gave better understandings to the nature of the enigmatic sources. The X-ray spectra of the sources were well explained by multi-color disk (MCD; Mitsuda et al. 1984) black body emissions from standard accretion disks with inner radius temperature of $T_{\rm in} \sim 1$ keV, which strongly suggests that the sources are BHs, although the temperature was rather high to be considered as intermediate mass BHs. To explain their high $T_{\rm in}$ Makishima et al. (2000) interpreted this as emissions from accretion disks around highly spinning intermediate mass BHs, which allows the inner-most stable circular orbit to be closer than the Schwarzschild BHs. Further more, Makishima et al. (2000) gave a nomenclature of Ultra Luminous X-ray sources (ULXs) to these objects.

As the observations made progress, ULXs were found to show spectral transitions, like in ordinary BH binaries, to a power-law (PL) shaped spectral state. However, unlike the BHBs in the Low/Hard states, ULXs in the PL state showed a cutoff at significantly low energy (~ 7 keV) compared to the BH binaries (e.g., ~ 100 keV in the Low/Hard state). Combining this with the high temperature problems seen in the disk-like shape spectra, some authors suggested that ULXs are in a somewhat unusual accretion sate which allows them to shine at super Eddington luminosities (e.g., Mineshige 2007). Since then, it has not been settled which hypothesis better explains the true nature of ULXs.

The aim of the present thesis is to examine whether the X-ray spectra of ULX are explicable as an extension of the ordinary accreting systems in our galaxy. For this purpose, we utilize the archival data of *XMM-Newton*, *Suzaku*, and *NuSTAR*, which all afford high-quality ULX spectra. Since we require high quality spectra, we limit our study to a sample of 10 luminous ULXs in nearby galaxies, with multiple data sets available from the three satellites. We attempt to fit the spectra with a unified model and seek for explanation which can describe the unique properties of ULX spectra.

2 REVIEW

2.1 Black Holes in the Universe

2.1.1 A review of black holes

The strong X-ray source Cygnus X-1 (Cyg X-1) was discovered by several rocket observations in 1962−1965 (Giacconi et al. 1967). Although the source of energetic X-ray emission was unidentified at that time, unexpected fast ($<$ 1 sec) variation of Cyg X-1, detected by first X-ray satellite *Uhuru*, led Oda et al. (1971) to argue that the size of X-ray emitting region should be compact, possibly a black hole (BH). This is the first paper that suggested an existence of BH in the universe based on an actual observational result. Just a year after the suggestion, a type-BOIb blue super giant star HD 226868 was found at the position of the X-ray source. From measurements of Doppler shift of Hβ emission line and a calculation using Kepler's law, the star turned out to be orbiting around "something" with a mass of $\sim 12 - 15 M_{\odot}$ in $\sim$ 5.6 days (Bolton 1972). Since it exceeds the maximum mass for a neutron star ($\sim 3\ M_{\odot}$), it became a consensus that the object is indeed a BH and it is shining by accreting mass from HD 226868. Thus, Cyg X-1 became the first binary system that contains a BH, so called BH binaries (BHBs).

After four decades from the discovery of Cyg X-1, at least 20 Galactic and Magellanic X-ray sources have been confirmed as BHBs. From the same technique as utilized for Cyg X-1, these BHBs systems harbor BHs with mass in the range of $4 - 20\ M_{\odot}$, with the mean $\sim 7\ M_{\odot}$. BHs in this mass range are considered to be remnants of gravitational collapse of massive stars, and hence they are called stellar mass BHs. On the other hand, from measurements of orbiting stars and gas motions at the center of galaxies, it became clear that most of galaxies harbor extremely massive BHs with a wide mass range of $10^{5-9}\ M_{\odot}$. When these BHs are under significant mass accretion, the host galaxies become so called Active Galaxies, or Active Galactic Nuclei (AGN). Since these are much more massive than the previous ones, they are called super massive BHs, and their formation scenario has been one of the biggest mysteries in astrophysics.

One of the most natural ways to form super massive BHs is to somehow feed and/or merge stellar mass BHs and make them grow over the Hubble time or even shorter. In either scenario, we expect the presence of BHs in intermediate mass ($100 - 1000\ M_{\odot}$) range. Although such BHs had not been established observationally, on September 14th 2015, the Laser Interferometer Gravitational-Wave Observatory (LIGO) has detected a significant gravitational wave event (GW150914) from a merger of two BHs, 36 $M_{\odot}$ and 29 $M_{\odot}$ each (Abbot et al. 2016). The BH merger released energy equivalent to 3 $M_{\odot}$ as gravitational waves and left a relatively massive 62 $M_{\odot}$ BH. This epoch making event has proved that such massive ($\geq$ 30 $M_{\odot}$) BHs do exist, and indicates a possibility that even more massive BHs may be present in a large number, wandering the universe.

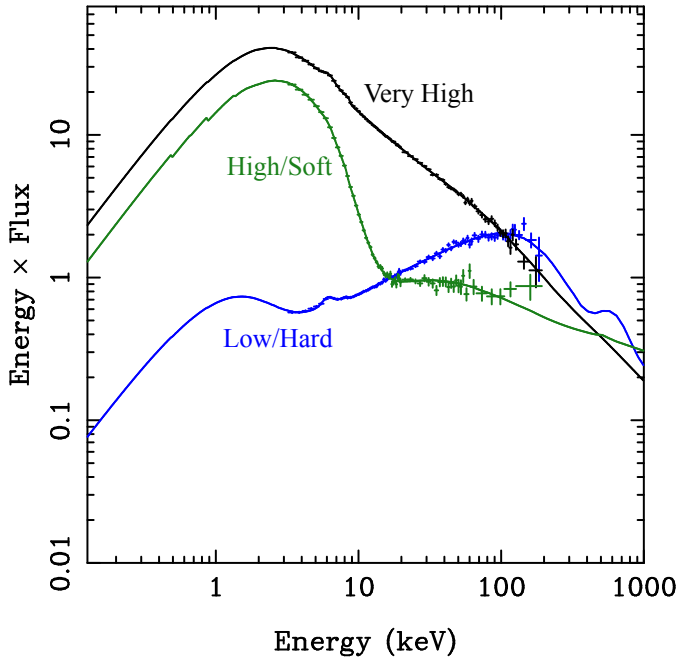

Figure 2.1. Three distinct spectral states of the BHB GRO J1655-40 (Done, Gierlinski, Kubota, 2007). Solid lines represent the best fit physical models.

2.1.2 Emission from accreting BHs

Since BHs themselves do not emit light, they are observable only when some matter falls onto them just like in Cyg X-1. The matters are heated gravitationally to high temperatures, and radiate, until they reach the event horizons of the BHs. Consider that the matter falls, with an accretion rate $\dot{m}$, onto a non-rotating BH with a mass of M. Then, the energy generation (luminosity) from the matter until it reaches the event horizon (Schwarzschild radius) $r_S = 2GM/c^2$ is $L = \dot{m}c^2/2$, where G and c are the gravitational constant and the speed of light, respectively. If this L is radiated as a black body emission from a region which has a size of $\sim r_S$, the black body temperature becomes $\sim 10^7 (M/10\ M_\odot)^{-1/4} (\dot{m}/\dot{m}_c)^{1/4}$ K where $\dot{m}_c$ is the Eddington limit described later. This is the reason why most of the accreting BHs are X-ray bright.

Although matters may gain energy enough to radiate powerful X-rays, they need to be to some extent thermalized to radiate. Since the thermalization time scale is inversely proportional to the density of the matters squared, the observed luminosity and spectral shape strongly depend on $\dot{m}$.

Generally, BHBs are known to show three distinct types of X-ray spectra as a function of $\dot{m}$, the Low/Hard state (LHS), the High/Soft state (HSS), and the Very High state (VHS). These three types of spectra are shown in figure 2.1, in which the BHB GRO J1655-40 is used as a representative example (Done, Gierlinski, & Kubota 2007). The LHS spectrum is the most dimmest one in figure 2.1, which consists of a soft excess component peaking at $\sim$ 1keV, a hard Power-Law (PL) shaped continuum with a photon index of $\Gamma = 1.5 - 1.7$, and a roll over at $\sim$ 100 keV. As the source gets luminous and makes transition to the HSS, the PL continuum becomes steeper ($\Gamma \sim 2$) and weaker, and instead the soft component becomes stronger and dominant in the spectrum. Finally as it reaches the VHS, the wakened PL continuum comes back again, but this time with even a

steeper slope of $\Gamma \sim 2.4$. It is known that the state transition occurs when the luminosity hits particular fractions of the Eddington luminosity, which can be written as,

$$L_{\rm Edd} = \frac{4\pi G M m_{\rm p} c}{\sigma_{\rm T}} = 1.5 \times 10^{38} (M/M_\odot) \ {\rm erg \ sec^{-1}}, \tag{2.1}$$

where $m_{\rm p}$ and $\sigma_{\rm T}$ are the proton mass and the Thomson scattering cross section, respectively. The Eddington luminosity represents the condition where the radiation pressure and the gravitational force balance under a spherical accretion. BHBs are known to make transitions between the LHS and the HSS typically at $\sim 0.1 L_{\rm Edd}$, while between the HSS and the VHS at $\sim 0.3 L_{\rm Edd}$ (e.g., Done, Gierlinski, Kubota, 2007).

Regardless of the spectral states, the spectrum of a BHB can be decomposed roughly into three components; the soft excess component peaking at $1-3$ keV, the PL continuum, and a local spectral structure which is particularly prominent at $6-7$ keV. The first component is considered to be emission from a standard accretion disk formed around the BH, which was introduced by Shakura & Sunyaev (1973). In fact, Makishima et al. (1986) has shown that an approximate model of the standard accretion disk emission called multi-color disk model (MCD model; Mitsuda et al. 1984) well explains the actual observational data of BHBs. The second component is considered to arise when the accretion disk photons are Compton up-scattered by a hot electron cloud. Finally, the third component appears as emission line and absorption edge feature due to Fe K-shell transitions. Although we have so far focused only on the BHB, these three components are also seen in the AGN spectra. Since especially the former two components are such fundamental characteristics seen in the accreting BH spectra, we devote the following two sections, 2.1.3 and 2.1.4 to the description of the components.

2.1.3 Emission from an accretion disk

The accreting gas around a BH is considered to form a flat disk called an accretion disk, due to its own angular momentum. Here, we assume that the accreting matters are orbiting around the BH in Kepler motion, i.e. with a velocity of $v = \sqrt{GM/r}$ where r is the radius from the center of the BH. Since matters at smaller r rotate with a higher angular frequency than those at larger r, the angular momentum is gradually transported outwards via friction between neighboring radii of the disk. If $\dot{m}$ is high enough, the emissivity increases up to the black body regime, in which the generated thermal energies are immediately dissipated as radiation. In such an accretion phase, the disk is kept relatively cool and becomes geometrically thin, because of the efficient thermalization and radiative cooling.

The standard accretion disk model is an analytic solution to such a radiatively efficient accretion flow, introduced by Shakura & Sunyaev (1973). Under the Keplerian motion, the virial theorem is applicable, in which half the released gravitational energy goes into the Kepler motion and the rest is radiated away. Since the disk is optically thick, each radial component dissipates this energy as a black body emission with an effective temperature of $T_{\rm eff}(r)$. Hence by combining these two conditions, the energy flux density at radius r is written as

$$\sigma T_{\rm eff}(r)^4 = \frac{3GM\dot{m}}{8\pi r^3} \left(1 - \sqrt{\frac{R_{\rm in}}{r}} \right), \tag{2.2}$$

where σ is the Stefan-Boltzmann constant. Accordingly, the energy flux of such a disk can be obtained by integrating the black body emissions from outer-most radius $R_{\rm out}$ to the inner-most radius $R_{\rm in}$. The result can be written as

$$F(E) = \frac{\cos \mathrm{i}}{D^2} \int_{R_{\rm in}}^{R_{\rm out}} 2\pi r B(E, T_{\rm eff}(r)) dr, \tag{2.3}$$

where i, D, and $B(E,\ T_{\rm eff}(r))$ are the inclination angle of the disk, the distance to the observer, and the black body flux function at temperature $T_{\rm eff}(r)$, respectively.

As mentioned in the previous subsection, Makishima et al. (1986) employed this disk emission model, with some approximations, to actually observed BHB HSS spectra. The approximated model is called a multi-color disk model (MCD model; Mitsuda et al. 1984), in which the accretion disk is assumed to extend up to infinite radius. This approximation allows us to ignore the $R_{\rm in}/r$ term in equation 2.2, and the effective temperature can be rewritten as

$$T_{\rm eff}(r) = T_{\rm in} \left(\frac{r}{R_{\rm in}} \right)^{-\frac{3}{4}}, \tag{2.4}$$

where $T_{\rm in}$ is the inner-most disk temperature. Then, the bolometric luminosity of the disk can be obtained by simply integrating black body emission from all radii, as

$$L_{\rm disk} = 2 \int_{R_{\rm in}}^{\infty} 2\pi r T_{\rm eff}(r)^4 dr = 4\pi R_{\rm in}^2 \sigma T_{\rm in}^4. \tag{2.5}$$

Here, we substituted equation 2.4 to $T_{\rm eff}(r)$ in equation 2.5.

According to general relativity, there is a minimum radius for a stable circular orbit around a BH, which is called the inner-most stable circular orbit (ISCO). It is expressed as,

$$R_{\rm in} = 3\alpha R_{\rm S} = \frac{6GM\alpha}{c^2} = 8.86\alpha \frac{M}{M_\odot} \text{ km}, \tag{2.6}$$

where α is a spin parameter of a BH which takes a value between $1/6 \leq \alpha \leq 1$. Thus, for a Schwarzschild BH ($\alpha = 1$), ISCO is equivalent to 3 times the Schwarzschild radius, whereas it shrinks down to 0.5 times the Schwarzschild radius for a maximally rotating Kerr BH ($\alpha = 1/6$).

Figure 2.2 shows examples of applying the MCD model to the actual data. There, High/Soft state spectra of the BHB LMC X-3 at various luminosities are individually fitted with the MCD model (dotted line). As can be seen, the spectra are well reproduced by the MCD model. Since the luminosity is an observed quantity and the peak energy of the MCD model gives the inner-radius temperature $T_{\rm in}$, we can derive $R_{\rm in}$ from each spectrum by utilizing equation 2.5. The time dependence of $R_{\rm in}$ and $T_{\rm in}$ is shown in figure 2.3. Although $T_{\rm in}$ varied by a factor of two as $\dot{m}$ varied, the derived $R_{\rm in}$ is quite constant throughout the observation, indicating the presence of a well-defined radius of ~ 50 km, which is likely to be the ISCO. If we assume a Schwarzschild BH for LMC X-3, then the BH mass is calculated as $\sim 6\ M_\odot$ from equation 2.6, which is consistent with the result obtained from optical Doppler measurements of the companion ($5.0 - 7.2\ M_\odot$). Thus, the standard accretion disk model successfully explains the soft excess component in the X-ray spectra of the BHBs.

2.1.4 Comptonization

If some parts of the accretion disk become somehow radiatively inefficient, those parts become hotter than the accretion disk because the radiative cooling is now ineffective. Then the flows

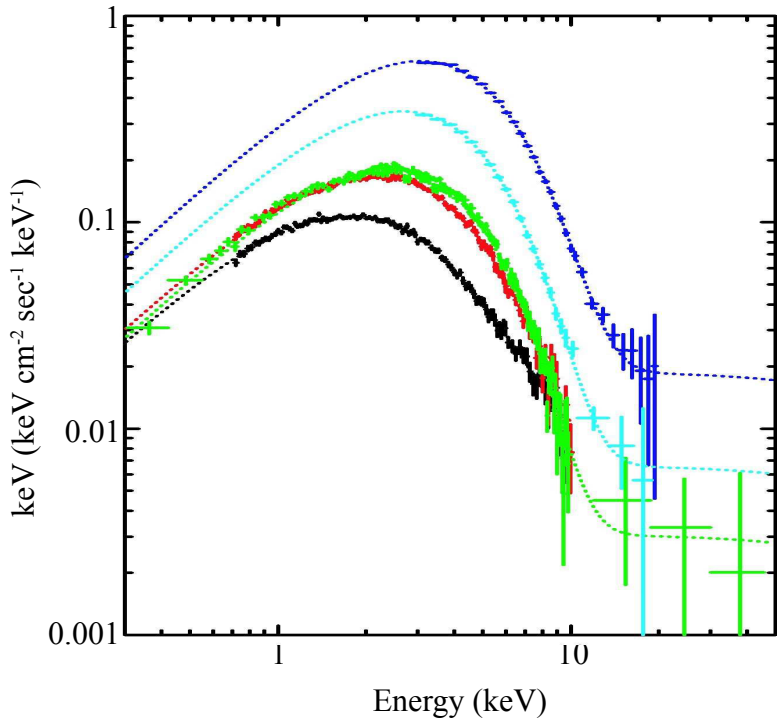

Figure 2.2. Series of High/Soft state spectra of the BHB LMC X-3 (Done, Gierlinski, Kubota, 2007).

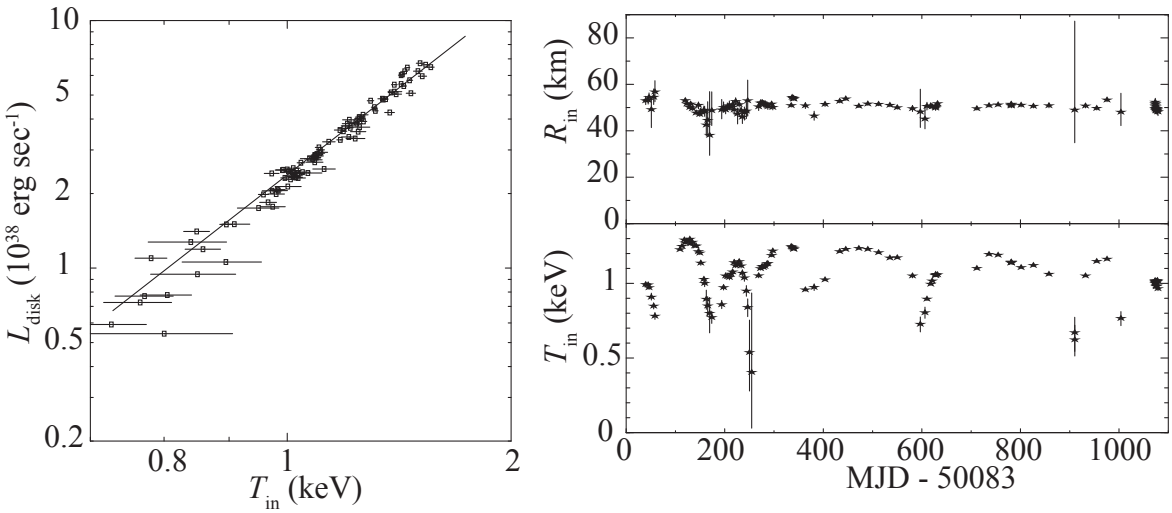

Figure 2.3. (left) Correlation between the innermost disk temperature T_{in} vs the bolometric disk luminosity L_{disk} and (right) time vs T_{in} and R_{in} of LMC X-3.

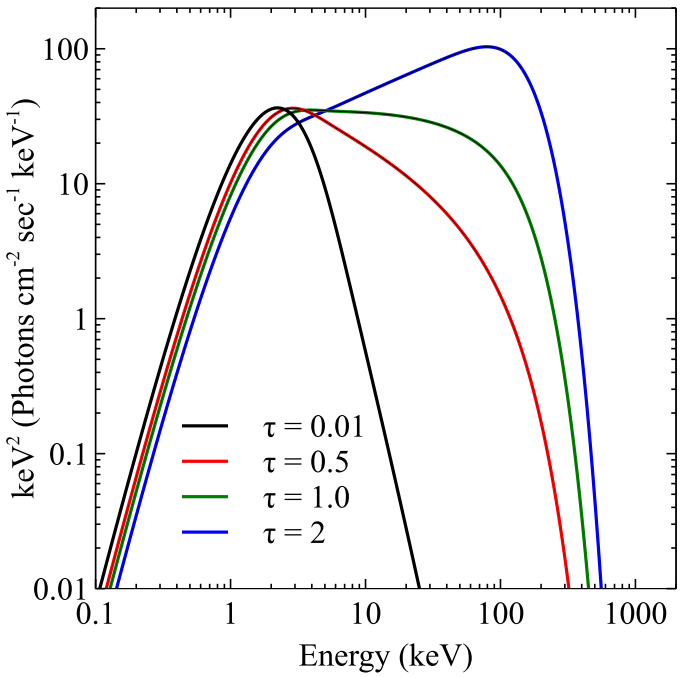

Figure 2.4. Comptonized spectrum with different coronal optical depth.

no longer emit black body emission, instead they start to pass energies to the photons from the accretion disk via inverse-Compton scattering. Such a radiatively inefficient hot flow, so called a corona, is considered to be accounting for the PL-shaped continuum seen in the individual spectral states.

The incident photons gain energy from the hotter electrons inside the corona. The mean energy gain is expressed as,

$$y = \left(\frac{4kT_{\rm e}}{m_{\rm e}c^2}\right)\tau(1+\tau/3), \tag{2.7}$$

where $T_{\rm e}$, $m_{\rm e}$, and τ are the electron temperature, the electron mass, and the coronal optical depth, respectively. Thus, the energy gain is determined by the electron temperature and the mean scattering number i.e., the optical depth. Figure 2.4 presents several lines of Comptonization model with different τ. Here, the temperature of the coronal electron and the black body which generates the seed photons are set to 30 keV and 0.5 keV, respectively. At small τ of 0.01, since the corona is nearly transparent to Compton scattering, the spectrum is nearly identical to the original black body emission. As τ increases, the spectrum starts to exhibit PL shape at higher energy, and a roll over representing the electron temperature emerges at $\sim 3T_{\rm e}$. Since the low-energy photons are up-scattered toward higher energy at the same time, photon number is decreased at energy around the Rayleigh-Jeans regime of the original black body spectrum. If the corona is optically thick enough, the spectrum exhibits a peak feature called Wien peak at $\sim 3T_{\rm e}$ like the line of $\tau = 2$ in figure 2.4. In such thick corona, the Comptonization is nearly saturated, in which the spectral shape starts to represents the thermal distribution of the coronal electron and eventually becomes a black body emission.

2.2 Ultra Luminous X-ray Sources (ULXs)

Thanks to development of instruments with higher angular resolutions and sensitivities, more than 470 ULXs candidates are found in external galaxies (Walton et al. 2011) since the discovery with the *Einstein* satellite (chapter 1). As studies on ULXs made progress, it turned out that many ULXs are associated with galaxies or region where star formations are active, such as starburst galaxies, at arms of spiral galaxies, and irregular galaxies. Since ULXs are considered as mass accreting BHs, this association may be natural from a view point that it is easier for BHs to acquire their companion stars which stably support the persistent high luminosities of ULXs. However, the true reason to this association is still under debates.

In order to determine their BH mass, large number of attempts have been done by numbers of authors to identify their companion stars and measure their orbital motions to obtain the mass functions of the binary systems. Although some succeeded to identify their possible companion stars (e.g., Heida et al. 2015), still their mass functions are poorly constrained (e.g., Motch et al. 2014). Therefore, X-ray spectroscopy plays an important roll to understand the nature of this enigmatic sources.

2.2.1 X-ray Spectra of ULXs

Thanks to the wide band and the high angular resolution of the *ASCA* satellite, spectroscopy of each ULX became possible, which gave an significant leap to the understanding. As an example, X-ray spectra of representative ULXs, NGC 1313 X-1 and X-2, taken with the *XMM-Newton* satellite are shown in figure 2.5 in $\nu F\nu$ form. Thus, ULXs show roughly two distinct types (with possible extra subgroups; Gladstone et al. 2009) of X-ray spectra, and some of them (including NGC 1313 X-1) are known to shift their spectral types in time just like in the ordinary BHBs (section 2.1). Both types of spectra rollover at $5 - 7$ keV and spread only in limited X-ray band of $0.1 - 15$ keV. In addition, they are extremely featureless. Especially, the strong structures from Fe K-shell, which was commonly seen in spectra of BHBs, are absent. In the following sections we describe the detail characteristics and physical interpretations of these two spectral states.

Disk-like state

Disk-like state is a spectrum with a convex shape, peaking at ~ 3 keV (shown in red in figure 2.5) and typically more luminous than the other spectral state. It is called "Disk-like" mostly because the spectrum can be well reproduced by a single MCD model like in the High/Soft state of galactic BHBs, which was previously reported by Makishima et al. (2000).

As described in chapter 1, although the MCD model fits the spectrum, their obtained inner-radius temperatures of $T_{\rm in} \sim 1.3$ keV are too hot to be explained as emissions from accretion disks around intermediate mass BHs which possibly explain the high luminosities of $> 10^{39}$ erg sec^{-1}. In order to explain this too high $T_{\rm in}$ problem, Makishima et al. (2000) assumed the BHs in ULXs to have spins, which makes the ISCOs to be closer to the central BHs and gives systematically higher $T_{\rm in}$ than the Schwarzschild BHs (section 2.1.3).

Although the spectra were successfully explained as emissions from highly spinning intermediate mass BHs, it turned out that some ULXs do not follow the relation of $L_{\rm disk} \propto T_{\rm in}^4$, which

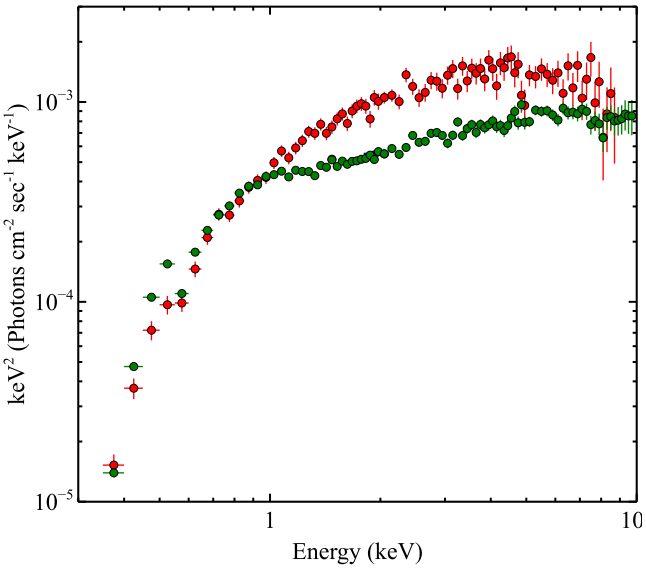

Figure 2.5. X-ray spectra of representative ULXs NGC 1313 X-1 (green) and NGC 1313 X-2 (red) in different spectral states.

was expected if the disk was in standard accretion regime (Mizuno et al. 2000, Mizuno et al. 2001). For this reason, some authors alternatively suggested that ULXs are possibly accreting mass at significantly high rate, in which the accretion disks are no longer in standard accretion regimes (e.g., Mineshige et al. 2007). An analytic solution for disks in such high accretion rate regime is known as Slim disk (Watarai 2000). The emission from the Slim disk can be approximated by making the radius dependence of the disk temperature from $\propto r^{-0.75}$ (equation 2.4) to a more flatter distribution $\propto r^{-0.5}$.

In fact, if we employ a model called variable-p disk model, which has the radial distribution index as a free parameter, to the Disk-like spectra, it gives good fits with temperature distribution near to the Slim disk solution ($p \sim -0.5$; e.g., Isobe et al. 2012). However, Miyawaki et al. (2009) pointed out that this Slim disk solution do not give good explanation to the spectral variation of the ULX M82 X-1. Since the spectrum of this source became harder as it became more luminous, the variable-p disk model indicated that the spectrum became rather closer to the standard accretion disk at the higher luminosity, which is unreasonable. Thus, the best modeling for this particular spectral shape is still under discussion.

Power-Law (PL) state

As the source becomes dimmer from the Disk-like state, they make transition to a state called PL state (the green spectrum in figure 2.5). This state is composed of two components. One is a hard ($\Gamma \sim 1.7$) PL shaped continuum which has a turn over at ~ 8 keV. Although the overall feature of this turn over has been a mystery, thanks to the high S/N ratio of *NuSTAR*, it is now known that this continuum continuously drops sharply above 10 keV (Bachetti et al 2013). Another is a exceeding component which typically peaks at ~ 1 keV.

The former component can be well reproduced by a thermal Comptonization (section 2.1.4) by an optically thick ($\tau \sim 10$) and low temperature ($T_e \sim 3$ keV) electron cloud, while the latter can be interpreted as an optically-thick emission providing some seed photons to the election cloud

(Gladstone et al. 2009).

Although the spectrum is explicable with the ordinary modeling utilized in BHB studies (section 2.1.3 and 2.1.4), it is noticeable that its spectral appearances are quite distinctive from what are observed in the Galactic BHBs. For example, while the PL state has a similarly hard continuum as the Low/Hard state of BHB, the energy where the spectrum rolls over ($\sim$ 7 keV) is significantly lower than that in the BHB ($\sim$ 100 keV).

2.2.2 Possible interpretations of ULXs

Since the X-ray spectra of ULXs show such distinctive characteristics from those of the Galactic BHBs, interpretations of these enigmatic sources are still unsettled. Here we introduce two representative hypothesis.

Intermediate-mass BHs

This is a hypothesis that assumes that the ULXs are sub-Eddington objects, and harbor BHs with masses of $100 - 1000\ M_{\odot}$ (e.g., Makishima et al. 2000). As described in the previous sections, since the behavior of the X-ray spectra of ULXs are considerably different from those of the Galactic BHBs, and the formation mechanism for such massive BHs is not known, it has been always considered with alternative options such as a hypothesis shown later. However, as described in chapter 1, the detection of the gravitational event GW150914 has proved the presence of massive ($\sim 60\ M_{\odot}$) BHs, which strongly supports this hypothesis.

Stellar-mass BHs with super-critical accretion flows

This assumes that the ULXs are stellar mass ($\sim 10\ M_{\odot}$) BHs shining at super-Eddington regimes via super-critical accretion flows (e.g., Mineshige et al. 2007). Since none of the Galactic X-ray binaries are known to persistently overwhelm their Eddington limit, people rely on computational studies to explain the spectra of ULXs. Although some 3D MHD simulations have roughly reproduced the unique shapes of the ULX spectra (e.g., Kawashima et al. 2012), some features such as spectral variability are still left to be explained.

3 INSTRUMENTS

3.1 The *Suzaku* Satellite

3.1.1 An overview

Suzaku is the fifth Japanese X-ray astrophysical mission which follows *Hakucho* (launched in 1979), *Tenma* (1983), *Ginga* (1987), and *ASCA* (1993). An identically designed satellite, called *ASTRO-E*, was to be sent in orbit on 2000 February 10, but it was unfortunately lost due to malfunction of the M-V rocket. From this background, *Suzaku* is also known as *ASTRO-E2* project, which was a recovery mission to *ASTRO-E*. *Suzaku* was successfully launched on 2005 July 10 from Uchinoura Space Center (USC) of ISAS/JAXA at Kagoshima prefecture with the M-V rocket unit No.6. It acquired a circular orbit with the height of 568 km, the inclination angle of 30 degrees, and the orbital period of 96 minutes. Thanks to the low-altitude orbit, a low background environment was achieved. In 10 years of operation, in May 2015, JAXA has decided to terminate the mission and it became the second longest lived satellite among all the Japanese X-ray satellites.

Figure 3.1 is a schematic drawing of the *Suzaku* spacecraft. It consists of five pairs of soft X-ray mirrors and detectors, and one hard X-ray detector. These instruments altogether enabled a wide band ($0.3 - 600$ keV) coverage with a single satellite. Of the five X-ray mirrors, or the X-ray Telescope (XRT) modules, four focused onto four X-ray CCD cameras called the X-ray Imaging Spectrometer (XIS), working in the $0.2 - 12.0$ keV range, and the remaining one onto the X-ray Spectrometer (or X-ray micro calorimeter), XRS. Especially, the latter was capable of high resolution spectroscopy with ~ 5 eV energy resolution at $0.5 - 10$ keV, which was overwhelming those of the other X-ray satellites in orbit at that time. Unfortunately, just a month after the launch, and immediately after the start of test observations, the XRS stopped working due to a tragic leakage of liquid helium. Although the XRS was no longer available, the wide band achieved with the XIS and the Hard X-ray Detector (HXD) was a unique ability of *Suzaku* even after the launch of *Nu-STAR* in 2012. In the following sections, we review characteristics of the XRT (section 3.1.2) and the XIS (section 3.1.3), which play important rolls in the present study.

3.1.2 The X-ray Telescope (XRT)

The X-ray telescope (XRT) on-board *Suzaku* consists of 5 units of X-ray mirrors, capable of reflecting $0.1 - 13$ keV X-ray photons and creating images at its focal plane. Four units (called XRT-i) focusing on the XIS are identical to one another, whereas the fifth one (called XRT-S) coupled to the XRS has slightly different parameters. Figure 3.2 is an actual photograph of one of the *Suzaku* XRT flight model units. Each of them is Wolter-I type telescope, which consists of 175 concentrically nested X-ray mirror foils. Each mirror foil, in turn, is made of 152 μm thick Al foil, shaped

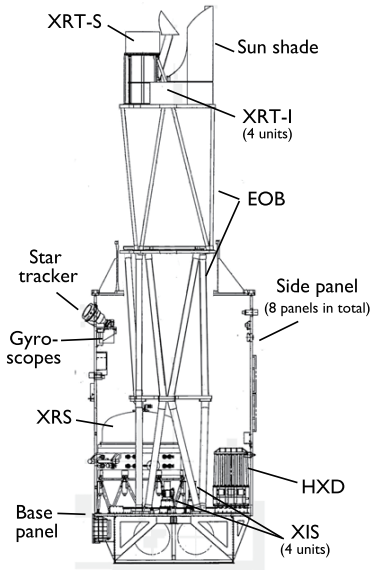

Figure 3.1. Side view of the *Suzaku* satellite (Mitsuda et al. 2006).

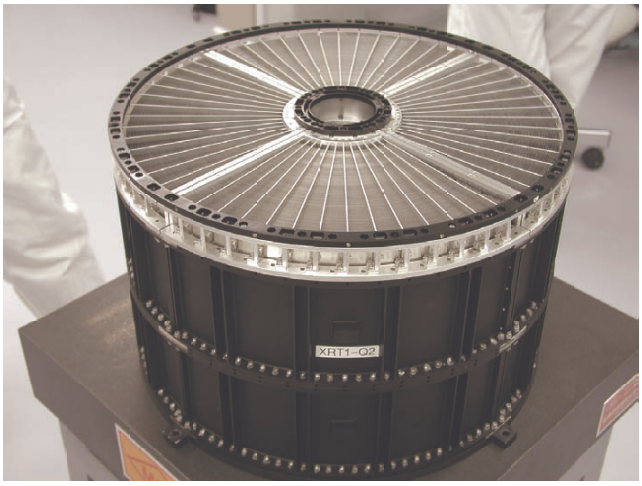

Figure 3.2. A photograph of one unit of the *Suzaku* XRT (Serlemitsos et al. 2006).

into a conical form and coated with > 1000 Å thick Au. The XRT has a focal length of 4.75 m (4.50 m for XRT-s) and a spacial resolution of $2'.0$ in half power diameter.

Figure 3.3 shows the effective area of the XRT when combined with the focal plane detectors. Due to materials used in the XRT mirror foils and thermal shield foils placed in front, several absorption-edge features are present in the effective area curves. The edges at 0.54 keV and 1.56 keV are absorption from K-shell of O and Al, respectively, both used in the thermal shield. The series of edge features at $2 - 3$ keV are the M-edge absorption from the Au coating. Thanks to enlarged geometrical area of 873 cm^2 per unit, the effective area has improved by 1.5 times and 1.7 times from that of *ASCA* at 1.5 keV and 7.0 keV, respectively.

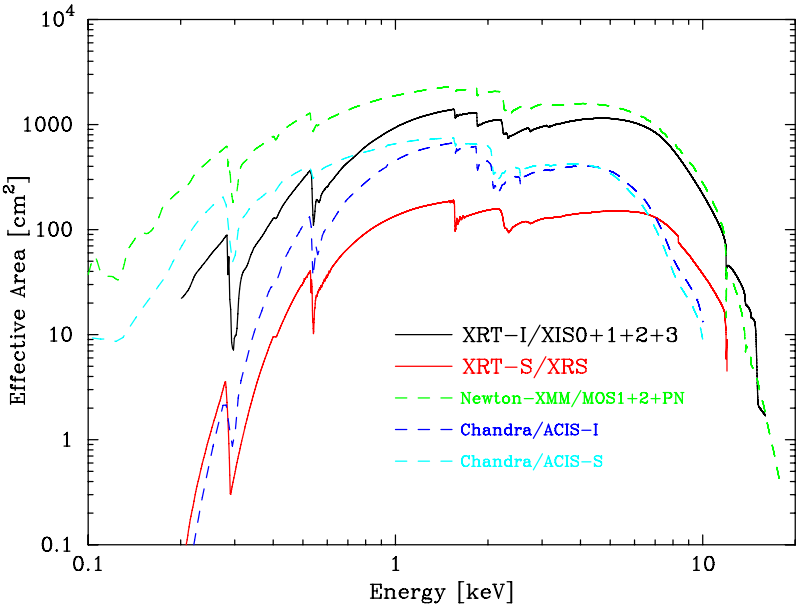

Figure 3.3. Effective are of the *Suzaku* XRT, including the thermal-shield absorption, the detector quantum efficiency, and all other effects. For comparison, the effective areas of other satellites are also shown (Serlemitsos et al. 2006).

3.1.3 The X-ray Imaging Spectrometer (XIS)

The X-ray Imaging Spectrometer (XIS) comprises four X-ray CCD cameras, of which three (XIS0, XIS2, and XIS3) are identical and utilize front-illuminated (FI) CCD chips, whereas the other (XIS1) uses a back-illuminated (BI) CCD chip. Each camera is placed at the focal plane of the corresponding XRT unit, and detect $0.1 - 12$ keV photons one by one to determine its energy and position individually. The left panel of figure 3.4 is a photograph of an actual XIS detector on-board *Suzaku*. As shown in the right panel of figure 3.4, a CCD chip used in an XIS camera consists of an imaging area and a frame-store region, both having 1024×1024 pixels. This 1024×1024 pixels are read out by four different read-out nodes, each covering 1024×256 pixels (A-D in figure 3.4). After exposing the imaging region to the focused X-rays for a given exposure time (8 sec in default setting), the XIS starts to transfer the charge generated inside the Si semiconductor pixels toward the four read-out nodes. Although the energy of an incident X-ray photon is basically proportional to the amount of charge created in the CCD. the energy vs charge relation may change in time, due to aging degradation, fluctuation of induced bias voltage, and temperature change. In order to follow this change in orbit, two ^{55}Fe radio isotopes illuminate two corners of the imaging area with 5.9 keV and 6.4 keV fluorescence X-rays. Therefore, these corner regions should not be used in spectral analysis.

Figure 3.5 shows the quantum efficiency of an FI-XIS and a BI-XIS as a function of energy. In the FI XIS, X-ray photons enter the depletion layers of the CCDs from the front side with the electrodes and SiO_2 layers, while it is opposite in the BI XIS. Since, low energy X-ray photons ($\leq$ 4 keV of figure 3.5) are strongly absorbed by the front-side materials, the BI XIS is superior to the FI XIS in terms of the quantum efficiency at lower energies. In higher energies, the FI XIS has a higher quantum efficiency since the thickness of the depletion layer is thinner in the BI XIS. Figure 3.6 shows background spectra of FI/BI XIS, acquired when *Suzaku* was observing night Earth.

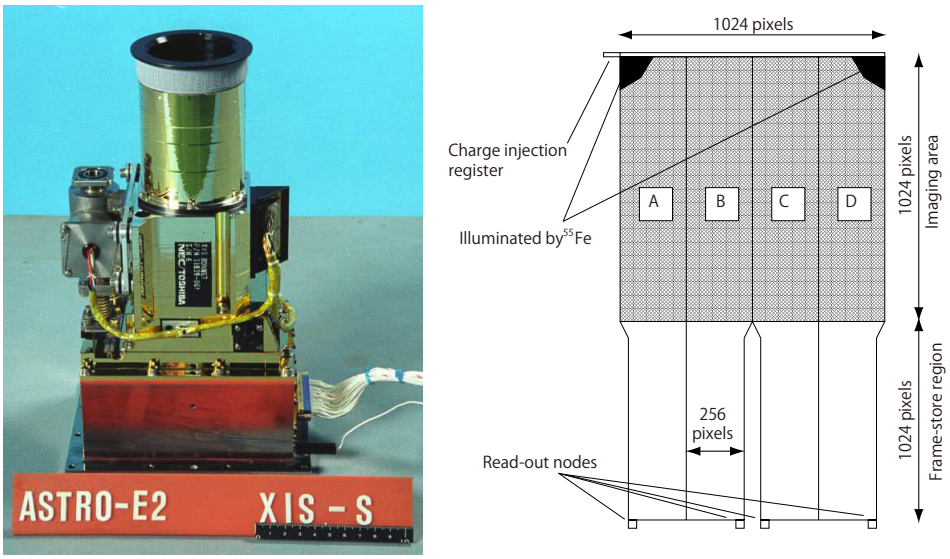

Figure 3.4. A photograph of one XIS camera (left) and a schematic drawing of an XIS CCD (right), taken from Koyama et al. (2006).

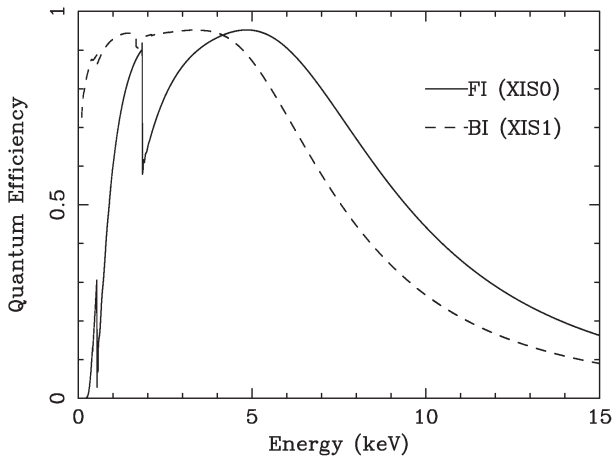

Figure 3.5. Quantum efficiency of the XIS as a function of energy (Koyama et al. 2006).

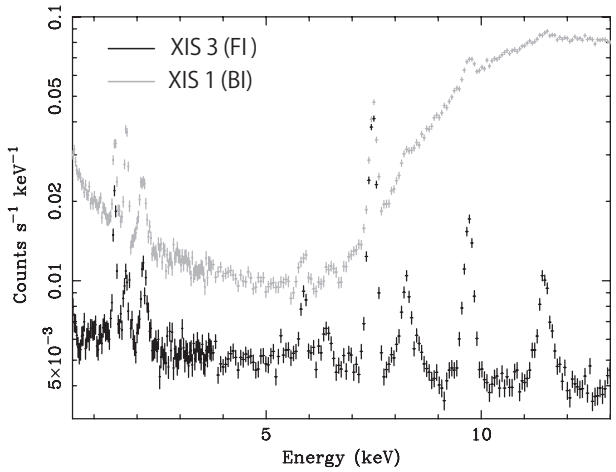

Figure 3.6. Background spectra of FI/BI XIS (Koyama et al. 2006). They are obtained from night-Earth observations.

Thanks to low orbit, XIS have low background rate in orbit. Line features are fluorescence X-rays from materials surrounding the XIS detectors such as Fe (6.4 keV), Ni (7.4 keV), and Cu (8 keV). The BI XIS has higher background rate than the FI XIS, particularly in energies above 8 keV. For this reason, we mainly use the FI XIS data to study the higher end of the effective energy band ($0.5 - 12$ keV), while the BI XIS data to obtain information in the lower energy band ($0.3 - 8$ keV).

3.2 *XMM-Newton*

3.2.1 An overview

X-ray Multi-Mirror Mission (*XMM-Newton*) is the largest cosmic X-ray mission that has ever been developed by the European Space Agency (ESA) as a cornerstone project of ESA Horizon program, with an objective of performing high quality soft X-ray spectroscopy of faint sources in the universe. It was launched successfully from ESA's launch base in Kourou, French Guiana, on 1999 December 10 with the Ariane rocket unit No. 504. It was placed in a highly eccentric 48 hours period orbit with the perigee altitude of 850 km, the apogee altitude of 114000 km, and the inclination of $\sim -40^{\circ}$. It provides wide band coverage ($0.2 - 10$ keV) and high photon-collecting area (~ 2000 cm^2 at 1.5 keV), by combining three X-ray telescopes with large effective areas and X-ray CCD detectors with high quantum efficiencies. It is also capable of observations with high energy resolution of $\Delta E \sim 3$ eV at $0.3 - 2.5$ keV by utilizing reflecting gratings. Yet another outstanding feature of *XMM-Newton* is its capability of observing an X-ray source continuously, without interrupted by Earth occultations of the source, or by spacecraft passage through South Atlantic Anomaly. This is owing to the highly elongated orbit, but a penalty is that the data are often contaminated by soft proton flares (mainly from the Sun) from which *Suzaku* is free due to magnetospheric shielding.

As shown in figure 3.7, the spacecraft consists of three main components, the Focal-Plane Assembly (FPA), the Telescope Tube (TT), and the Mirror Support Platform (MSP). As implied by the name "XMM: X-ray Multi Mirror", the MSP carries three large reflecting telescopes, which individually focus on three units of European Photon Imaging Camera (EPIC) placed on the focal plane platform comprising the FPA. The FPA and MSP are connected by the 6.8 m long TT, which assures the 7.5 m focal length and the alignment between the mirrors and respective focal-plane detectors. In total, *XMM-Newton* is 10 m long and weights 3800 kg.

Although the three EPIC units are photon-counting CCD detectors like the *Suzaku* XIS, two of them (EPIC-MOS) utilized Metal-Oxide Semiconductor type CCD chips and the other uses a p-n junction type one (EPIC-PN). In the following sections, we summarize the characteristics of X-ray telescopes and the EPIC units which are involved in the present work.

3.2.2 X-ray telescopes

Each of the X-ray mirror telescopes on-board *XMM-Newton* is capable of reflecting X-ray photons in $0.2 - 10$ keV. The mirror assembly consists of a paraboloid section and a hyperboloid section, each containing 58 mirror shells nested in a concentric geometry. The two sections together form Wolter-I grazing-incident optics. Each mirror shell is replicated from super-polished Au (~ 200

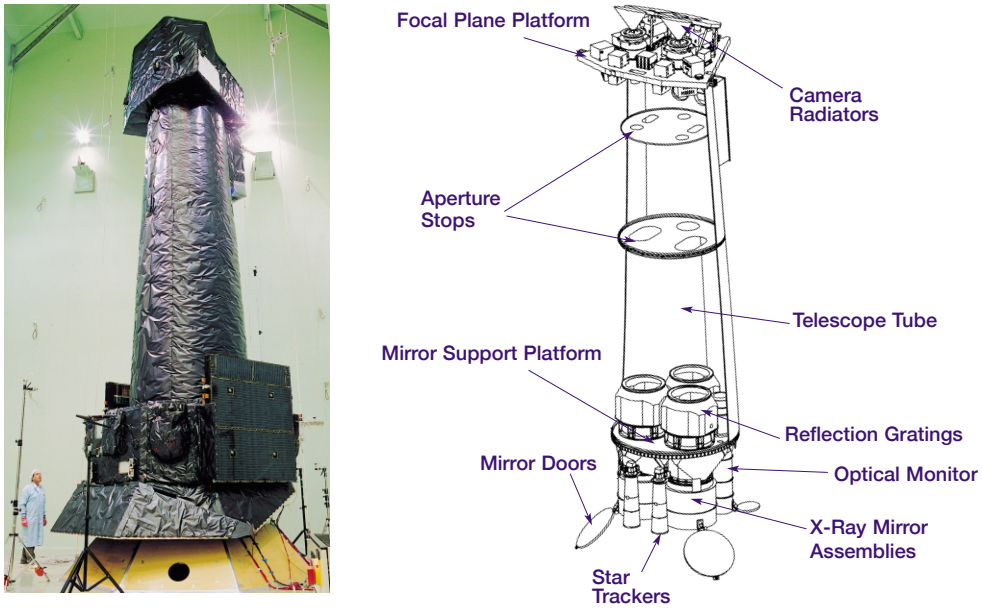

Figure 3.7. A photograph of the *XMM-Newton* spacecraft (left: van Katwijk et al. 1999) and a schematic drawing of its configuration (right: Barre et al. 1999). Signal X-rays enters the spacecraft from the bottom upward.

nm thick) coated mandrels using Ni electroforming technique. In order to maximize the effective area within a restricted size budget, the mirror shells are stacked as much as possible with optimized thicknesses, 1 mm for the outermost shells with a diameter of 70 cm, and 0.5 mm for the innermost shell of 30.6 cm diameter. Figure 3.8 shows the effective area of the X-ray mirrors of *XMM-Newton* as a function of energy. The structures around 2 keV are M-edges of Au on the mirrors, and the sharp decrease at $\geq$ 10 keV is because the critical angle for the total reflection approaches zero approximately as inverse square of the photon energy. Thus, the three X-ray mirror telescopes of *XMM-Newton* achieved a large total effective area of $\sim$ 1500 cm^2 at 1.5 keV (solid line in figure 3.8).

Although the three mirror telescopes are identical to one another, two of them which correspond to the EPIC MOS are equipped with Reflection Grating Assembly (RGA), which gives $\sim$ 44% of incident X-rays to the initial focal plane (MOS) and $\sim$ 40% to another CCD called Reflection Grating Spectrometer (RGS). This gives a difference in terms of effective area as shown in figure 3.8 that EPIC PN has nearly twice as large effective area as the single EPIC MOS does.

Figure 3.9 shows Encircled Energy Function (EEF) of the X-ray mirror telescope No. 3. In order to detect faint X-ray sources with high signal to noise ratio, the X-ray mirror telescopes of the *XMM-Newton* were designed to have high angular resolution, which is $\sim 12''$ in half power diameter as shown in figure 3.9. Since the EEF at 1.5 keV is almost identical to that at 8 keV, the angular resolution is approximately energy independent.

3.2.3 The European Photon Imaging Camera (EPIC)

Figure 3.10 shows a rough sketch of the field of view of the two type of EPIC cameras, EPIC MOS and EPIC PN. One MOS camera consists of 7 segments of front-illuminated CCD chips, each having a format of 600 $\times$ 600 pixels. On the other hand, the PN camera consists of 12 back-

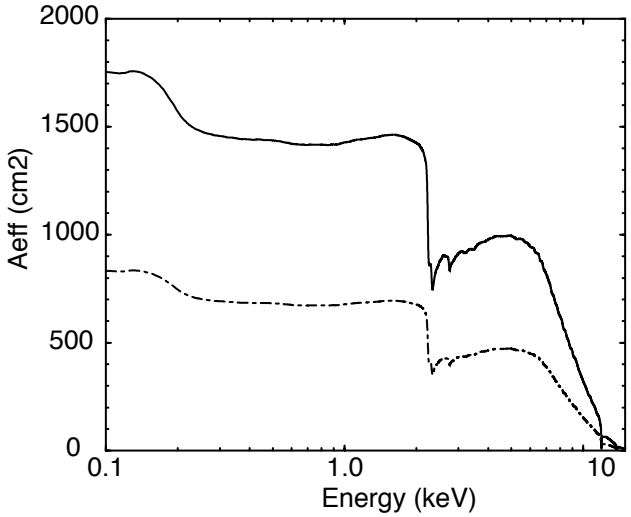

Figure 3.8. Effective areas of *XMM-Newton* X-ray telescopes as a functions of energy (Jansen et al. 2000). That of mirrors with the RGA is shown in dot-dashed line, while that without the RGA (with the three telescopes summed up) is in solid line.

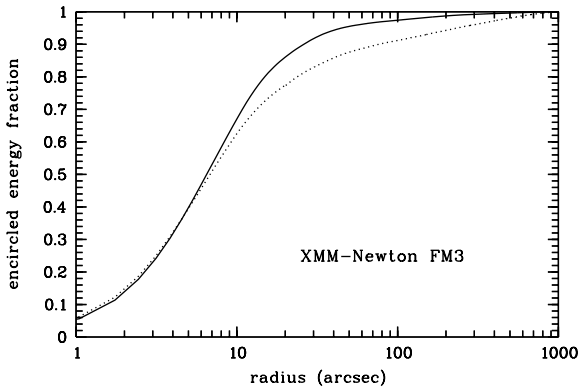

Figure 3.9. Encircled energy function (EEF) of the X-ray telescope No.3, measured at 1.5 keV (solid line). Taken from Aschenbach 2002.

Table 3.1: Key parameters of the two types of EPIC cameras

	EPIC-MOS	EPIC-PN
Energy resolution (at 1 keV)	70 eV	80 eV
Time resolution (in full frame)	2.6 sec	73.4 ms
Effective area (at 6 keV)	~ 300 cm^2	~ 900 cm^2
Pixel size	40×40 μm^2	150×150 μm^2
Thickness of depletion layer	$35 - 40$ μm	280 μm

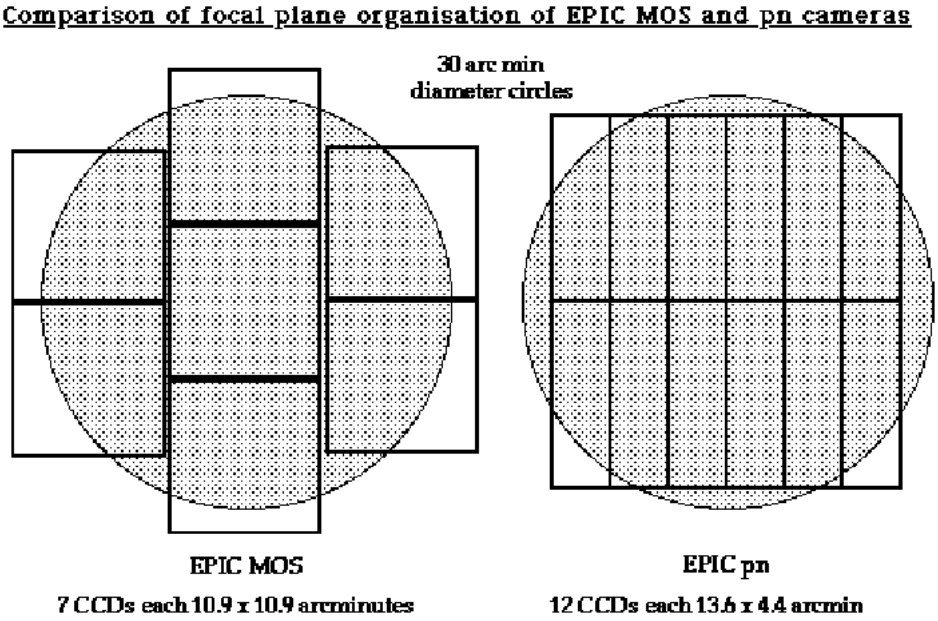

Figure 3.10. A schematic drawing of the fields of view of the two types of EPIC cameras. The shaded region indicates a 30′ diameter circle. Taken from *XMM-Newton* users handbook, section 3.3, figure16.

illuminated CCD chips with 200×64 pixels each. Both are covering similar fields of view of 30′ diameter circle. Key parameters of the two types of EPIC cameras are summarized in table 3.1.

Comparing the two types of EPIC cameras, the energy resolution of EPIC MOS at 1 keV is similar to (or slightly better than) that of EPIC PN. EPIC MOS has a smaller pixel size than EPIC PN, which makes EPIC MOS more sensitive to fine structure of X-ray images. However, the time resolution of EPIC PN is $\sim$ 30 times better than that of EPIC MOS, because EPIC PN reads out the entire region in parallel with larger number of read out nodes. In addition, EPIC PN has three times larger effective area than the other type, since it has a thicker depletion layer and also it utilizes the entire effective area of the X-ray mirror (section 3.2.2).

In figure 3.11, we show background spectra of EPIC MOS (left) and EPIC PN (right). The line features are fluorescence X-rays from surrounding materials. As can be seen in figure 3.11, the background count rate of EPIC MOS is lower than that of EPIC PN. Especially at the higher energy band, several significant fluorescence line features are present only in the EPIC PN spectrum. These lines originate in metals inside the circuit board which is placed just behind the PN sensor. Therefore, the strength of the line components is position dependent, and we must be careful which region to choose for extracting the background spectra (section 4.2.1). Otherwise, some fake structures could be left in the spectrum around the energy where these lines are present.

3.3 Nuclear Spectroscopic Telescope ARray (*NuSTAR*)

3.3.1 An overview

In early 2000s, X-ray observations above 10 keV were relying on the coded mask technologies or simple collimators just like in the *Suzaku* HXD. This is mainly because the critical angle for the total reflection is extremely small ($<$ 1 degree) at hard X-rays, so that it was difficult to utilize,

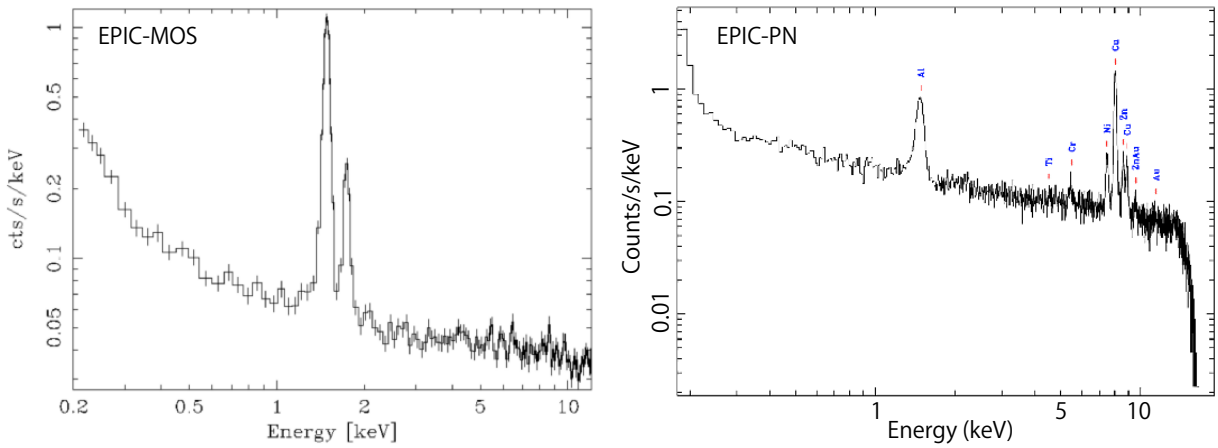

Figure 3.11. Background spectra of the two types of EPIC cameras. Taken from *XMM-Newton* users handbook, section 3.3.7.2, figure 34 and figure 35.

in these energies, the grazing-incident optics which are very standard in < 10 keV as described in section 3.1.2 and section 3.2.2. However, thanks to the new technology of incorporating Bragg reflection by synthetic multi-layer coatings, X-ray mirrors focusing > 10 keV photons have been realized.

The NASA Small Explorer mission, named Nuclear Spectroscopic Telescope ARray (*NuSTAR*), was the first satellite to bring the hard X-ray focusing mirror in orbit. The primary objective of the mission is to explore X-ray spectroscopy above 10 keV with the highest sensitivity ever achieved. On 2012 June 13, it was launched from the Reagan Test Site on the Kwajalein Atoll in the South Pacific into a near-equatorial, low-Earth orbit with the Pegasus XL vehicle No.41. Since the payload size is restricted, it was launched in a stowed configuration (the bottom panel of figure 3.12), and then the extendable mast was deployed in orbit after 9 days of the launch to achieve the focal length of 10.14 m (the top panel of figure 3.12). The *NuSTAR* observatory is 11 m long, and weights 350 kg. Since it carries no consumables, the life time is mainly limited by the orbit decay which is expected to be ~ 10 years.

NuSTAR carries two pairs of hard X-ray telescopes, which focus on two CdZnTe (CZT) detectors mounted on the focal plane bench. The detectors, called the Focal Plane Module (FPM; subsection 3.33) enable imaging and spectroscopy in a $3 - 79$ keV band as a whole. Thanks to the hard X-ray imaging capability, the signal to noise ratio has improved dramatically from the previous detectors on-board other satellites, achieving nearly two orders of magnitude higher sensitivity at the $10 - 30$ keV band.

3.3.2 X-ray telescopes

The X-ray mirrors on-board *NuSTAR* form Wolter-I telescope with focal length of 10.14 m, each nesting 133 multilayer-coated grazing incidence shells in concentric geometry. The new technology of depth-graded multilayer coating has enable to utilize Bragg reflection for hard X-ray photons, which cannot be focused by ordinary total reflection. This technology has significantly increased the reflectance above 15 keV. Figure 3.13 compares the effective area of *NuSTAR* with those of other X-ray focusing telescopes. Thus, *NuSTAR* achieves significant effective areas above

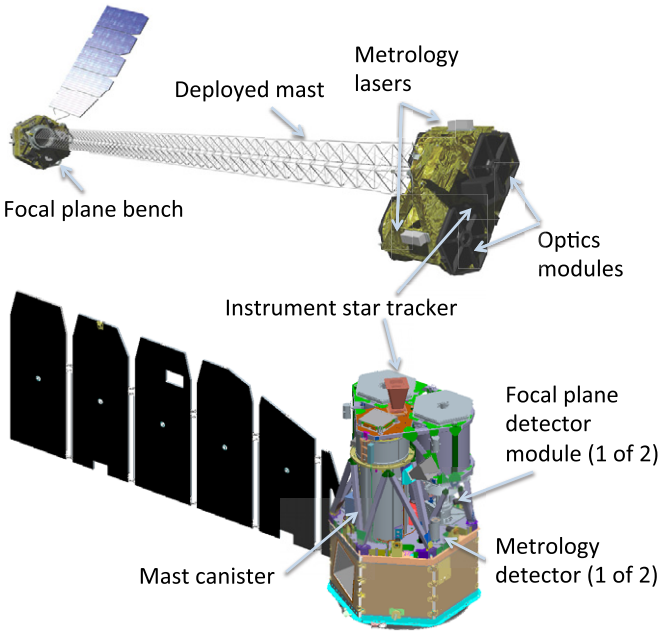

Figure 3.12. Illustration of the NuSTAR observatory (Harrison et al. 2013). In the bottom panel, the spacecraft is shown in stowed configuration, while it is shown in deployed configuration in the top panel.

15 keV where the telescope on-board the other missions, all relying only on the total reflection, no longer work. The inner 89 shells are coated with depth-graded Pt/C multilayers which reflect the higher energy X-ray photons up to Pt K-edge at 78.4 keV, while the outer 44 shells are coated with depth-graded W/Si multilayers to reflect lower energy photons below W K-edge at 69.5 keV. The effect of the former can be seen in figure 3.13 as a sudden drop of the effective area at 78.4 keV.

The capability of the *NuSTAR* X-ray telescopes is summarized in figure 3.14. The left panel shows the enclosed energy fraction as a function of diameter, obtained from an observation of the bright point source GRS 1915+105. The angular resolution of the X-ray telescope is thus 58″ in half power diameter (diameter where the enclosed fraction hits 0.5). The right panel of figure 3.14 presents the effective area as a function of the off-axis angle, so-called vignetting function. Because the grazing-incidence angles (hence reflectivity) of incoming X-ray photons depend both on the X-ray off-axis angle and the positions on the mirror shells, the effective area decreases significantly as the off-axis angle of the incident X-ray becomes larger than 2′(vignetting effect). The vignetting effect becomes severer toward higher energies, because the allowed grazing angle decreases. For example, the angle where the effective area becomes 50% is $\sim 10'$ at 10 keV, whereas it is $\sim 6'$ at 68 keV.

3.3.3 Focal Plane Module (FPM)

NuSTAR carries two pairs of identical X-ray detectors on the focal planes of the respective X-ray mirrors. They are called Focal Plane Module (FPM) A and B . The FPM is designed to achieve a wide energy coverage of $3 - 80$ keV with good energy resolution (< 1 keV FWHM). These were realized by employing CdZnTe (CZT) pixel detectors, which are characterized by high atomic numbers (48 for Cd and 52 for Te) and relatively wide energy gap (1.5 eV) which enables operation

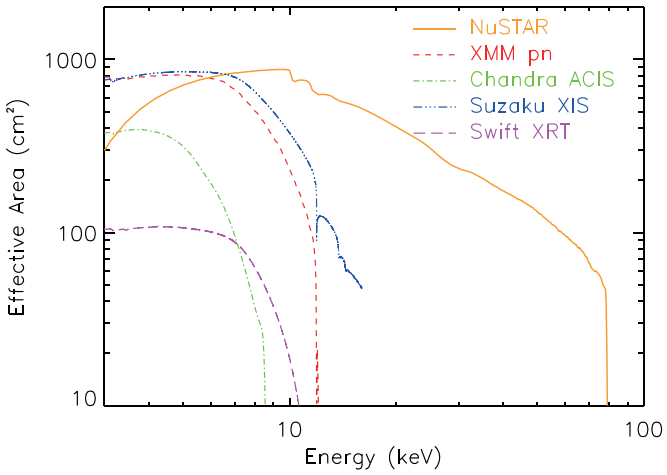

Figure 3.13. The effective area of *NuSTAR* (orange) in comparison with those of other focusing X-ray telescopes (Harrison et al. 2013).

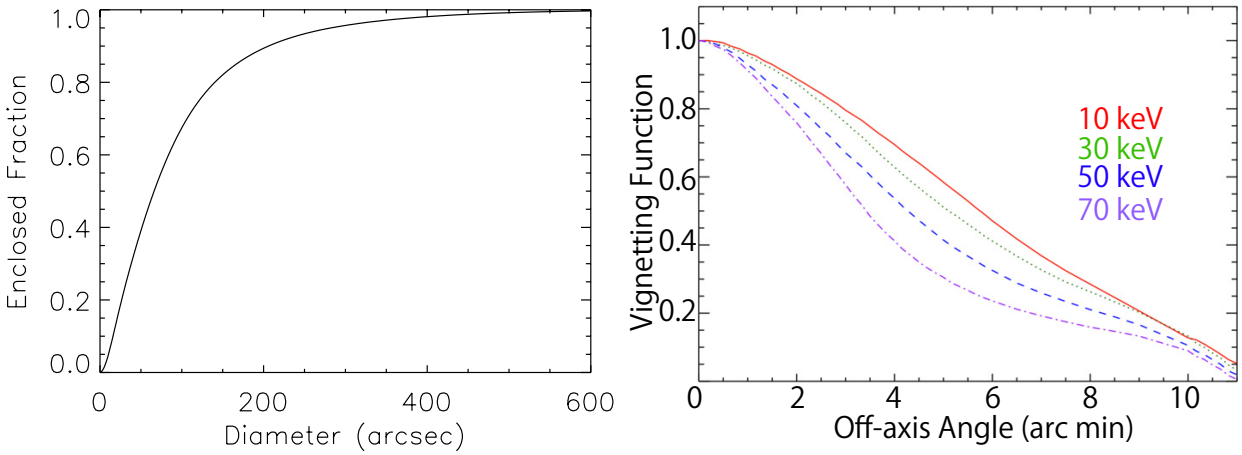

Figure 3.14. Left: Enclosed energy fraction as a function of the diameter. Right: Changes in the effective area as a function of the off-axis angle. Results at several energies are shown in different colors (Harrison et al. 2013).

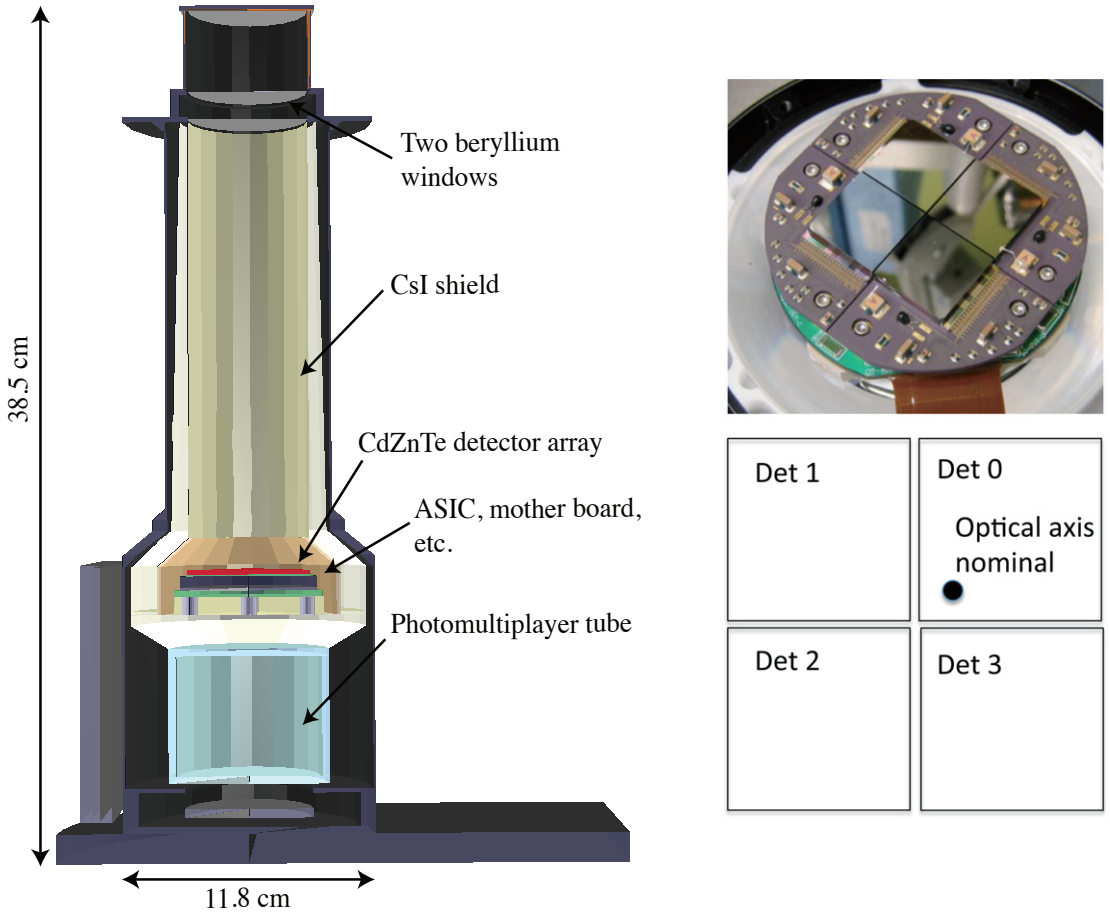

Figure 3.15. Left: A cross-sectional view of the FPM model (Kitaguchi et al. 2011). Right top: A photograph of the CZT pixel detector array. Right bottom: Configuration of the CZT (Harrison et al. 2013).

at near room temperature. The left panel of figure 3.15 shows a cross-sectional view of the FPM. The CZT pixel detector array is surrounded by a shield unit consisting of CsI scintillators and a photo-multiplayer tube. Non-celestial (background) events detected by CZT modules, such as non-aperture Gamma-ray photons and cosmic ray particles, can be rejected by screening the events that are coincident with this surrounding CsI shield unit.

The CZT hybrid pixel detector, which serves as the main detector of each FPM, has a 2×2 array configuration as presented in the right top panel of figure 3.15. Each segment of this array is a 2 cm $\times$ 2 cm $\times$ 2 mm CZT crystal, to which 32×32 grid segmented anode is attached to form 1024 pixels with a pitch of 605 μm. These pixels provide two dimensional position information of individual hard X-ray photons, together with their pulse heights. The field of view of each FPM is $12' \times 12'$ and the nominal position of the optical axis is set to the position indicated in figure 3.15 (bottom right). Unlike the CCD camera readout, each pixel has its own independent amplifier, discriminator, and sample/hold circuit. This parallel readout scheme realizes a fast hard X-ray imager. If readout were slow, the CsI anti-coincidence shield would not work. The read out time is $\sim$ 2.5 ms per event, which makes the instrument pile-up free up to 10^4 counts sec^{-1}.

Figure 3.16 shows a comparison of background spectra screened with different background-rejection criteria. The background spectra were obtained with series of blank sky observations.

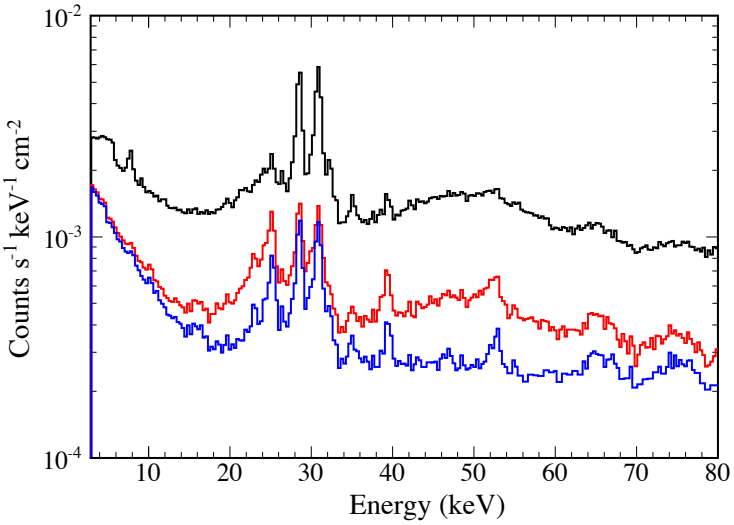

Figure 3.16. In-orbit background spectra of the FPM taken from Kitaguchi et al. (2014). The data were obtained in observations of a blank sky. Black, red, and blue representing background spectra without any rejection with CsI shield, with anti-coincidence rejection, and with all background rejection.

Almost in whole effective energy band, the background continuum decreases by a factor of $\sim 1/5$ by taking the anti-coincidence of the CsI shield. The remaining line features at 29 and 31 keV are fluorescence X-rays from I and Cs in the shield, respectively. Other lines are those due to detector activation. The anti-coincidence shield is inefficient to reduce these background sources, but some events from the latter component can be removed with interaction depth cut method, of which the effect can be seen in changes of the spectra from red to blue. Thus, by applying several background rejection techniques, the *NuSTAR* FPMs achieve low back ground level of $\leq 10^{-3}$ counts sec^{-1} keV^{-1} cm^{-2} in orbit.

4 OBSERVATION

In the present thesis, we would like to study the X-ray spectra of a sample of ULXs from two prospects. One is luminosity-dependent changes in their spectral continua. As described in section 2.1.2, Galactic BHBs show spectral state transitions at particular Eddington ratios L_X/L_{edd} (e.g., from LHS to HSS is at $L_X/L_{edd} \sim 0.1$). If this is so the case with ULXs, possible spread in their transition luminosity will tell us about the underlying scatter in their masses, since L_{edd} is proportional to the mass. In order to do this, we fit various spectra of several representative ULXs with a physical model that has been well established through the research of BHBs; this enables us to characterize the spectral shapes quantitatively, without relying on any specific physical accretion models.

The other prospect is their local spectral structures. A unique characteristic of ULXs is their lack of local spectral features, including especially those from Iron $K\alpha$ which are widely seen in other X-ray binaries. The faintness of these local structures gives us information about their surrounding environment, such as the amount of matters and geometrical conditions of their accretion flows. Even upper limits will allow us to derive some useful constraints on their accretion mechanisms. Thus we focus also on their local spectral features, and discuss.

Since the studies require a relatively large number of high statistics X-ray spectra, we utilized archival data of *XMM-Newton*, *Suzaku*d, and *NuSTAR*; the former two spacecrafts provide sensitive coverage to the $0.3 - 10$ keV range, and the latter $3 - 20$ keV. For the same reason, we focused only on representative ULXs in nearby galaxies, which are luminous and have fluxes high enough to grasp their spectral shapes. The following sections describe details of target selection and characteristics of the selected objects.

4.1 Targets to be Studied

4.1.1 Target selection criteria

To unambiguously compare ULXs with ordinary BHBs, we focus on ULXs whose maximum luminosity exceeds $\sim 2.5 \times 10^{39}$ erg sec^{-1}, which corresponds to the Eddington limit for the heaviest stellar mass ($\sim 20\ M_\odot$) BHs. In addition, in order to satisfy the required photon statistics as well, the ULX sample has to be restricted to those associated with nearby galaxies. According to the sensitivity of the *XMM-Newton* EPIC in $2 - 10$ keV band, the detectable minimum flux in a typical exposure time, $\sim$a few tens ks, is $\sim 10^{-14}$ erg cm^{-2} sec^{-1} (Walton et al. 2001). Since we need to perform detailed spectral studies, the target ULXs should have X-ray fluxes at least two orders of magnitude higher than this. From these criteria, our sample should consist of within a distance of ~ 5 Mpc. Finally, we select ULXs that have been observed more than twice in total, because we also focus on spectral variability.

Table 4.1: List of the selected ULXs and their basic information.

host galaxy	morphology	$N_{\rm H}{}^{a}$	distance (Mpc)	source name	R.A. (deg)	Dec. (deg)
M33	SA(s)cd	4.4	0.88	X-8	23.462	+30.660
NGC 253	SAB(s)c	1.7	3.2	ULX1	11.844	-25.347
Holmberg II	Im	3.9	3.3	X-1	124.871	+70.705
IC 342	SAB(rs)cd	34.5	3.3	X-1	56.482	+68.082
Holmberg IX	dl	4.3	3.4	X-1	149.472	+69.063
NGC 4190	Im	2.1	3.5	X-1	183.439	+36.63
NGC 1313	SB(s)d	3.6	4.13	X-1	49.583	-66.486
NGC 1313				X-2	49.593	-66.601
M83	SAB(s)c	3.8	4.61	ULX1	204.334	-29.897
M83				ULX2	204.271	-29.869

a: Galactic column density of equivalent Hydrogen in units of 10^{20} cm^{-2} (Dickey and Lockman 1990).

4.1.2 Target selection

Applying the above target selection criteria to the *XMM-Newton*, *Suzaku*, and *NuSTAR* archives, we are left with 10 ULXs as listed in table 4.1. They reside in 8 galaxies, with NGC 1313 and M83 hosting more than one of the selected objects. Four host galaxies are all spirals, with their morphology ranging from Sab to Scd. Basic information of the individual data sets is summarized in table 4.2, table 4.3, and table 4.4, separately for the three archives.

Table 4.2: Observational log of *XMM-Newton*.

Host galaxy	ObsID	R.A. (deg)	Dec. (deg)	Observation Start yyyy/mm/dd hh:mm:ss	Exposure (ks)
NGC 1313	0150280301	49.66304	-66.59972	2003/12/21 01:54:45	10.3
	0150280401	49.66196	-66.60047	2003/12/23 04:50:43	14.1
	0150280601	49.65758	-66.60817	2004/01/08 03:30:34	14.8
	0150281101	49.65250	-66.61319	2004/01/16 23:38:52	7.0
	0205230301	49.5170	-66.60464	2004/06/05 06:08:51	10.0
	0205230401	49.55733	-66.57292	2004/08/23 05:44:43	14.9
	0205230501	49.65583	-66.58697	2004/11/23 06:59:33	14.0
	0205230601	49.63488	-66.62122	2005/02/07 11:35:10	12.4
	0301860101	49.42263	-66.57953	2006/03/06 16:43:12	19.9
	0405090101	49.59296	-66.47497	2006/10/15 23:44:33	120.3
	0693850501†	49.63108	-66.49931	2012/12/16 16:00:25	122.1
	0693851201†	49.63305	-66.50272	2012/12/22 15:45:31	123.2
	0722650101	49.33767	-66.55542	2013/06/08 05:21:44	28.8

Table 4.2: Continued

Host galaxy	ObsID	R.A. (deg)	Dec. (deg)	Observation Start yyyy/mm/dd hh:mm:ss	Exposure (ks)
	0742590301†	49.50163	-66.49044	2014/07/05 22:54:38	60.0
Holmberg IX	0112521001	149.46213	69.03264	2002/04/10 16:58:14	7.8
	0657801801	149.21079	69.09094	2011/09/26 04:17:58	20.0
	0693850801†	149.47125	69.09203	2012/10/23 04:17:03	9.9
	0693851001†	149.46817	69.09231	2012/10/27 04:04:42	12.0
	0693851701†	149.44925	69.09156	2012/11/12 03:04:01	8.0
	0693851801†	149.44767	69.09117	2012/11/14 02:55:07	11.6
	0693851101†	149.44658	69.09083	2012/11/16 02:52:38	11.4
Holmberg II	0112520601	124.8950	70.67828	2002/04/10 12:31:19	5.2
	0112520701	124.90204	70.67975	2002/04/16 12:06:26	10.0
	0112520901	124.8760	70.73356	2002/09/18 02:10:13	5.0
	0200470101	124.90079	70.67844	2004/04/15 20:08:43	77.4
	0561580401	124.87692	70.67714	2010/03/26 09:20:48	46.1
	0724810101†	124.88775	70.73364	2013/09/09 06:33:44	10.2
	0724810301†	124.87921	70.73342	2013/09/17 06:03:28	10.0
IC 342	0206890101	56.57808	68.11403	2004/02/20 06:30:24	20.3
	0206890201	56.47533	68.15733	2004/08/17 18:48:16	19.7
	0206890401	56.57175	68.11256	2005/02/10 17:26:36	18.6
	0693850601†	56.43046	68.10256	2012/08/11 20:06:44	51.6
	0693851301†	56.43146	68.10375	2012/08/17 19:48:41	50.5
M83	0110910201	204.24417	-29.83581	2003/01/27 10:54:53	27.0
	0723450101	204.2760	-29.89686	2013/08/07 16:38:29	50.0
	0723450201	204.26263	-29.84075	2014/01/11 11:59:44	54.9
	0729561201	204.28029	-29.89628	2014/07/06 17:45:59	26.8
	0729561001	204.26696	-29.84067	2015/02/02 16:00:02	27.9
NGC 4190	0654650101	183.44208	36.60292	2010/06/06 12:08:27	7.7
	0654650201	183.44233	36.60336	2010/06/08 11:14:45	21.9
	0654650301	183.43221	36.65992	2010/11/25 01:24:51	16.7
M33	0102640101	23.43317	30.67694	2000/08/04 05:17:12	13.3
	0102640301	23.35442	30.88608	2000/08/07 01:03:49	10.0
	0141980801	23.49225	30.64731	2003/02/12 15:17:46	8.5
NGC 253	0110900101	11.87613	-25.26478	2000/12/13 23:37:50	0.2
	0152020101	11.87513	-25.29269	2003/06/19 08:13:24	3.6
	0304851101	11.91583	-25.30244	2005/12/16 20:14:55	21.2
	0304851001	11.91313	-25.30625	2006/01/06 04:12:06	9.9

†: Observations that are jointed with *NuSTAR*.

Table 4.3: Observational log of *Suzaku*.

Host galaxy	ObsID	R.A. (deg)	Dec. (deg)	Observation Start yyyy/mm/dd hh:mm:ss	Exposure (ks)
NGC 1313	100032010	49.5282	-66.5443	2005/10/15 13:21:13	32.9
	703010010	49.6088	-66.5434	2008/12/05 23:03:23	91.5
	709023010	49.4840	-66.5362	2014/05/27 05:41:09	107.3
M33	704016010	23.4896	30.5679	2010/01/11 01:47:07	82.5

†: Observations that are jointed with *NuSTAR*.

Table 4.4: Observational log of *NuSTAR*.

Host galaxy	ObsID	R.A. (deg)	Dec. (deg)	Observation Start yyyy/mm/dd hh:mm:ss	Exposure (ks)
NGC 1313	30002035002	49.6268	-66.5225	2012/12/16 13:56:07	100.8
	30002035004	49.6351	-66.5268	2012/12/21 20:06:07	127.0
Holmberg IX	30002033006	151.1143	68.5532	2012/11/11 16:51:07	35.2
	30002033008	151.1297	68.5537	2012/11/14 01:31:07	14.5
	30002033010	151.1297	68.5537	2012/11/15 17:51:07	49.0
Holmberg II	30001031002	124.8517	70.684	2013/09/09 05:41:07	31.3
	30001031003	124.9776	70.693	2013/09/09 17:31:07	79.4
	30001031005	124.9655	70.7048	2013/09/17 04:46:07	111.1
IC 342	30002032002	58.4077	67.7677	2012/08/10 08:21:07	21.0
	30002032005	58.4635	67.844	2012/08/16 08:26:07	127.4

4.2 Descriptions of the Selected ULXs

4.2.1 IC 342 X-1/X-2

These are two ULXs both residing in the starburst Scd galaxy IC 342. Figure 4.1 is a superposition of optical and X-ray image of IC 342. The ULXs are both located in the arms of the galaxy with a $\sim 6'$ separation from each other. The X-rays from these sources suffer strong absorptions due to the low Galactic latitude of IC 342 ($b \sim 11^\circ$). Both sources are known to show strong variability. The average $0.3-10$ keV luminosity of X-1 is $L_X \sim 5 \times 10^{39}$ erg sec^{-1} and reaches $L_X = 1.4 \times 10^{40}$ erg sec^{-1} at maximum, while X-2 is generally slightly more luminous, $L_X \sim 8 \times 10^{40}$ erg sec^{-1} in average and $L_X \sim 3 \times 10^{40}$ erg sec^{-1} at maximum (Yoshida et al. 2012, Rana et al. 2015). They are also known to change their spectral shapes between the two typical ones described in section 2.2.1, namely, the Disk-like state and the PL state (Mizuno et al. 2001, Yoshida et al. 2013).

Sugiho et al. (2001a) detected a possible periodicity in an X-ray light curve of X-1 acquired in the Disk-like state. The period was 31 or 41 hours, which are both reasonable as the orbital period of a binary system with a BH and a main-sequence companion star. Although the origin of the

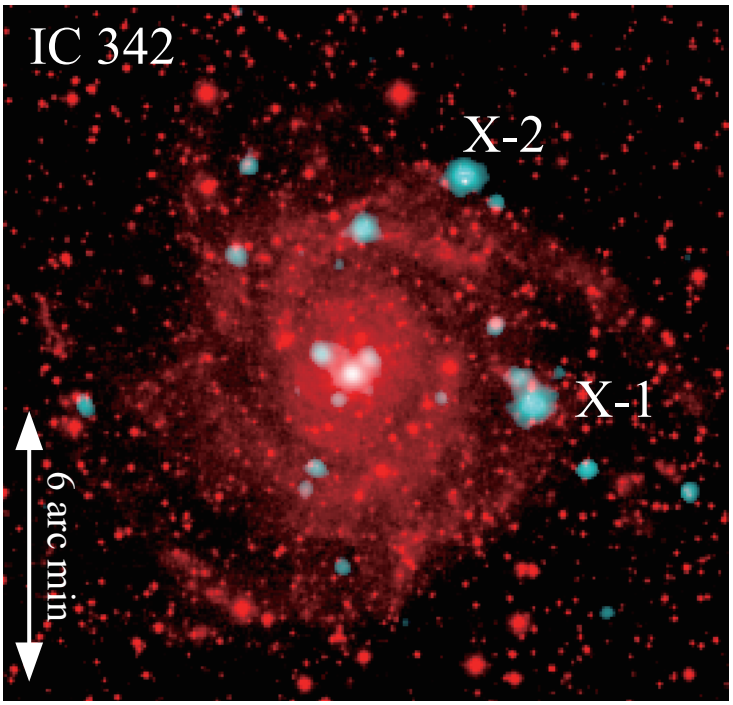

Figure 4.1. An optical image of the IC 342 galaxy (red) taken from the Digital Sky Survey. A $0.3 - 12$ keV X-ray image of the *XMM-Newton* EPIC PN is overlaid in cyan.

periodicity is still uncertain, assuming that the system is close to exchange the mass via Roche-Lobe overflow yields the BH, as in X-1 as $\sim 100\ M_{\odot}$, which supports the intermediate mass BH scenario.

4.2.2 NGC1313 X-1/X-2

These are ULXs in the spiral galaxy NGC 1313 with a separation of $\sim 6'$ from each other. Both of these ULXs are known to be variable, typically by a factor of 5 or so. For example, X-1 reaches $L_{\rm X} = 3.5 \times 10^{40}$ erg sec^{-1} at maximum, while the average is $L_{\rm X} \sim 3 \times 10^{39}$ erg sec^{-1} (Mizuno et al. 2007). Figure 4.2 show two X-ray images of the NGC 1313 obtained on different epochs. Thus, X-2 is normally dimmer than X-1 (left panel), but sometimes it becomes comparable to or event brighter than X-1 (right panel).

Since X-1 and X-2 are bright and relatively nearby, they have also been extensively observed. Pinto et al. (2016) successfully detected blue-shifted narrow emission/absorption line features from highly ionized neon, oxygen, and iron by accumulating large amount of archival data sets of the *XMM-Newton* RGS. Along with NGC 5408 X-1, this was the first detection of any kind of local spectral features in the X-ray spectra of ULXs, but the features are extremely weak ($\sim$ few eV in equivalent width) and their origin is yet to be identified.

4.2.3 Holmberg IX X-1

Holmberg IX X-1 is a ULX in the irregular dwarf galaxy Holmberg IX, which is a companion to the nearby galaxy M81. Since the host galaxy Holmberg IX was recognized only recently, this

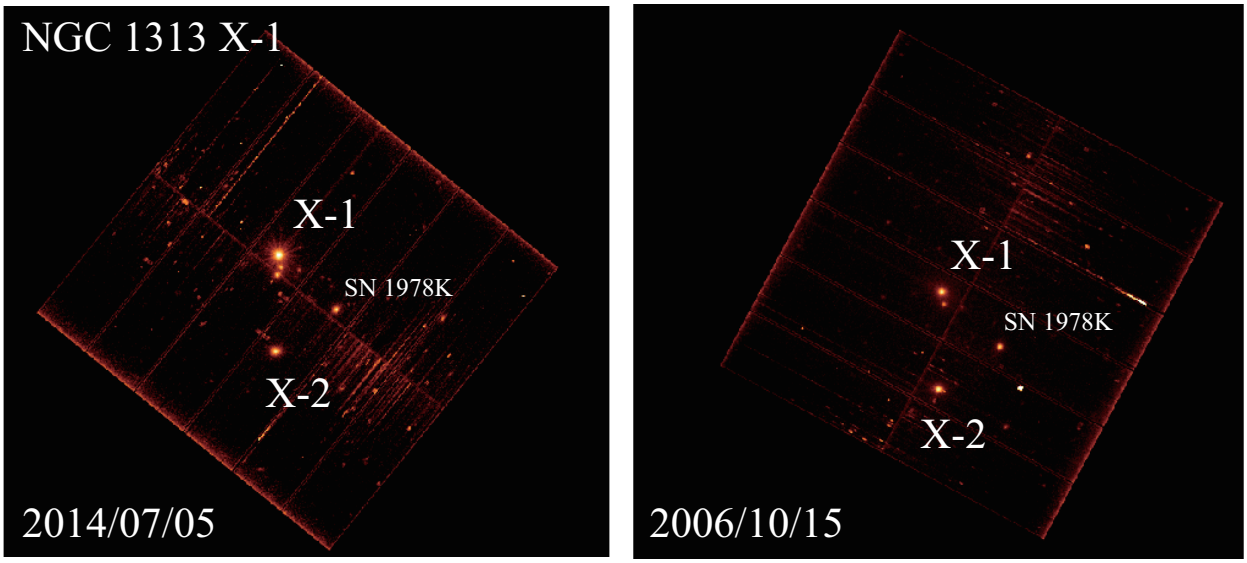

Figure 4.2. X-ray images of NGC 1313 observed with the *XMM-Newton* EPIC PN in $0.3 - 12$ keV band. Images from two different observations are shown.

ULX was once considered as an object belonging to the M81 galaxy, namely as M81 X-6, or even a background quasar (Ezoe et al. 2001). It is one of the brightest ($L_X \sim 1 - 3 \times 10^{40}$ erg sec^{-1}) ULXs in nearby galaxies, and accordingly has the highest flux ($0.3 - 10$ keV flux $\sim 10^{-11}$ erg cm^{-2} sec^{-1}) among the known ULXs. It has been extensively studied with many X-ray satellites. In an observation performed in 1999 with *ASCA*, it was relatively luminous ($L_X = 2 \times 10^{40}$ erg sec^{-1}) and showed a Disk-like state spectrum which can be fitted with an MCD model with a peak temperature of 1.3 keV (Tsunoda et al. 2006). However, since, it has been mostly residing in the PL state (Vierdayanti et al. 2010, Luangtip et al. 2016).

Since this ULX shows relatively hard ($\Gamma = 1.5 - 1.8$) spectra, it is rich in photons with energies above the iron K-edge (7.13 keV). Therefore, it is a favorable target of searching for spectral features from irons, including Kα fluorescence X-rays, resonant absorption lines, and K-shell edge absorption, which are commonly seen in other accreting objects. In order to detect these, Walton et al. (2013) conducted a large observational program with *Suzaku* incorporating 3 separate pointings. Figure 4.3 is an actual X-ray light curve of X-1 taken with XIS0 in one of three pointings. As described in section 3.2.1, observations with *Suzaku*, having a near-Earth orbit, are periodically interrupted by Earth occultations and passages through the SAA, which can be seen as data gaps in the light curve. Thus, the net exposure time of an observation with *Suzaku* is typical reduced by a factor of 1/2 from the actual gross duration. The campaign by Walton et al. (2013) had a gross and net exposure of ~ 11.5 day and ~ 6 day, respectively, which are ~ 5 times longer than the request of average *Suzaku* proposals. Despite such a historically long observation, Walton et al. (2013) obtained only stringent upper limits of 30 eV in equivalent width for any narrow emission/absorption line features.

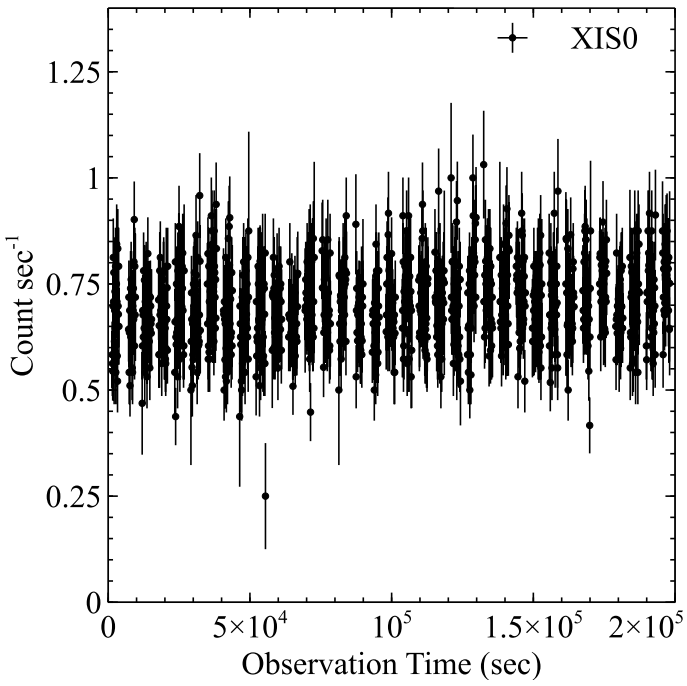

Figure 4.3. A full-band ($0.1 - 12$ keV) light curve of the *Suzaku* XIS0, from an observation of Holmberg IX X-1, ObsID 707019030. The photons were accumulated over a circular region of $3'$ radius. The width of each bin is set to 200 sec.

4.2.4 Holmberg II X-1

Just like Holmberg IX X-1, this is also a ULX in the irregular galaxy Holmberg II. Its average luminosity is $\sim 8 \times 10^{39}$ erg sec^{-1}, and at the maximum it reaches 10^{40} erg sec^{-1}. Thus, from the luminosity viewpoint, it is intermediate among the ULX sample utilized in the present study. In contrast to other ULXs (e.g., Holmberg IX X-1, NGC 1313 X-1, and IC 342 X-1) showing hard ($\Gamma = 1.5 - 1.8$) PL state spectra, Holmberg II X-1 often show considerably softer ($\Gamma = 2.0 - 2.4$) spectra, which is likely to be the subgroup of the PL state.

Holmberg II X-1 is also known as a strong radio source, and some observations were performed with several radio observatories. Figure 4.4 is a radio image from one of such observations. Although ULXs are generally radio-faint objects, this source exhibits an exceptionally strong radio emission, as shown in figure 4.4. The radio emission of Holmberg II X-1 has a bipolar radio lobe structure with a size of 38.5 pc extending from the center source region. The spectra of those lobes are reproduced with a model of synchrotron emission, and its photon index is consistent with the typical value of the jet emissions from accreting BHs. The power of the jet is estimated to be $\sim 2 \times 10^{39}$ erg sec^{-1}, which is comparable to the X-ray luminosity $L_{\rm X} \sim 4 \times 10^{39}$ erg sec^{-1} of the central ULX. This suggests that Holmberg II X-1 harbors a BH with a mass of $\geq 25\ M_\odot$ (Cseh et al. 2014).

4.2.5 M33 X-8

M33 X-8 is a ULX located at central position of the local group spiral galaxy M33. Although it was at first considered as an AGN, the imaging capability of the fourth Japanese X-ray satellite *ASCA* up to ~ 10 keV revealed that its $1 - 10$ keV spectrum is different from those of AGNs (Takano et

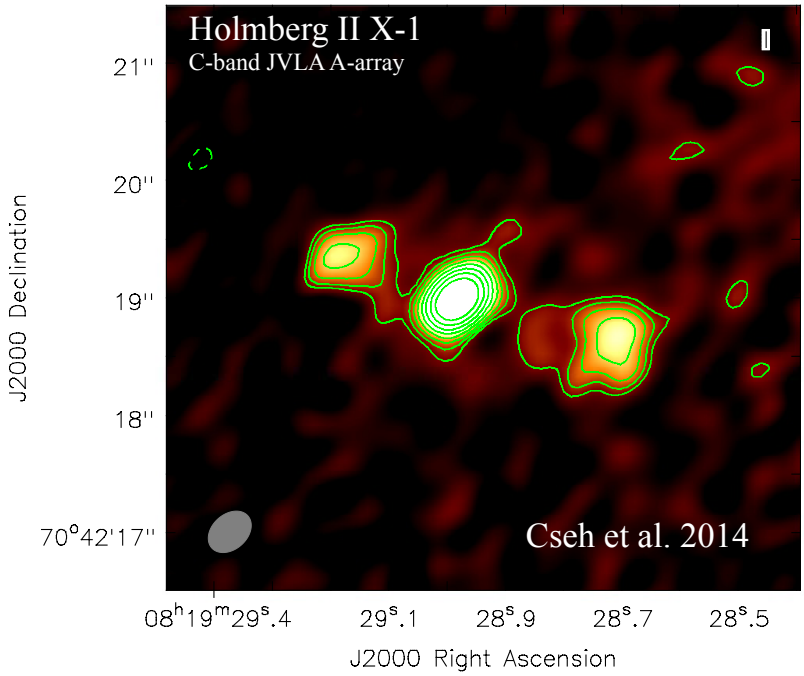

Figure 4.4. A radio image of Holmberg II X-1 taken with the Very Large Array observatory (Cseh et al. 2014). An image contour is drawn in green as well.

al. 1994). It is now regarded as the closest and also the dimmest ($L_X \sim 10^{39}$ erg sec^{-1} in average) ULX ever observed. Therefore, it is expected to be an object connecting ULXs and ordinary BHBs.

Another unique characteristics of M33 X-8 is that it has been residing in the Disk-like state since it has been discovered. Although the available past observation indicate its variability by a factors of 1.8, it has never showed the PL state like spectra (Middleton et al. 2011).

4.2.6 Others

NGC 4190 X-1

This is a ULX in the dwarf galaxy NGC 4190 located at a distance of 3.5 Mpc. Its typical luminosity is $\sim 5 \times 10^{39}$ erg sec^{-1}, which is in intermediate regime among the present sample. It is known to show relatively hard $\Gamma = 1.5 - 1.7$ continuum.

NGC 253 ULX1

This is a ULX resided in the starburst galaxy NGC 253. The host galaxy has two ULXs, one is the source we are now focused, ULX1, and another is a less luminous one called ULX2. Since ULX2 are dimmer than the threshold luminosity that we settled in the target selection criteria, we have excluded the source from the present analysis.

M83 ULX1/ULX2

These are ULXs in the face-on spiral galaxy M83. While ULX1 is located near center region of the galaxy, ULX2 is in the edge region of a spiral arm. Both are similarly dim ULX with typical luminosity of $\sim 10^{39}$ erg sec^{-1}, which are comparable with that of M33 X-8.

4.3 Data Reduction

In X-ray astronomy, the observational data sets are generally handled in a format called Flexible Image Transport System (FITS). An example of FITS format data is shown in figure 4.5. FITS files consist of multiple rows and columns. Each of the row represents single X-ray event, and each column stacks the individual physical values for respective X-ray event such as the arrival position (X and Y in figure 4.5), the pulse height (or energy; PHA in figure 4.5), and the arrival time of the photon. Generally, the primary data sets obtained from the satellites, so called "raw data", cannot be immediately used in the analysis, because they are uncalibrated and also include large number of unusable events. Therefore, we have to extract only appropriate events from the whole data and converted them to calibrated formats via procedures called pipeline processes. The pipeline processes can be performed by running unique software tools developed by the individual satellite teams in well defined manners. This provides us with the basic data sets which can be used in scientific researches. Here, we devote this section for summarizing the data reduction performed in each satellite.

4.3.1 Data reduction in the *XMM − Newton* EPIC

The obtained raw data sets are transmitted from the *XMM-Newton* spacecraft and then stored at ESA's *XMM-Newton* Science Archive (XSA) web server as Observation Data Files (ODF). This ODF is pipeline processed by a software called the Science Analysis Software (SAS) which is developed by ESA. The SAS removes unusable events (e.g., flaring hot pixels, dead column, and bad grade events), converts pulse height into energy, and corrects the attitude of the satellite by referring an appropriate calibration data inside a data base called Current Calibration Files (CCF). In the present thesis, the pipeline process was performed by the SAS version xmmsas_20160201_1833-15.0.0 with the CCF released on 2016 January 22.

As described in section 3.2.1, due to the highly elongated orbit, the EPIC data sets can be contaminated by the soft proton flare events if the data sets were taken during when the spacecraft was outside the Earth's magnetospheric shield. Figure 4.6 shows a set of EPIC light curves at $>$ 10 keV, which was taken in an observation of ULX Holmberg IX X-1. Since the X-ray mirror telescopes have approximately zero effective area at $>$ 10 keV, the light curves are mostly following the variability of the background components. As can be seen in the latter half of the exposure, count rate suddenly increases in all EPIC detectors simultaneously, while it is rather stable at few to 1 counts sec^{-1} level in the other half. During these flares, the data is dominated by highly variable background events, which makes the accuracy of the background level estimation extremely poor. Therefore, we excluded the intervals from the analysis in which the count rate is twice or more than that in the quiescent state.

File Edit Tools Help

Select All	X 1I pixel	Y 1I pixel	PHA 1I chan	PI 1I chan	TIME 1D s
Invert	Modify	Modify	Modify	Modify	Modify
1	695	1073	384	396	1.827001704084E+08
2	707	963	1767	1833	1.827001704084E+08
3	709	908	689	712	1.827001704084E+08
4	688	901	313	321	1.827001704084E+08
5	667	888	983	1018	1.827001704084E+08
6	632	842	815	843	1.827001704084E+08
7	475	748	352	362	1.827001704084E+08
8	515	700	3113	3233	1.827001704084E+08
9	507	678	1967	2042	1.827001704084E+08
10	643	533	248	254	1.827001704084E+08
11	751	955	812	795	1.827001704084E+08
12	797	936	631	617	1.827001704084E+08
13	716	656	431	421	1.827001704084E+08
14	788	488	2224	2185	1.827001704084E+08
15	474	1212	2024	2010	1.827001704084E+08
16	331	665	3330	3308	1.827001704084E+08
17	1014	631	1834	1827	1.827001704084E+08
18	705	1194	600	619	1.827001784084E+08
19	663	1088	288	295	1.827001784084E+08
20	650	962	210	214	1.827001784084E+08
21	714	950	1158	1200	1.827001784084E+08
22	955	723	2670	2625	1.827001784084E+08
23	769	583	266	258	1.827001784084E+08
24	685	321	250	242	1.827001784084E+08
25	400	825	1920	1906	1.827001784084E+08
26	306	525	3662	3638	1.827001784084E+08
27	1147	670	4095	4095	1.827001784084E+08

Figure 4.5. An example of the observation data in FITS format. An event file of the *Suzaku* XIS is shown here.

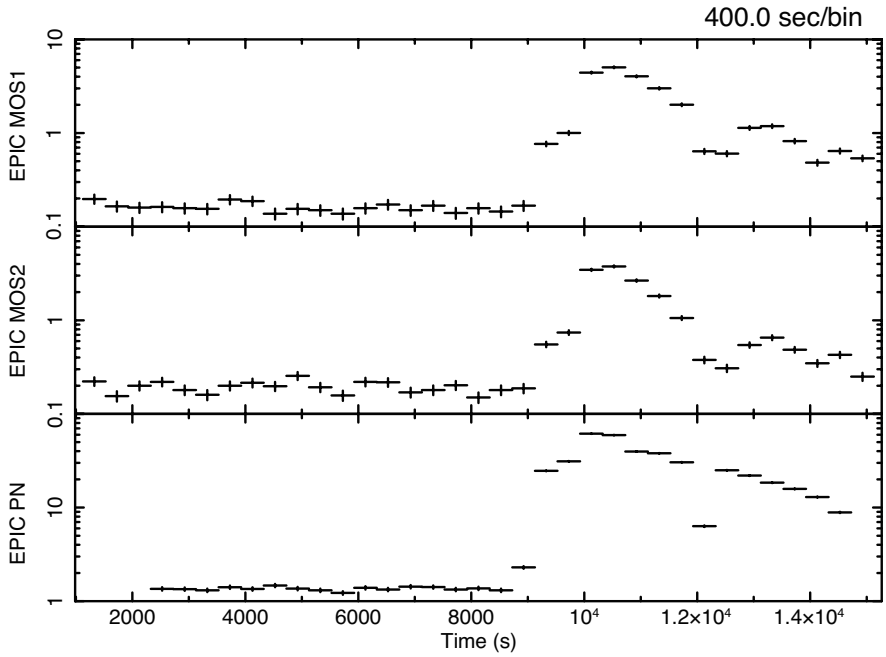

Figure 4.6. Light curves of the EPIC cameras at $\geq$ 10 keV.

Figure 4.7 shows background images of EPIC PN at the energies where the fluorescence X-rays are present. As described in section 3.2.3, the fluorescence X-rays show strong patterns in the images which are reflecting the structures of circuit board behind the CCD chips. Thus, the users are required to choose an appropriate region for extracting a background spectrum, in which the level of the fluorescence X-rays is approximately equivalent to that in the region where the observing source is present.

4.3.2 Data reduction in the *Suzaku* XIS

The pipeline process of the *Suzaku* data is performed by a specific software called "aepipeline". The software is developed by NASA and it is included in a software package called HEASoft which integrates all the softwares developed for NASA's high energy astrophysical missions. As is the case with the *XMM-Newton* SAS, the aepipeline does the calibration, attitude correction, and exclusion of unusable pixels (such as flickering pixels and dead columns) and bad grade events by referring calibration database files (CALDB) released by the *Suzaku* team. Although it is similar to the SAS in some extents, there are other different data reductions which are unique to the *Suzaku* satellite. Figure 4.8 shows a light curve of the XIS0 above 10 keV with no data reduction performed. Since the XRT has almost no effective area at this energy band, the variabilities which can be seen in the figure are not from the observing celestial object. As can be noticed from the periodicity, this background component strongly reflects the characteristics of the low orbit of *Suzaku*.

As described in section 3.2.1, since the orbit of *Suzaku* is inclined by 30° from the equatorial plane, the space craft periodically enters the SAA, where the Van Allen radiation belt is penetrating down to the height of the satellite orbit. Inside this particular region, the instruments are strongly bombarded by trapped cosmic particles, which cause an extreme increase in the background count

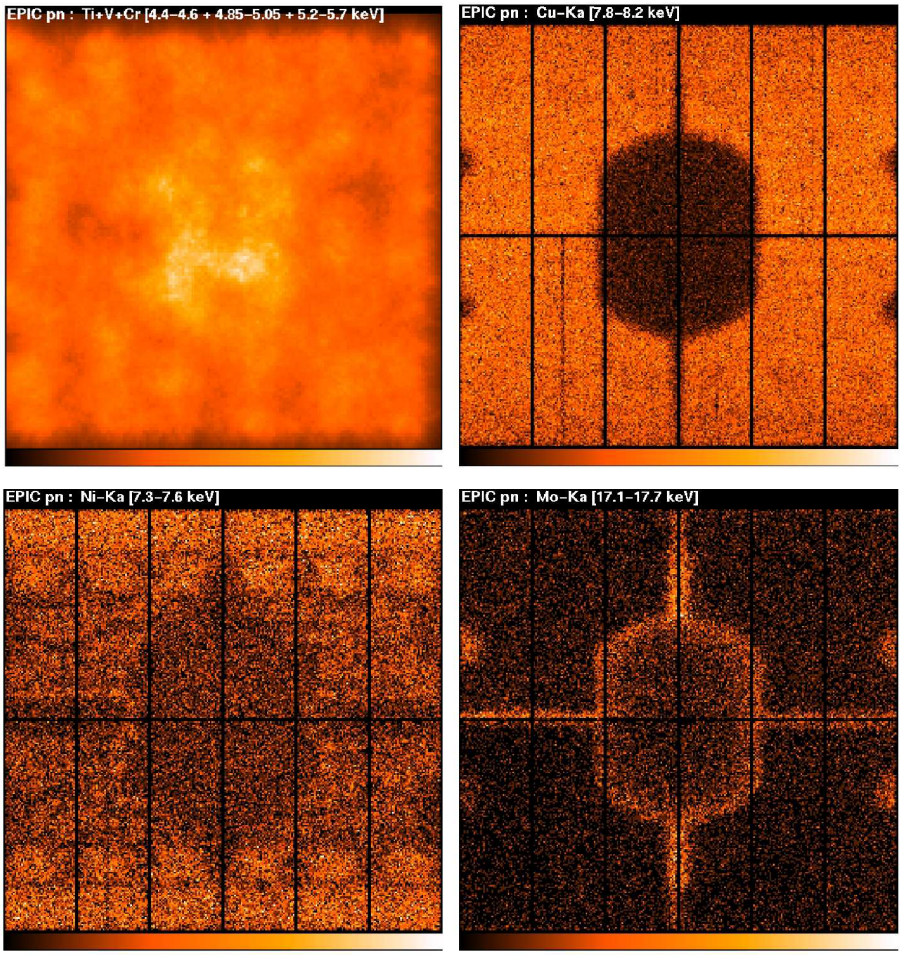

Figure 4.7. Instrumental background images of EPIC PN (*XMM-Newton* Calibration Technical Note; XMM-SOC-CAL-TN-0018).

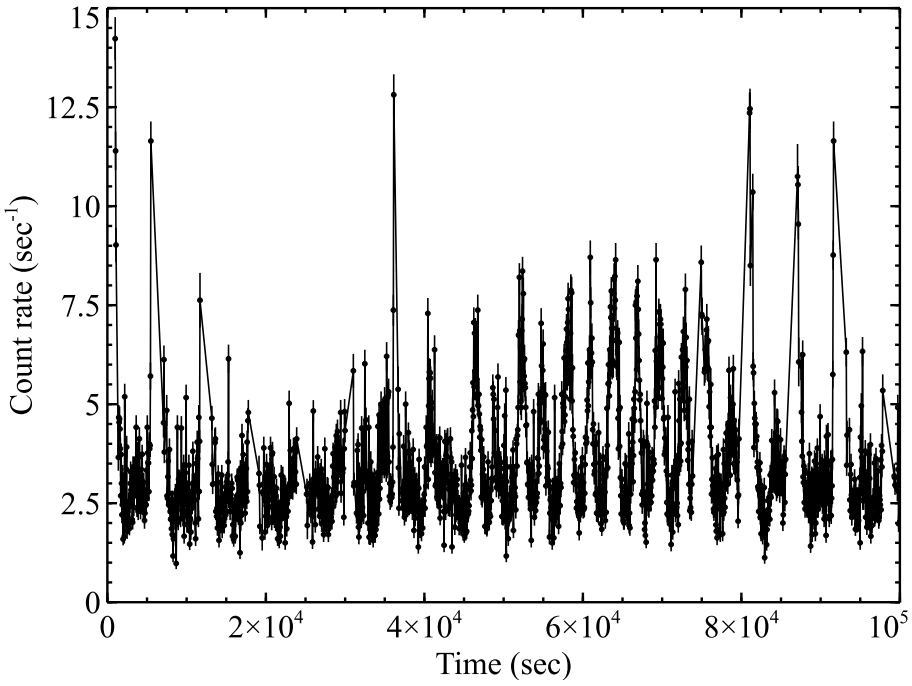

Figure 4.8. An unfiltered light curve of the XIS0 at $\geq$ 10 keV

rate just like the periodical spikes seen in figure 4.8. Since the data sets taken in the SAA are unusable, we need to exclude the corresponding time interval from the analysis.

Once the satellite is outside the SAA, then the amount of cosmic particle background is determined by the strength of the magnetospheric shield of Earth at that orbital position, which is called as Cut Off Rigidity (COR). The COR represents the minimum energy for the cosmic particles to penetrate the shield and reach the spacecraft. Therefore, the lower the COR at that position is, the higher the background becomes. The strength of the background component is known to vary by a factor of two in maximum (Tawa et al 2008). In order to minimize the background component, the data sets taken in intervals with low COR are also required to be excluded.

Earth itself also becomes a major background source in low orbit satellites like *Suzaku*, since the day Earth is a strong X-ray source due to irradiation. Figure 4.9 shows spectra of XIS1 taken with different elevation angles between telescopes bore sight and the limb of day Earth. As the elevation angle decreases, the fluorescence X-rays from oxygen and nitrogen in the Earth's atmosphere start to contaminate the XIS spectra. Hence, users are recommended to utilize only the events which are taken during the elevation angle of the telescope had larger value than $\sim 20^\circ$.

In order to take all the above into account, we have reduced our observational data with following criteria. In order to exclude the effects of the SAA, we discarded events taken during SAA and within 436 sec after exiting the SAA. After recommended values set by the *Suzaku* instrumental team, the minimum value for elevation and the COR are set to 20° and 6 GV, respectively. Also, the data sets taken during time intervals in which the observing object was occulted by Earth are discarded. The data reduction are performed by aepipeline included in HEASoft version 6.18. As for calibration data base (CALDB) of XRT and XIS, we utilized CALDB release version 20110630 and 20160204, respectively.

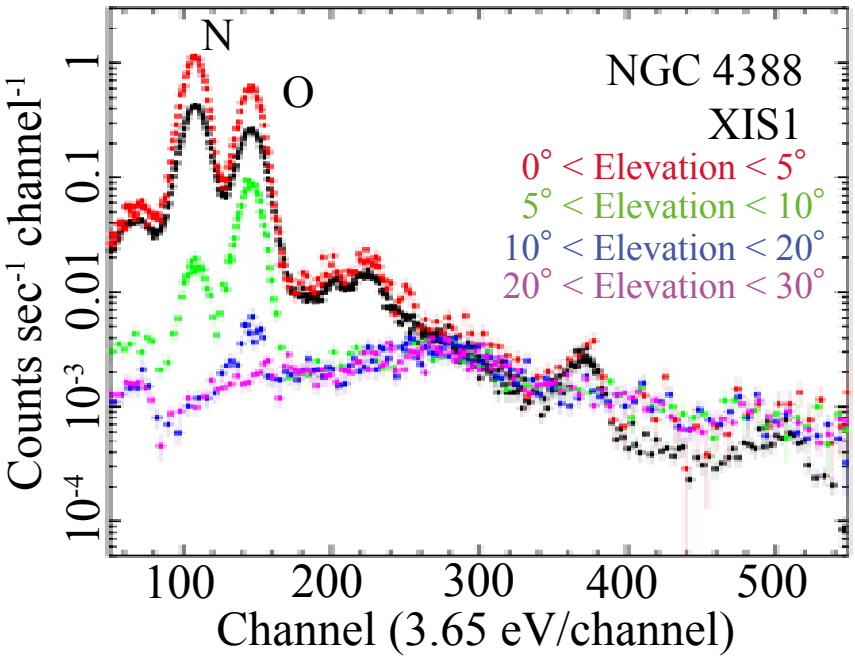

Figure 4.9. Spectra of XIS1 taken during observations of NGC 4388 (Tawa et al. 2006). The colors represents the difference of the satellite's elevation angle from day Earth's limb.

4.3.3 Data reduction in the *NuSTAR* FPM

For *NuSTAR*, NASA has developed a pair of pipeline process tools called "nupipeline" and "nuproducts", which are also included in HEASoft package like *Suzaku* aepipeline. The former is responsible for the fundamental data reductions. It corrects for the satellite attitude, excludes events from unusable pixels, rejects unwilling events like cosmic rays and fluorescence X-rays by applying various cuts criteria, and performs gain corrections to convert pulse height value into energy scale. On the other hand, the latter is in charge of rather advanced data reductions such as time interval screening, calculation of the SAA passages, region/energy screening, and dead time corrections. In the present thesis we performed the pipeline process with utilizing HEASoft version 6.18 and CALDB for FPM released on 2016/03/25.

Since *NuSTAR* has a similarly low orbit as *Suzaku*, the Earth occultation and the SAA passages are required to be handled properly as well. In the present thesis, we followed the recommended values set by the *NuSTAR* team. We have discarded the data taken during the time when satisfies either of the following conditions.

- When Earth is in the field of view.
- When the elevation angle between the telescope and the Earth's limb is $< 3^{\circ}$.
- When the satellite was in the SAA.
- When the on-board calibration source is in the field of view.
- When the nominal position of the detector went outside the defined limit due to wobbles of the optical bench.

5 DATA ANALYSIS AND RESULTS

In this chapter, we analyze X-ray data of the ULX sample defined in section 4.1.1. In order to grasp their basic characteristics, and to outline our data-analysis strategy, here we begin with a representative ULX, IC 342 X-1. Then, the other sources are studied in the following sections.

5.1 IC 342 X-1

This is a typical ULX in the face-on galaxy IC 342. As revealed with *ASCA* (Kubota et al. 2002), it was observed to switch between the two spectral states, the Disk-like state and the PL state (section 2.2.1).

5.1.1 Intensity variations

From 2004 to 2012, IC 342 X-1 was observed 6 times in total; four times with *XMM-Newton*, and twice with *NuSTAR* combined with *XMM-Newton*. Its X-ray intensity was stable within $\sim 10\%$ in each observation which lasted for a few tens to a hundred ks. However, as can be seen in figure 5.1, its luminosity changed by more than a factor of three on moths to year time scales. Since the observed luminosity range, $(3-9) \times 10^{39}$ erg sec^{-1}, encompasses that observed with *ASCA* (Kubota et al. 2002), it is possible that the source similarly made state transitions among those observations.

5.1.2 Broad band X-ray spectra

Figure 5.2 presents the X-ray spectra in the 6 observations, all shown after subtracting the background but not removing the instrumental response. Thanks to the high photon collecting area of *XMM-Newton* (section 3.2.2), high quality spectra were obtained in the $0.3-10$ keV band. When simultaneous *NuSTAR* data are available, the higher end of the energy band extends further up to $15-20$ keV, as in the bottom two spectra in figure 5.2.

As seen in figure 5.2, the spectra of IC 342 X-1 are featureless except for instrumental ones, including a stepwise decrease from 2.0 to 2.3 keV due to M-edge of the mirror coating materials. The spectral drop below ~ 1.2 keV is due to photoelectric absorption by instrumental materials, as well as by the Galactic interstellar medium toward the object and that within IC 342. As described in section 4.2.1, the spectra are absorbed more strongly than the other ULXs, due to the low Galactic latitude of IC 342. This makes some of the EPIC MOS spectra unavailable below 1 keV.

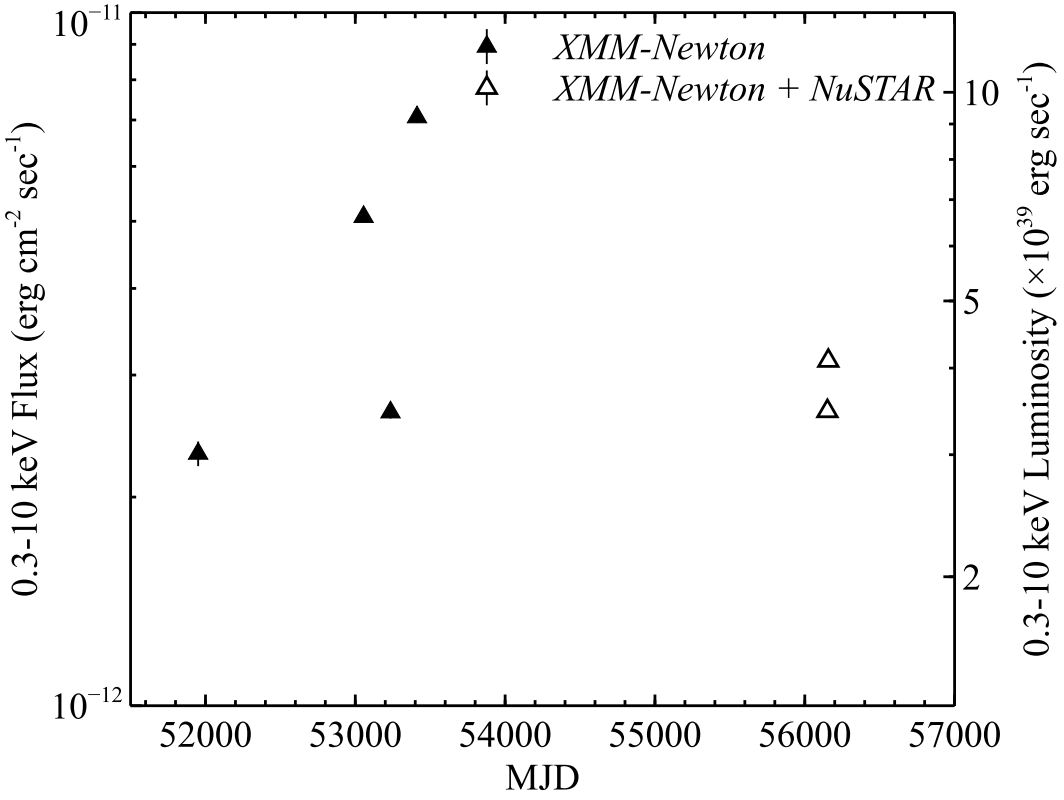

Figure 5.1. Long term variability of IC 342 X-1. The luminosity is calculated by assuming an isotropic emission at the distance of IC 342, 3.3 Mpc.

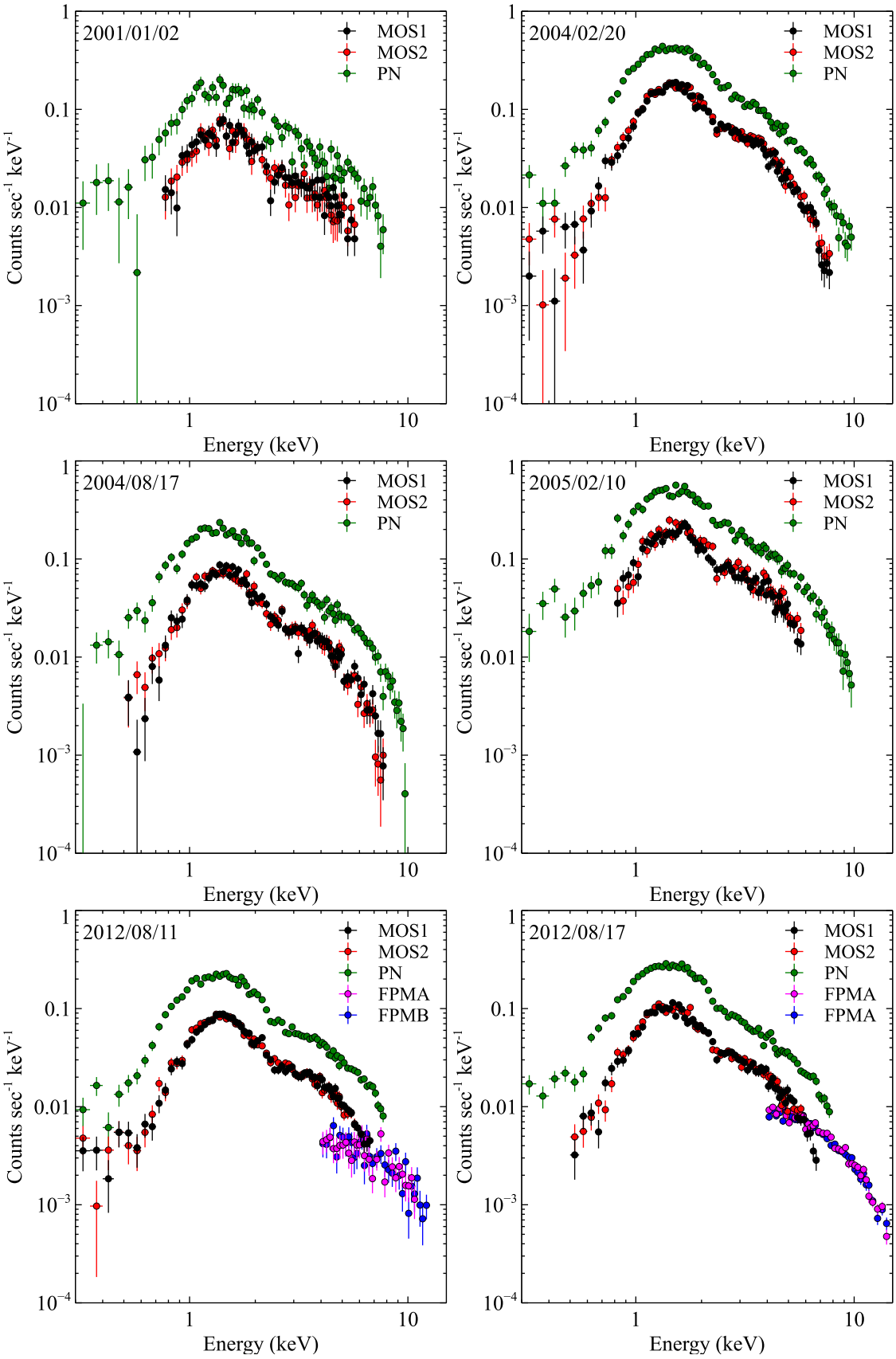

Figure 5.2. Broad-band spectra of IC342 X-1 obtained in the individual observations. Background was subtracted, but the instrumental response is still inclusive.

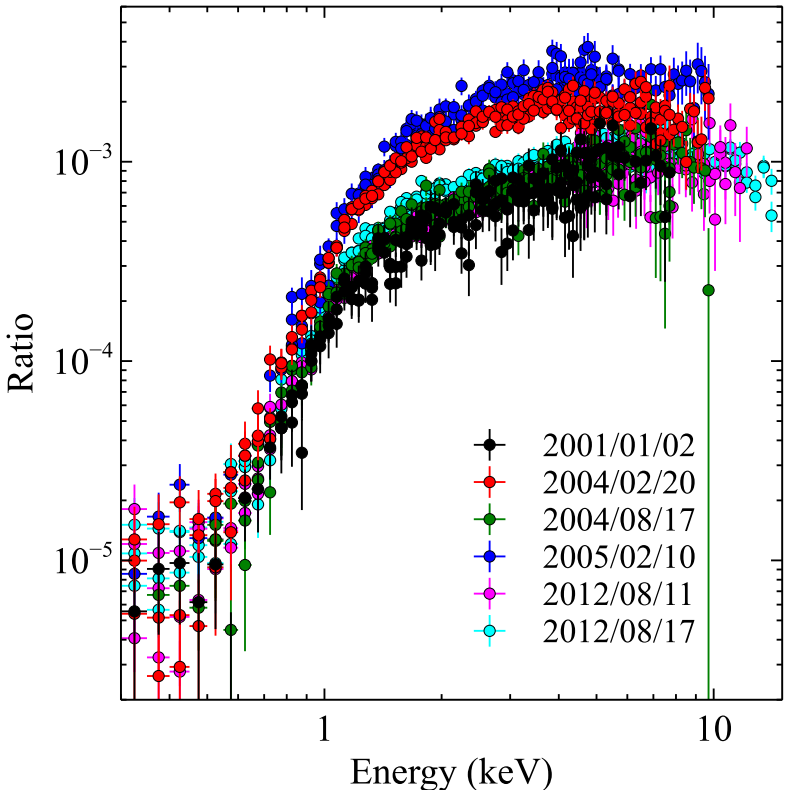

Figure 5.3. Ratios between the X-ray spectra of IC 342 X-1 and a response-folded PL model with $\Gamma = 2$.

5.1.3 Changes of spectral shapes

Since the spectra shown in the previous section are instrumental response inclusive, neither the actual spectral shape nor the source intensity can be easily recognized. In order to approximately deconvolve the spectra from the instrumental response, we took the ratio between the actual X-ray spectra, and a power-law (PL) model with a photon index of $\Gamma = 2$ that is convolved with the instrumental response (PL ratio). The results are shown in figure 5.3. As expected from the precious knowledge, the brighter 2 spectra exhibit a convex shape over $2 - 10$ keV, whereas the fainter 4 have rather PL-like shapes therein. Thus, IC 342 X-1 did make the spectral transitions between the PL state and the Disk-like state several times in a decade. As the source made a transition from the PL state to the Disk-like state, the continuum above 1keV became more convex and the cutoff at 7 keV became lower at the same time. Although the spectra above 2 keV showed such significant changes in shape, the continuum below 1 keV are relatively stable.

To better grasp the characteristics of the spectral variability, we took ratios of each spectrum to that of 2012/08/17, and show the obtained spectral ratios in figure 5.4. The ratios show a common break at ~ 1 keV, suggesting that the X-ray spectra can be decomposed into two major components. One is the component at > 1 keV, which extends up to 10 keV, and becomes more convex as the source gets more luminous. Such a PL continuum with a roll over is often observed as a consequence of thermal Comptonization (THC) process. The other component is the one at < 1 keV. Its stable nature is suggestive of optically-thick source from, e.g., an accretion disk, supplying seed photons to the Compton cloud.

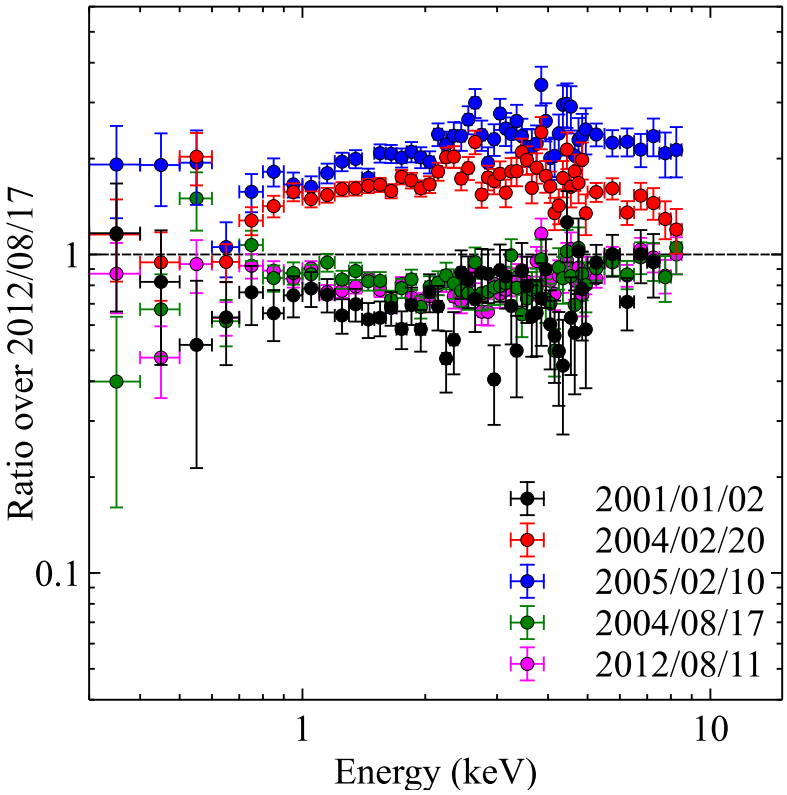

Figure 5.4. EPIC PN spectral ratios for IC 342 X-1. Each spectrum is divided by that of 2012/08/17

5.1.4 Spectral modeling

In order to quantitatively examine the inference made in section 5.1.3, we attempted to fit each broad-band spectrum with a combination of the MCD model and its THC (MCD+THC modeling; Makishima et al. 2008). As described in section 2.1.3, the MCD model approximates the emission from a standard accretion disk, which is expressed as a summation of multiple black body radiations from various disk annuli. Figure 5.5 is a schematic drawing of a geometry we assume here. The accretion disk is covered by a coronal electron cloud, in which some fraction of the seed photons from the disk beneath it are Comptonized (namely THC(MCD)) while the rest reach the observer directly un-scattered (direct MCD).

We carried out the spectral fitting with an analysis software tool called XSPEC (section 4.3.2), which is included in the software library HEASoft. The XSPEC supports various physical models including those for the MCD and THC process. In the present thesis, we combined the `diskbb` model (Mitsuda et al. 1984, Makishima et al. 1986) and the `nthcomp` model (Zdziarski et al. 1996; Zycki et al. 1999) in XSPEC, to realize the MCD+THC modeling described above. The former, `diskbb` represents the direct MCD emission with two free parameters, the inner-disk temperature $T_{\rm in}$, and the normalization which is proportional to the square of the apparent inner-disk radius $R_{\rm raw}$. Thus parameters are determined mainly by the spectral peak energy and the flux of the black body component of the direct MCD emission, respectively. The `nthcomp` model accounts for the THC(MCD) emission in terms of three free parameters; the coronal electron temperature $T_{\rm e}$, spectral photon index Γ, and the seed photon temperature. The former two are determined by the spectral cutoff energy and the spectral slope of the THC continuum, respectively. Since we

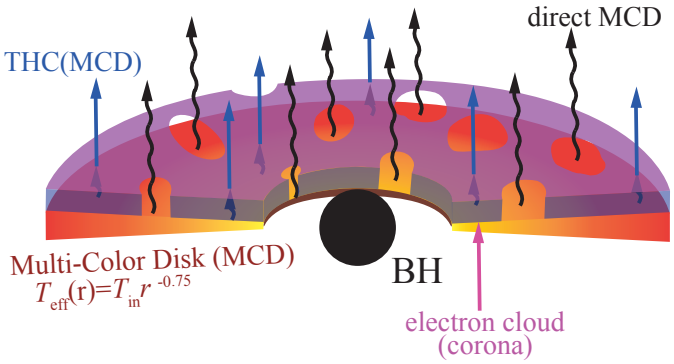

Figure 5.5. Schematic drawing of the geometry assumed in the MCD+THC modeling.

assume that the seed photons are supplied by the disk beneath the corona (Makishima et al. 2008; Gladstone et al. 2009; Miyawaki et al. 2009), we set the seed photon temperature to be identical to $T_{\rm in}$.

To express the absorption by the interstellar medium, we employed the photoelectric absorption model `tbabs` (Wilms, Allen and McCray 2000), which gives a column density $N_{\rm H}$ of equivalent hydrogen. Since the total absorption can be decomposed into the Galactic line-of-sight contribution and those associated with the host galaxy IC 342, we multiplied two `tbabs` factors to the MCD+THC continuum, and fixed $N_{\rm H}$ of one of them to the Galactic value shown in table 4.1. This enable us to evaluate the intrinsic absorption separately from the Galactic one.

5.1.5 Model fitting to the spectra

The result of the spectral model fitting is summarized in table 5.1, where 2004/02/20 and 2005/02/10 correspond to the Disk-like state. The actual spectra and their residuals from the model are shown in figure 5.6. Thus, the MCD+THC model has successfully reproduced all the spectra, in spite of the large variation in their shape. Thanks to the high quality data, the model parameters were mostly well constrained.

In all spectra, the Compton electron temperature was determined as $T_{\rm e} \sim 2-3$ keV, by identifying $3T_{\rm e}$ with the continuum cutoff observed at ~ 7 keV. As described in Sunyaev and Titarchuk (1980), the Compton continuum slope (photon index) Γ in the `nthcomp` model is expressed as

$$\Gamma = -\frac{1}{2} + \sqrt{\frac{9}{4} + \frac{4}{y}} \ , \tag{5.1}$$

where

$$y \equiv \left(\frac{4kT_{\rm e}}{m_{\rm e}c^2} \right) \tau \left(1 + \tau/3\right) \tag{5.2}$$

is the Compton y-parameter, with τ being the Compton optical depth. For example, we obtain $\Gamma = 3.0$, 2.0, and 1.5 for $y = 0.4$, 1.0, and 2.3, respectively. Since the fit gave typically $\Gamma = 1.5-2.0$, we obtain $y \sim 1-2.3$, which is very reasonable. Further employing equation 5.2 and the measured values of $T_{\rm e}$, the Compton optical depth is obtained as $\tau \sim 10-15$. More detailed values of the derived τ are given in table 5.1.

Let us next examine the derived MCD parameters, $T_{\rm in}$ and $R_{\rm raw}$. In the PL state, these parameters are determined mainly by identifying the slight soft X-ray hump below $\sim$ 1 keV with the directly visible disk emission. In the Disk-like state, $R_{\rm raw}$ becomes very poorly determined because such a soft excess is no longer visible in the spectrum. Nevertheless, $T_{\rm in}$ can sill be constrained, by the low-energy end of the convex continuum where the Rayleigh-Jeans regime of the seed photon spectrum is visible. As reported by Kobayashi et al. (2016), the Disk-like state spectra gave generally higher values of $T_{\rm in}$ than the PL state ones.

Since we assumed that some fraction of the disk photons are boosted by the coronal electrons to form the Comptonized continuum, $R_{\rm raw}$ represents only the linear size of the directly visible disk. Then, including these seed photons as well, the true inner radius of the disk beneath the corona must be calculated as

$$R_{\rm tot}^2 = R_{\rm raw}^2 + R_{\rm thc}^2 \, , \tag{5.3}$$

(e.g., Kubota 2001, Kubota and Makishima 2004, Makishima et al. 2008) where $R_{\rm thc}$ is the linear size of the covered fraction of the disk (i.e., the seed-photon source). Since $T_{\rm in}$ is constrained by the fitting, we can transform the `nthcomp` normalization into $R_{\rm thc}^2$, assuming that the photon number is conserved in Comptonization. The values of $R_{\rm tot}^2$ calculated in this way are shown in table 5.1.

As we look through the obtained parameters, it is noticeable that the Disk-like state spectra (2005/02/10) show higher $T_{\rm in}$ than those in the PL state, and exhibit poorly constrained $R_{\rm raw}$, just as expected in the arguments above and Kobayashi et al. (2016). However, the data from 2004/02/20 shows extreme large $R_{\rm tot}$ of $\sim$ 19000 km, and low $T_{\rm in} = 0.15$, which is rather similar to those in the PL state, in spite of its nearly identical spectral shape to that of 2005/02/10. We considered that this is instrumental, since only this data required large absorption column density of 7×10^{21} cm^{-2}, which is unnaturally higher than those obtained in other observations while the spectral ratio do not indicate any large increase in $N_{\rm H}$. Furthermore, allowing such a cool and huge disk to exist outside the detectable energy band is unreasonable. Hence, we fixed $N_{\rm H}$ to the average value 2.5×10^{21} cm^{-2} obtained from the other observations, and refitted the spectrum. The result is shown below the row for the first attempt in table 5.1. Although the chi squared became slightly worse, we hence adopt this fitting result for 2005/02/10. The fit gave reasonably higher $T_{\rm in}$, and smaller $R_{\rm tot}$, which are similar to those in 2005/02/10.

Table 5.1: Parameters obtained from the spectral fitting to the spectrum of IC 342 X-1.

Date[a] YY/MM/DD	N_H[b]	T_e (keV)	Γ	τ[c]	T_{in} (keV)	R_{raw}[d]	R_{tot}[e]	L_{disk}[f]	L_X[g]	χ^2/ν (ν)
				XMM-Newton						
01/01/02	$1.9^{+0.3}_{-0.7}$	$1.7^{+1.7}_{-0.3}$	< 1.68	> 18	$0.6^{+0.2}_{-0.4}$	$0.3^{+3.6}_{-0.1}$	0.28	1.3	3.1	0.89 (189)
04/02/20	$7.3^{+1.3}_{-1.5}$	$2.8^{+2.2}_{-0.6}$	$2.02^{+0.1}_{-0.09}$	10	0.15 ± 0.02	$17.9^{17.0}_{-10.4}$	19.1	23.8	7.1	1.12 (237)
	2.5 (fixed)	$2.4^{+1.1}_{-0.5}$	$1.9^{+0.1}_{-0.2}$	12	0.5 ± 0.1	< 0.3	0.3	0.7	3.1	1.27 (228)
04/08/17	$3.4^{+1.3}_{-0.9}$	$2.5^{+1.5}_{-0.6}$	$1.7^{+0.1}_{-0.2}$	14	$0.32^{+0.1}_{-0.09}$	$0.9^{+1.1}_{-0.5}$	1.1	1.6	3.4	1.15 (229)
05/02/10	$2.3^{+0.8}_{-0.5}$	$3.3^{+3.4}_{-1.5}$	< 2.1	> 9	$0.6^{+0.3}_{-0.1}$	< 0.4	0.38	2.4	9.5	0.93 (197)
				XMM-Newton+NuSTAR						
12/08/11	4.2 ± 0.8	$3.2^{+1.3}_{-0.6}$	$1.70^{+0.05}_{-0.06}$	12	$0.24^{+0.04}_{-0.03}$	$2.0^{+1.6}_{-0.9}$	2.4	2.5	3.54	0.92 (275)
12/08/17	4.1 ± 1.0	3.0 ± 0.2	1.84 ± 0.05	11	$0.22^{+0.07}_{-0.03}$	$2.2^{+2.6}_{-1.4}$	2.9	2.54	4.0	1.07 (291)

a: Date of the observation.

b: Intrinsic column density of equivalent Hydrogen in units of 10^{21} cm^{-2}.

c: Optical depth of the coronal electron cloud.

d: Apparent inner-disk radius of the un-scattered accretion disk component in units of 1000 km.

e: Inner-disk radius of the overall disk component in units of 1000 km. Calculated from equation 5.3

f: Bolometric luminosity of the accretion disk component in units of 10^{39} erg sec^{-1}.

g: Absorbed $0.3 - 10$ keV band luminosity in units of 10^{39} erg sec^{-1}.

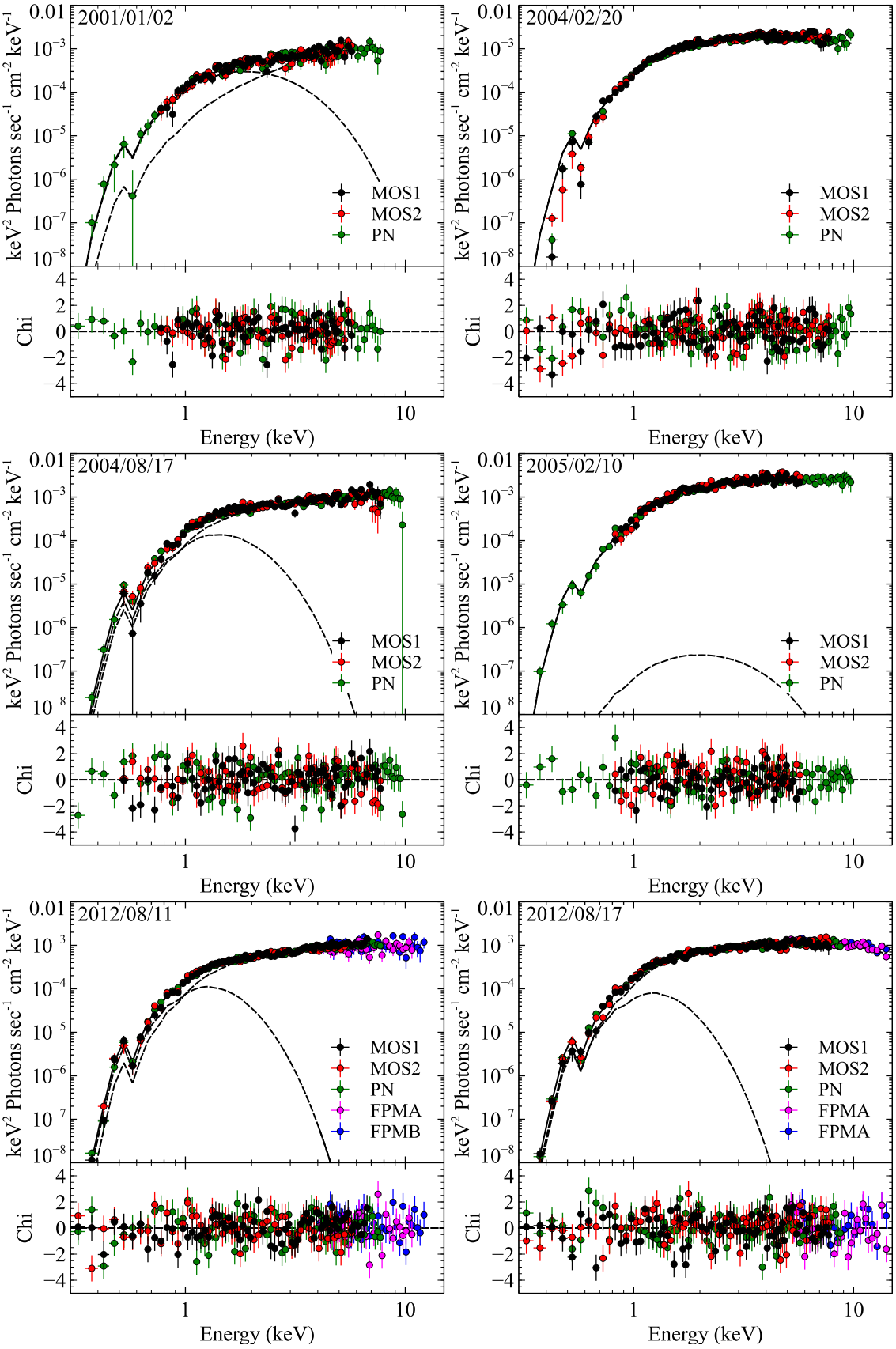

Figure 5.6. Spectra of IC 342 X-1 fitted and deconvolved with the MCD+THC model (top panels) and their residuals (bottom panels). The contributions of the MCD and THC components are drawn with the spectra in dashed lines.

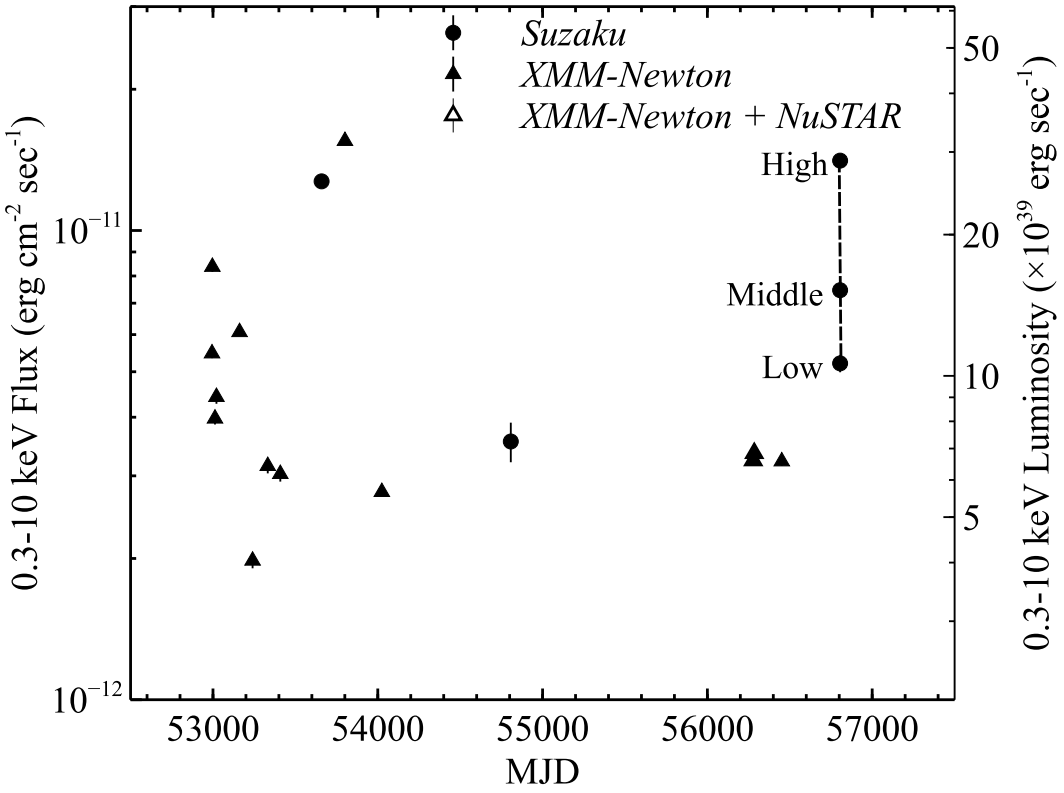

Figure 5.7. Long term variability of NGC 1313 X-1.

5.2 NGC 1313 X-1

The spiral galaxy NGC 1313, at a distance of 4.13 Mpc, host two typical ULXs, X-1 and X-2. In the present thesis, we study X-1 which was observed 18 times altogether with *Suzaku*, *XMM-Newton*, and *NuSTAR*; see section 4.1.2.

5.2.1 Intensity variations

Figure 5.7 shows long term variability of the $0.3 - 10$ keV flux of NGC 1313 X-1, where the data points represent the averaged flux in individual observations. The luminosity is calculated by assuming an isotropic emission at the distance of NGC 1313, 4.13 Mpc. One of the unique characteristics of this source is its high variability in luminosity. In fact, as shown in figure 5.7, it showed clear brightening in 2005, 2006, and in 2014, when the luminosity reached $> 2 \times 10^{40}$ erg sec^{-1}. At the dimmest, on the other hand, the luminosity decreased down to 4×10^{39} erg sec^{-1}. The variation thus amounts to almost an order of magnitude, around a mean of $(6 - 7) \times 10^{39}$ erg sec^{-1} (section 4.2.2).

Figure 5.8 shows two $0.5 - 10$ keV background subtracted light curves of NGC 1313 X-1, obtained in different observations with the *Suzaku* XIS. The light curve in the left panel (2008/12/05), which corresponds to the data point on MJD 54800 in figure 5.7, does not show noticeable variations beyond 20%. (The low data points at $6 - 8 \times 10^5$ sec are due to the Earth occultations or the SAA passages; section 4.3.2). When it became most luminous (figure5.8 right; MJD 56800 in figure 5.7), NGC 1313 X-1 in contrast showed strong variability on a few tens ks time scale (Mizuno et

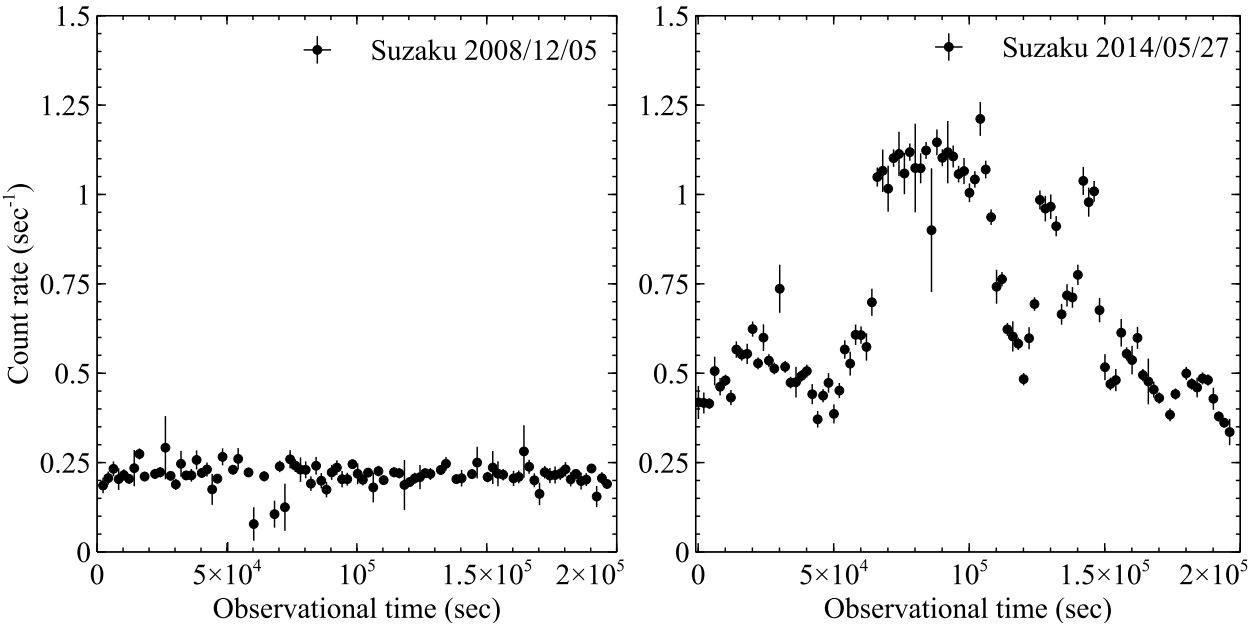

Figure 5.8. Two of light curves of NGC 1313 X-1 obtained with *Suzaku*.

al. 2007). Therefore, we divide this particular data set in three intensity intervals, low (< 0.65 counts sec^{-1}), middle ($0.65 - 0.85$ counts sec^{-1}), and high (> 0.85 counts sec^{-1}), and extracted spectra from each of them.

5.2.2 Broad band X-ray spectra and their variations

As the luminosity changed, the spectral shape of NGC 1313 X-1 varied significantly over the 13 years of observational history. To grasp the behavior, we again took the ratios between the actual X-ray spectra and a PL model with $\Gamma = 2$, and show the results in figure 5.9. Since we deal with 18 spectra altogether, we split them into four groups according to the 0.3-10 keV intensity.

As seen in figure 5.9, the spectral change is prominent mainly at energies of > 1 keV, like in IC 342 X-1. Furthermore, the spectral shape appears to be mainly determined by the luminosity. Some spectra (generally most luminous ones) exhibit characteristics of the Disk-like state, and those typical of the PL state are also seen particularly when the source is dim. Furthermore, we notice several features that was not seen in IC 342 X-1. One is the spectrum observed on 2004/08/23, which has an extremely soft PL continuum approximated by a PL with $\Gamma > 2.3$; this makes a contrast to the other spectra which exhibit significantly harder continuum with $\Gamma < 2$. Since this spectrum emerged when the source was dimmest among our sample, it may suggest a presence of an additional spectral state for ULXs at the lowest luminosity. The other is that some of the spectra, mainly observed at intermediate luminosities, exhibit characteristics which are in between those of the two spectral states; in $1 - 5$ keV, these spectra are convex like in the Disk-like state, but they look very similar to the PL-state spectra in energies of > 5 keV. Since its spectral shape and luminosity are roughly in between those of the PL state and the Disk-like state, these may be an important clue to continuously connecting the two typical spectral shapes.

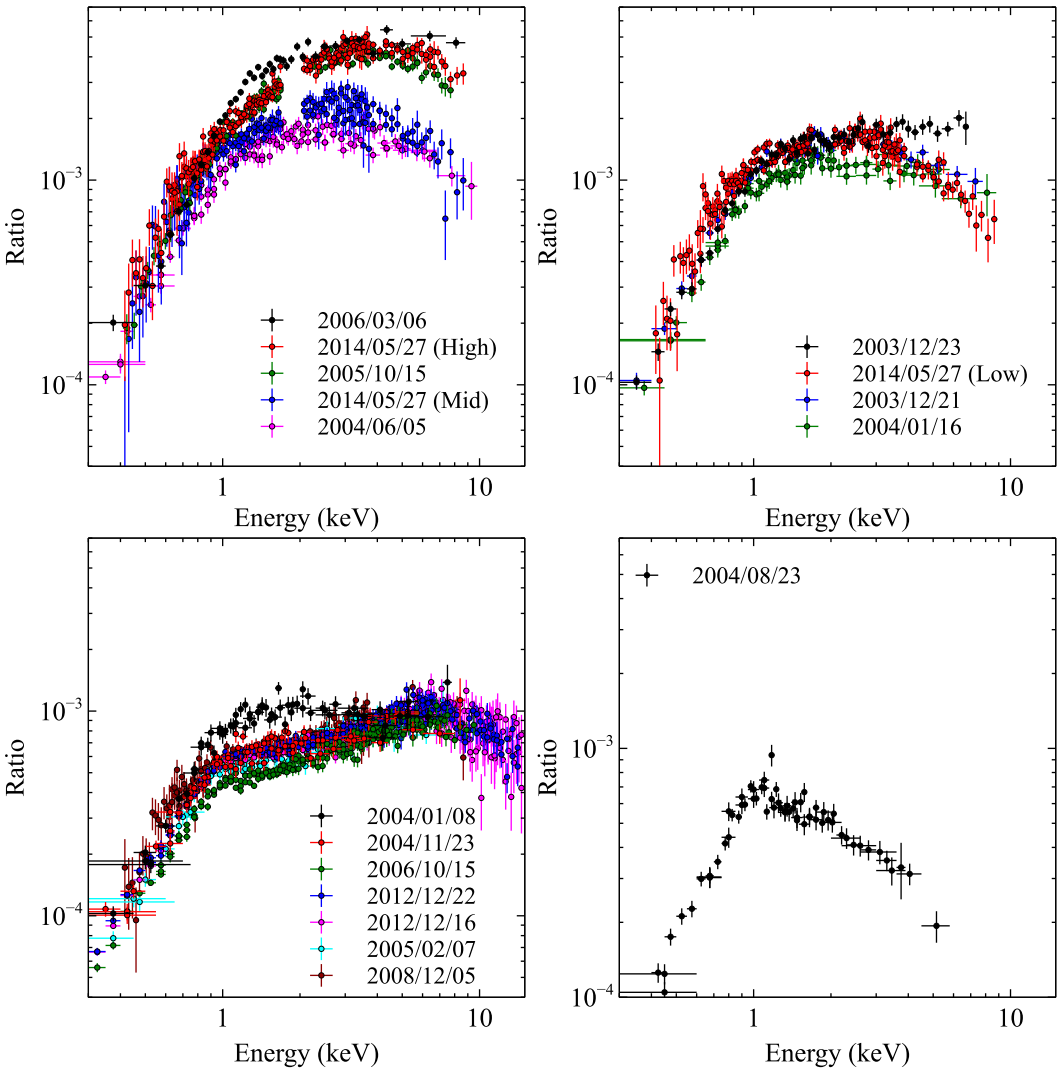

Figure 5.9. Ratios between the X-ray spectra of NGC 1313 X-1, and a response-folded PL model with $\Gamma = 2$. They are grouped into four in terms of their $0.3 - 10$ keV luminosity. Top left: $L_X > 1.3 \times 10^{40}$ erg sec^{-1}. Top right: 8×10^{39} erg sec^{-1} $< L_X < 1.3 \times 10^{40}$ erg sec^{-1}. Bottom left: 5×10^{39} erg sec^{-1} $< L_X < 8 \times 10^{39}$ erg sec^{-1}. Bottom right: $L_X < 5 \times 10^{39}$ erg sec^{-1}.

5.2.3 Model fitting to the spectra

As we have looked through, NGC 1313 X-1 has large diversity in its spectral shape, which makes the source highly worth studying. In order to see whether the MCD+THC modeling is still valid under its strong variability, we similarly performed a spectral fitting as in IC 342 X-1. Although the fundamental modeling is identical to that in IC 342 X-1, we gave an extra treatment to the modeling of the low-energy photoelectric absorption. According to an analysis utilizing the *Suzaku* data acquired on 2005 October 15, NGC 1313 X-1 is possibly associated with an oxygen-poor environment (Mizuno et al. 2007). Therefore, to express the intrinsic absorption inside the NGC 1313 galaxy, we replaced the `tbabs` model with `vphabs` model, which allows us to change the abundances of individual elements as free parameters. Following Mizuno et al. (2007), we fixed the oxygen abundance to $0.68 Z_{\odot}$ throughout the analysis of NGC 1313 X-1, while those of the other elements are fixed at $1 Z_{\odot}$, where $Z_{\odot}$ represents the solar abundance.

The result of the model fitting is summarized in table 5.2. The actual fitted spectra and their residuals from the model are shown in figure 5.10. In the *Suzaku* data analysis, we excluded the $1.7 - 2.0$ keV range to avoid calibration uncertainties with the Si-Kα edge, and co-added data from the FI-XIS cameras (section 3.1.3) because their instrumental responses are nearly identical. Like in IC 342 X-1, the MCD+THC successfully reproduced all spectra of NGC 1313 X-1. The derived disk temperature are distributed around $T_{\rm in} = 0.2 - 0.3$ keV, and the data require cool ($T_{\rm e} < 3$ keV) and thick ($\tau > 10$) coronae, which are also similar to what we obtained in IC 342 X-1. While the spectral slope was rather hard ($\Gamma < 2.0$) in IC 342 X-1, those of NGC 1313 X-1 scatter more widely over $1.7 \leq \Gamma \leq 2.3$, just reflecting the spectral diversity.

According to the results in table 5.2, NGC 1313 X-1 exhibited low ($T_{\rm in} < 0.15$) and extremely large ($R_{\rm raw} > 10000$ km) disks in the Disk-like state (e.g., 2014/05/27 High, Mid, and Low), which is similar to what happened in IC 342 X-1. Unlike the case in IC 342 X-1, $N_{\rm H}$ in these fits has no large difference from the results in the other data sets, but, it is still unphysical to allow such large accretion disks of which the emitted photons mostly fall below the detectable energy range (< 0.5 keV). We consider that such a result was obtained because the data sets are actually requiring some extra soft component in $0.3 - 0.8$ keV, and those are multi-color black body emissions from the outer side of the disks, where the corona is no longer present and the raw MCD is visible. In order to take this case into account, we modified our modeling for only the high luminosity spectra exhibiting unnaturally large inner-disk radius, by adding extra `diskbb` model which represents the MCD emission from uncovered outer disk, and we made the corona to cover only the inner part (hotter part) of the disk. The fitting results utilizing this modified model are summarized in table 5.2 as additional results in respective data. In the previous modeling, a single MCD component was required to supply the seed photons to the THC continuum, and to explain the soft excess. Now, these two requirements are carried respectively by two disks, the inner hotter one and the other cooler one.

Thus, the alternative model gave similarly good fit to the Disk-like spectra, and the inner-disk temperature of the hotter disk became higher $0.6 - 0.9$ keV, which is consistent with the view described in section 5.1.5. Furthermore, the relation between the physical parameters of the outer-disk ($R_{\rm raw1}$ and $T_{\rm in1}$) and those of the inner-disk ($R_{\rm tot2}$ and $T_{\rm in2}$) are satisfying the condition expected in the standard accretion disk $T_{\rm eff}(r) \propto T_{\rm in}(r/r_{\rm in})^{-3/4}$ (equation 2.4). In other words, the two MCD components are considered to represent a single MCD emission, of which the inner part

is fully covered by the corona whereas the other part is directly visible.

Combining the results altogether, apart from the point that the emission from the outer disk is visible in the observing energy band, the convex spectra in NGC 1313 X-1 still follow the common characteristics expected in the Disk-like state. They exhibited hotter inner-radius temperature than those in the PL state ($T_{\rm in} \sim 0.2$ keV), with disk corona nearly fully covering the inner part of the disk.

Figure 5.11 shows the correlation between the luminosity and the Galactic subtracted $N_{\rm H}$ (the value obtained from the `vphabs` model). The obtained values are distribute around $N_{\rm H} = 3 \times 10^{21}$ cm^{-2}, while the luminosity changed by an order of magnitude. Considering errors, the change in $N_{\rm H}$ gives a reduced chi-squared of 1.70 (for $\nu = 17$). Therefore we cannot claim that $N_{\rm H}$ was constant, but its variation is small; the error-weighted mean and the standard deviation become $< N_{\rm H} >= (2.1 \pm 0.9) \times 10^{21}$ cm^{-2}.

Table 5.2: Parameters obtained from the spectral fitting to the spectrum of NGC 1313 X-1.

Date[a] YY/MM/DD	N_H[b]	T_e (keV)	Γ	τ[c]	T_{in} or T_{in1}[d] (keV)	R_{raw}[e] or R_{raw1}[f]	T_{in2}[g] (keV)	R_{tot}[h] or R_{tot2}[i]	L_{disk}[j]	L_X[k]	χ^2/ν (ν)
					XMM-Newton						
03/12/21	$3.2^{+1.3}_{-0.9}$	$1.8^{+1.6}_{-0.4}$	2.1 ± 0.2	12	$0.18^{+0.08}_{-0.04}$	$7.4^{+18.0}_{-5.2}$	–	9.4	12.0	10.8	0.82 (72)
03/12/23	$2.7^{+0.7}_{-0.6}$	> 1.9	$1.96^{+0.08}_{-0.06}$	> 11	$0.22^{+0.07}_{-0.05}$	$3.3^{+4.3}_{-1.8}$	–	4.6	6.4	13.8	0.93 (67)
04/01/08	3 ± 1	> 2.6	$2.31^{+0.09}_{-0.34}$	> 8	$0.18^{+0.08}_{-0.03}$	7.0^{+11}_{-5}	–	8.7	10.2	7.5	0.94 (207)
04/01/16	$2.8^{+1.0}_{-0.7}$	$2.6^{+2.6}_{-1.1}$	$2.2^{+0.2}_{-0.3}$	9.3	$0.21^{+0.12}_{-0.06}$	$3.1^{+9.0}_{-1.9}$	–	4.7	5.5	8.4	1.12 (212)
04/06/05	$2.6^{+0.8}_{-0.6}$	$2.0^{+0.7}_{-0.4}$	2.1 ± 0.1	11	$0.19^{+0.12}_{-0.04}$	< 8.6	–	5.6	5.3	11.4	1.05 (227)
04/08/23	$2.8^{+0.6}_{-0.5}$	$0.9^{+0.6}_{-0.2}$	$2.0^{+0.5}_{-0.8}$	19	$0.22^{+0.05}_{-0.04}$	$4.0^{+3.2}_{-1.5}$	–	4.4	5.9	3.3	1.16 (167)
04/11/23	$1.7^{+0.5}_{-0.4}$	$2.0^{+8.2}_{-0.6}$	$1.7^{+0.2}_{-0.3}$	16	$0.29^{+0.08}_{-0.06}$	$1.4^{+0.8}_{-0.5}$	–	1.8	3.0	6.4	1.26 (212)
06/03/06	$3.2^{+0.8}_{-0.7}$	$1.5^{+0.2}_{-0.1}$	1.92 ± 0.09	15	$0.17^{+0.04}_{-0.03}$	$12.0^{+14.0}_{-7.0}$	–	15.0	24.3	31.8	1.41 (77)
	$2.7^{+0.4}_{-0.4}$	> 1.0	$3.0^{+0.5}_{-0.9}$	$11 >$	0.23 ± 0.03	$5.7^{+7.7}_{-4.5}$	$0.8^{+0.1}_{0.2}$	0.7	26	31.8	1.26 (71)
06/10/15	$2.4^{+0.3}_{-0.2}$	$2.6^{+0.3}_{-0.2}$	1.70 ± 0.03	14	0.20 ± 0.01	$3.5^{+3.8}_{-0.8}$	–	3.6	2.7	6.6	1.28 (227)
13/06/08	$2.2^{+0.8}_{-0.6}$	120^{+120}_{-50}	$1.83^{+0.08}_{-0.04}$	> 13	$0.21^{+0.06}_{-0.04}$	$2.8^{+3.8}_{-1.5}$	–	3.6	3.3	6.6	1.05 (82)
					Suzaku						
05/10/15	$2.9^{+0.8}_{-0.9}$	1.6 ± 0.1	1.75 ± 0.05	17	$0.17^{+0.05}_{-0.02}$	$7.2^{+8.4}_{-5.4}$	–	9.9	10.6	24.7	1.35 (127)
	2.6 ± 0.5	> 2.7	$2.7^{+0.2}_{-0.6}$	> 7	0.22 ± 0.02	$4.5^{+5.4}_{-2.5}$	$0.9^{+0.1}_{-0.2}$	0.3	8	24.7	1.23 (135)
08/12/05	$1.7^{+0.6}_{-0.5}$	$2.3^{+0.5}_{-0.3}$	$1.7^{+0.05}_{-0.06}$	15	$0.22^{+0.04}_{-0.03}$	$2.7^{+1.8}_{-1.1}$	–	3.3	3.3	7.1	1.15 (189)
14/05/27 (Low)	4.4 ± 0.9	$1.6^{+0.3}_{-0.2}$	2.19 ± 0.1	13	$0.13^{+0.02}_{-0.01}$	28.1^{+21}_{-14}	–	30.3	33.8	10.6	1.35 (187)
	3.3 ± 0.1	> 2.5	$3.1^{+0.2}_{-0.6}$	> 6.2	$0.17^{+0.02}_{-0.01}$	$10.0^{+13.3}_{-7.9}$	$0.62^{+0.06}_{-0.12}$	0.5	4.8	10.6	1.35 (192)
14/05/27 (Mid)	4.6 ± 1.4	$1.6^{+0.3}_{-0.2}$	2.1 ± 0.1	14	$0.13^{+0.02}_{-0.01}$	$35.0^{+41.1}_{-22.9}$	–	37.3	51.3	15.0	1.04 (189)
	3.0 ± 0.1	> 2.5	$2.7^{+0.6}_{-0.5}$	> 5	$0.17^{+0.05}_{-0.02}$	$10.9^{+22}_{-9.8}$	$0.7^{+0.1}_{-0.2}$	0.5	7.7	15.0	0.99 (189)
14/05/27 (High)	$4.5^{+0.9}_{-1.0}$	$1.8^{+0.2}_{-0.1}$	1.81 ± 0.06	15	0.13 ± 0.01	$39.3^{+25.5}_{-18.2}$	–	41.5	63.5	28.4	1.08 (193)
	2.3 ± 0.1	$2.3^{+1.3}_{-0.3}$	$2.0^{+0.3}_{-0.2}$	11	$0.18^{+0.05}_{-0.03}$	$9.0^{+17.8}_{-8.3}$	$0.7^{+0.3}_{-0.2}$	0.6	11.1	28.3	1.01 (197)

Table 5.2: Continued

Date[a] YY/MM/DD	N_H[b]	T_e (keV)	Γ	τ[c]	T_{in} or T_{in1}[d] (keV)	R_{raw}[e] or R_{raw1}[f]	T_{in2}[g] (keV)	R_{tot}[h] or R_{tot2}[i]	L_{disk}[j]	L_X[k]	χ^2/ν (ν)
XMM-Newton+NuSTAR											
12/12/16	2.0 ± 0.2	$2.6^{+0.2}_{-0.1}$	1.73 ± 0.02	13	$0.24^{+0.02}_{-0.01}$	$2.0^{+0.4}_{-0.3}$	–	2.5	2.7	6.6	1.30 (266)
12/12/22	2.0 ± 0.1	2.6 ± 0.1	$1.72^{+0.02}_{-0.03}$	13	0.25 ± 0.01	1.9 ± 0.3	–	2.4	2.9	6.8	1.13 (258)

a: Date of the observations

b: Intrinsic column density of equivalent Hydrogen in units of 10^{21} cm^{-2}.

c: Optical depth of the coronal electron cloud.

d: Inner-disk temperature at the radius where the corona is truncated (see text).

e: Apparent inner-disk radius of the un-scattered accretion disk component in units of 1000 km.

f: Apparent inner-disk radius of the outer-disk region in units of 1000 km.

g: Inner-disk temperature of the model representing the inner part of the disk in the alternative model (see text).

h: Inner-disk radius of the overall disk component in units of 1000 km. Calculated from equation 5.3

i: Inner-disk radius of the overall disk component in units of 1000 km. Calculated from equation 5.3

j: Bolometric luminosity of the accretion disk component in units of 10^{39} erg sec^{-1}.

k: Absorbed $0.3 - 10$ keV band luminosity in units of 10^{39} erg sec^{-1}.

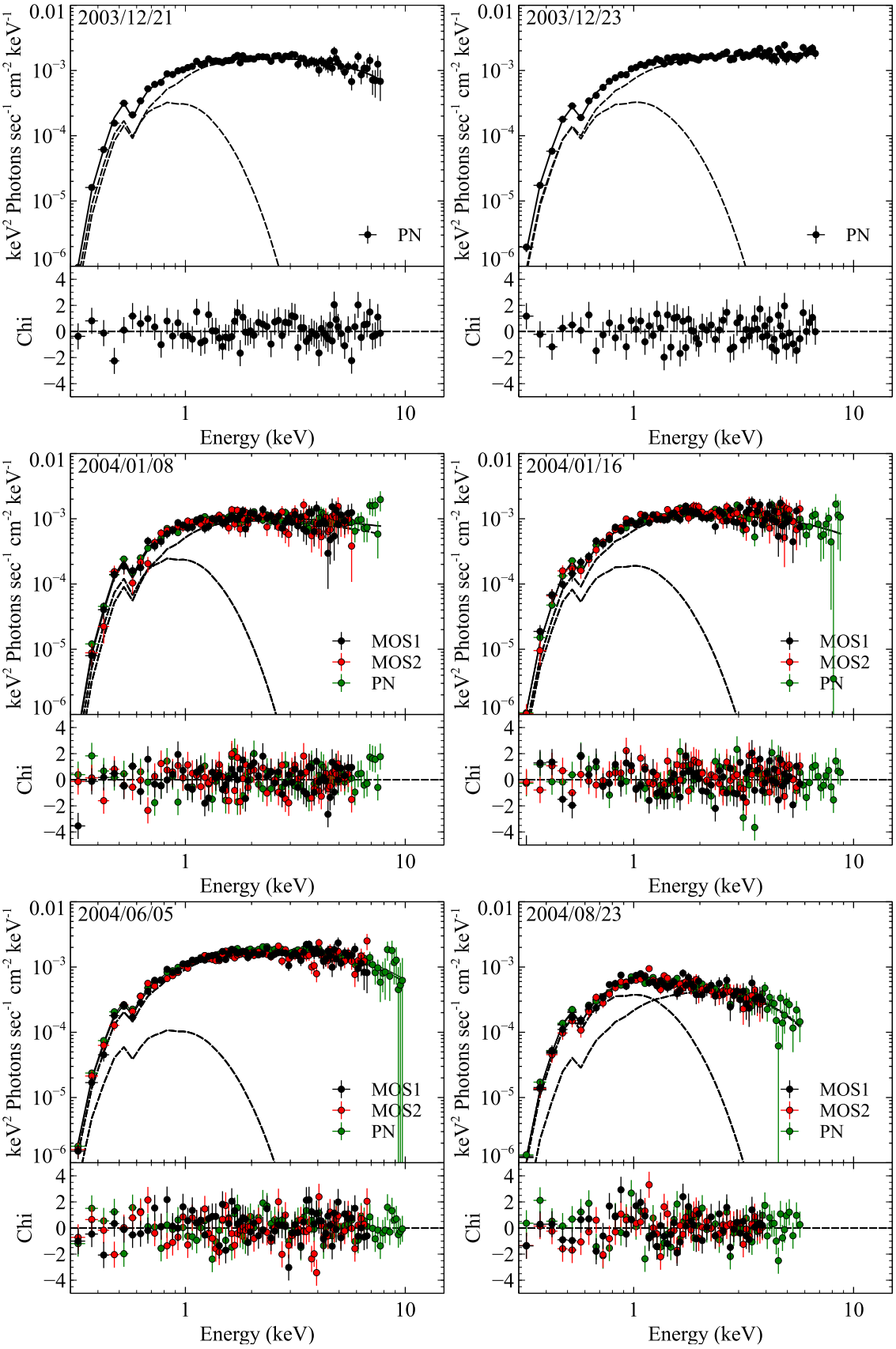

Figure 5.10. Spectra of NGC 1313 X-1 fitted and deconvolved with the MCD+THC model (top) and their residuals (bottom). The contributions of the MCD and THC components are drawn with the spectra in dashed lines.

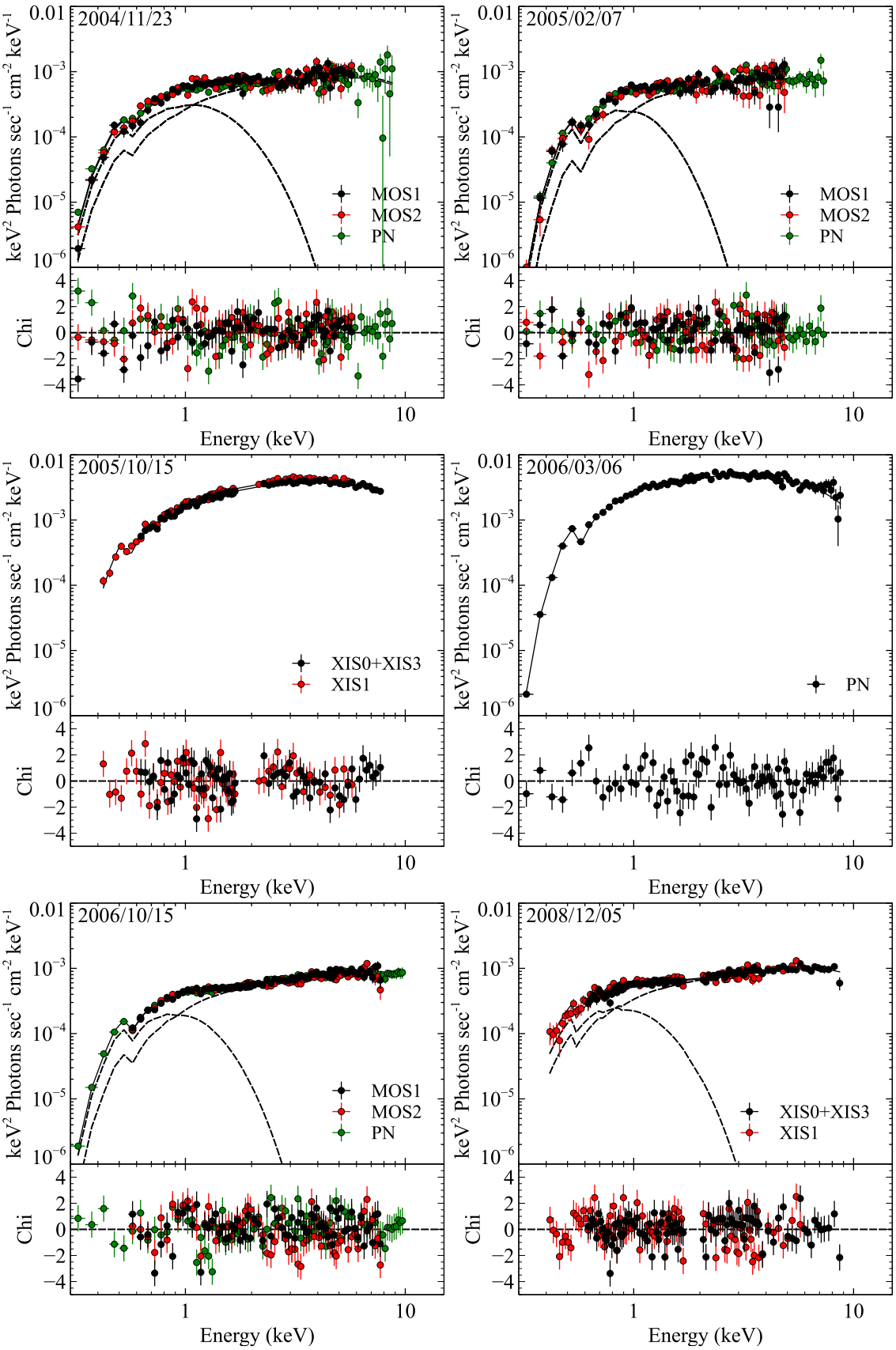

Figure 5.10. Continued.

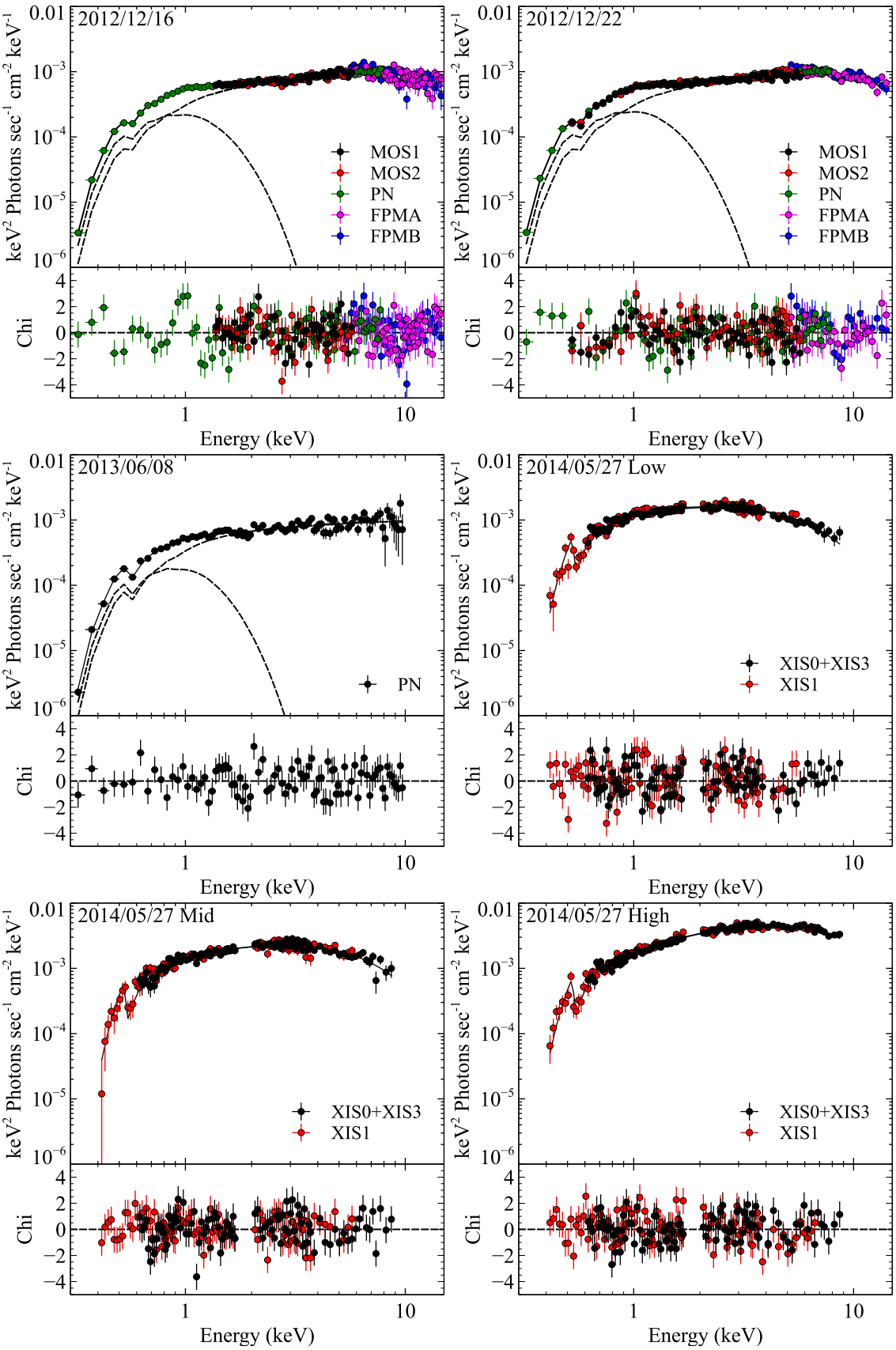

Figure 5.10. Continued.

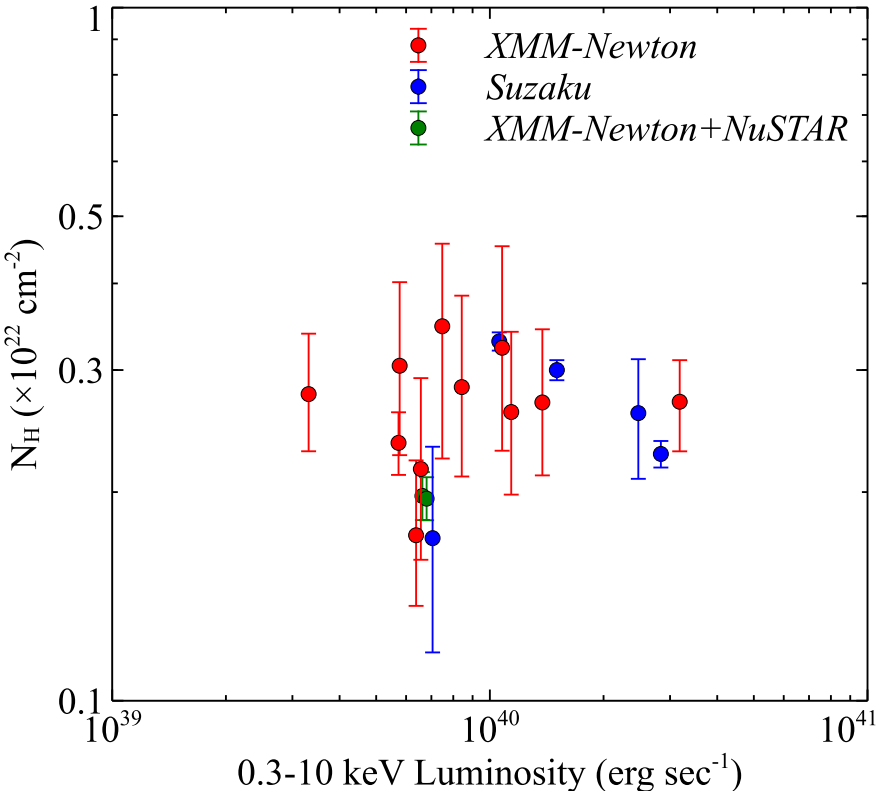

Figure 5.11. A correlation between $0.3 - 10$ keV luminosity and the absorption column density $N_{\rm H}$ in NGC 1313 X-1. The Galactic line-of-sight contribution is removed.

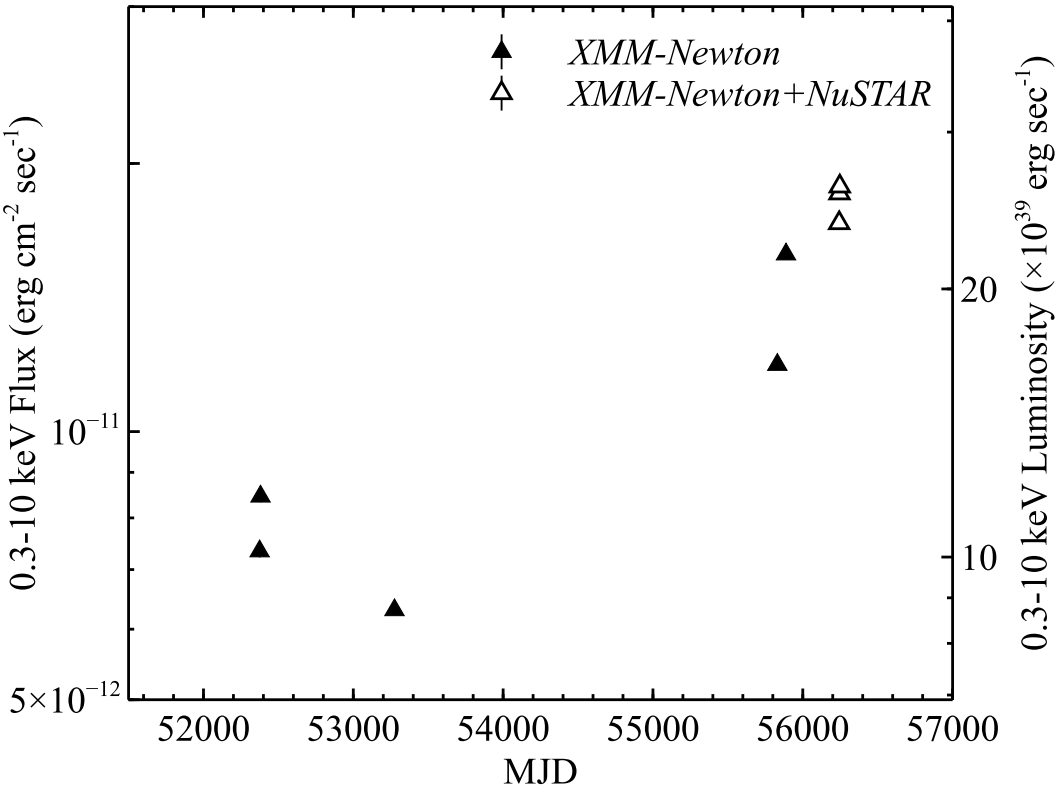

Figure 5.12. Long term variability of Holmberg IX X-1.

5.3 Holmberg IX X-1

5.3.1 Intensity variations

We present long term variability of Holmberg IX X-1 in figure 5.12. The luminosity is calculated by assuming an isotropic emission at the distance of the Holmberg IX galaxy, 3.4 Mpc. As described in section 4.2.3, it is one of the most intensively studied ULXs, and has the second largest number of spectra among the present sample. Its luminosity changed by a factor of three in a decade. During a large campaign conducted with *NuSTAR* in 2012 (MJD $\sim$ 56200), it showed a gradual rise in luminosity, from 1.2×10^{40} erg sec^{-1} to 2.5×10^{40} erg sec^{-1}, in 3 weeks, which was covered by 6 discrete observations.

5.3.2 Broad band spectra and their variations

The PL ratios of the Holmberg IX X-1 spectra are shown in figure 5.13. Like in NGC 1313 X-1, they are split in two groups for presentation. Those with luminosity higher than 1.5×10^{40} erg sec^{-1} are presented in the left panel, and the rest are in the right. As also seen in other ULXs, Holmberg IX X-1 show strong variability above 1 keV, while less variable below $\sim$ 1 keV. Unlike NGC 1313 X-1, its spectral continuum has been always hard ($\Gamma > 2.0$) throughout the observations, which is somewhat similar to the behavior of IC 342 X-1. The soft component which was barely seen in IC 342 X-1 is much clearly present in the spectrum with the lowest luminosity. As the luminosity increased, the soft component became gradually dominated by the hard PL emission, and finally

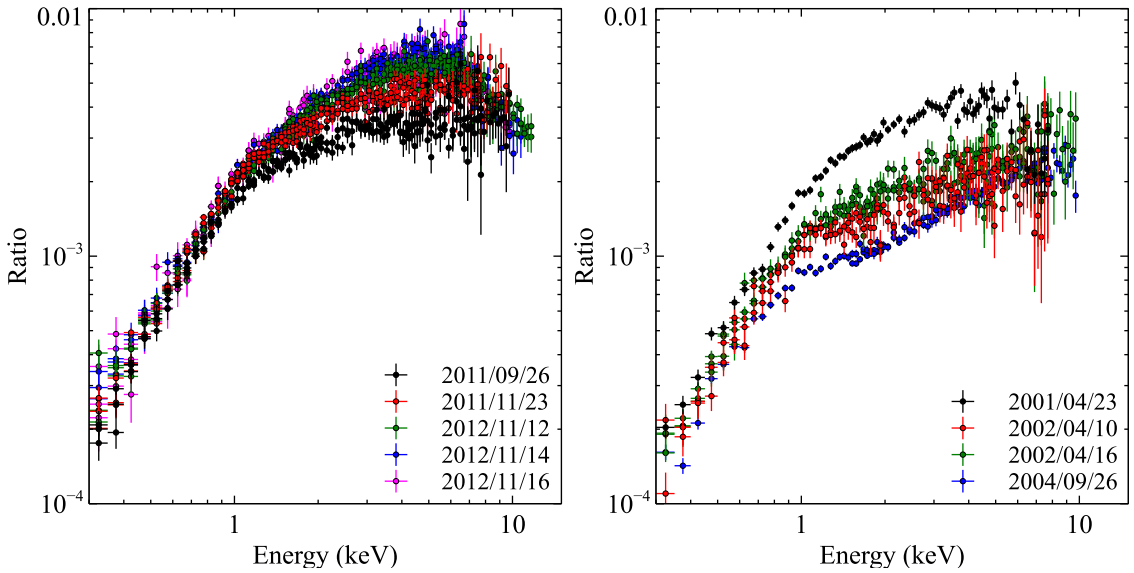

Figure 5.13. Ratios between the X-ray spectra of Holmberg IX X-1, and a response-folded PL model with $\Gamma = 2$. Spectra with luminosities higher than 1.5×10^{40} erg sec^{-1} are shown in the left panel, and those with lower luminosity in the right panel.

became unrecognizable in the highest-luminosity spectra, whose shape is characteristic the Disk-like state. This is consistent with the characteristics of the spectral transition observed in IC 342 X-1.

5.3.3 Model fitting and results

The result of the spectral fitting is summarized in table 5.3, in the same way as for the previous objects. The deconvolved spectra and their fit residuals are in figure 5.14. The MCD+THC fit was again successful on all the spectra presented in figure 5.13. The obtained T_e and T_{in} are similarly low, like in the previous objects.

As expected from the PL ratios, R_{raw} is relatively well constrained in the spectra with low luminosities, in which the soft excess is clearly seen. As source approaches the Disk-like state (e.g., 2012/11/12) with increasing its luminosity, the directly-visible disk becomes less required, and eventually only upper-limits are obtained for R_{raw}. Meanwhile, the coronal temperature has decreased from $T_e \sim 3$ keV to $T_e \sim 1.7$ keV and the inner-disk temperature increased up to 0.5-$-$0.7 keV, making the difference between the two temperatures smaller. Thus, the tendency of the change in the parameters between the two characteristic spectral states are also kept in Holmberg IX X-1.

Table 5.3: Parameters obtained from the spectral fitting in Holmberg IX X-1.

Date[a] YY/MM/DD	N_H[b]	T_e (keV)	Γ	τ[c]	T_{in} (keV)	R_{raw}[d]	R_{tot}[e]	L_{disk}[f]	L_X[g]	χ^2/ν (ν)
XMM-Newton										
01/04/23	$1.1^{+0.4}_{-0.2}$	1.3 ± 0.2	< 1.7	> 20	0.4 ± 0.2	$0.7^{+0.5}_{-0.2}$	1.0	3.3	17.4	1.18 (72)
02/04/10	$1.1^{+0.3}_{-0.2}$	$2.7^{+1.1}_{-0.5}$	$1.68^{+0.05}_{-0.07}$	14	$0.27^{+0.05}_{-0.04}$	$1.4^{+0.8}_{-0.4}$	2.0	2.7	10.1	1.06 (237)
02/04/16	$1.5^{+0.5}_{-0.4}$	> 3.5	$1.78^{+0.05}_{-0.03}$	< 11	$0.20^{+0.04}_{-0.03}$	$2.6^{+2.5}_{-1.3}$	4.2	3.6	11.8	1.09 (237)
04/09/26	1.6 ± 0.2	2.6 ± 0.2	1.55 ± 0.02	16	0.23 ± 0.02	$2.3^{+0.6}_{-0.5}$	2.9	3.3	9.0	1.16 (213)
11/09/26	$1.5^{+0.4}_{-0.3}$	$2.6^{+0.6}_{-0.3}$	1.84 ± 0.03	12	$0.20^{+0.09}_{-0.05}$	< 4.7	4.3	3.8	16.7	1.05 (237)
11/11/23	$1.1^{+0.2}_{-0.1}$	$2.6^{+0.4}_{-0.3}$	$1.82^{+0.04}_{-0.03}$	13	0.33 ± 0.08	< 0.5	1.7	4.4	20.7	1.09 (237)
XMM-Newton+NuSTAR										
12/11/12	0.7 ± 0.1	2.1 ± 0.1	$1.77^{+0.07}_{-0.05}$	14	$0.55^{+0.02}_{-0.01}$	< 0.5	0.7	5.9	22.9	1.18 (287)
12/11/14	$1.1^{+0.4}_{-0.3}$	1.62 ± 0.05	1.57 ± 0.02	20	$0.24^{+0.1}_{-0.08}$	< 2.3	2.9	3.6	24.5	1.22 (276)
12/11/16	0.4 ± 0.2	$2.0^{+0.3}_{-0.1}$	$1.87^{+0.3}_{-0.1}$	18	0.77 ± 0.2	< 0.4	0.4	7.2	24.0	1.23 (270)

a: Date of the observation.

b: Intrinsic column density of equivalent Hydrogen in units of 10^{21} cm^{-2}.

c: Optical depth of the coronal electron cloud.

d: Apparent inner-disk radius of the un-scattered accretion disk component in units of 1000 km.

e: Inner-disk radius of the overall disk component in units of 1000 km. Calculated from equation 5.3

f: Bolometric luminosity of the accretion disk component in units of 10^{39} erg sec^{-1}.

g: Absorbed $0.3 - 10$ keV band luminosity in units of 10^{39} erg sec^{-1}.

5.3.4 Search for spectral features from iron Kα

As we have seen so far, the spectra of each ULX are featureless, and require no additional components apart from the continuum models. This is surprising, because (as described in section 2.1.5) accreting objects usually exhibit rich local features in their spectra. Especially, K-α emission/absorption lines from the most abundant heavy metal, Iron, are ubiquitously detected in most of the accreting objects.

Due to its hard spectrum, Holmberg IX X-1 supplies a large number of photons with energy above the iron K-edge (7.12 keV), which makes it one of the most suitable sources to search for such iron line features. In this section, we searched for features by utilizing the large spectral sample of Holmberg IX X-1 accumulated with *XMM-Newton*.

Since the spectra from individual observations did not bear any features, the possible line structures, if any, must be extremely weak. To search for such features under the highest signal-to-noise ratio, we produced a single EPIC PN X-ray spectrum with extremely high statistics, by stacking all of the available observational data sets. The total exposure of the stacked spectrum is 132 ks, which is equivalent to nearly 10 times of ordinary *XMM-Newton* observations.

Since our present interest is on features due to iron Kα, we restricted the analyzing energy band to $4 - 8.5$ keV, which sufficiently covers lines from neutral (6.40 keV) to hydrogen-like (6.97 keV) iron even considering Doppler shifts up to $\sim$ 20% of the light speed. We first fit this spectrum with a cutoff power law model which approximates the curving continuum around 6 keV. Then, we add a narrow (10 eV width) Gaussian function to examine the significance of the line feature at that energy. We swept the above energy band by changing the center energy of the Gaussian with a step of 10 eV. In order to allow the feature to be an absorption line as well, the normalization of the Gaussian function was also allowed to take negative values.

The result on this line search is shown in figure 5.15. The top panel presents the actual stacked spectrum fitted with a cutoff PL model, and the best fit equivalent width (blue dotted line) and its 99% confidence range (light blue band) is shown in the bottom panel. Thus, the stacked spectrum did not require any narrow emission/absorption line features either, in the $4 - 9$ keV band. Especially around the energy where the iron Kα lines are expected at rest frame (red dashed lines), we obtained stringent limit of < 30 eV which is consistent with the result in Walton et al. (2013).

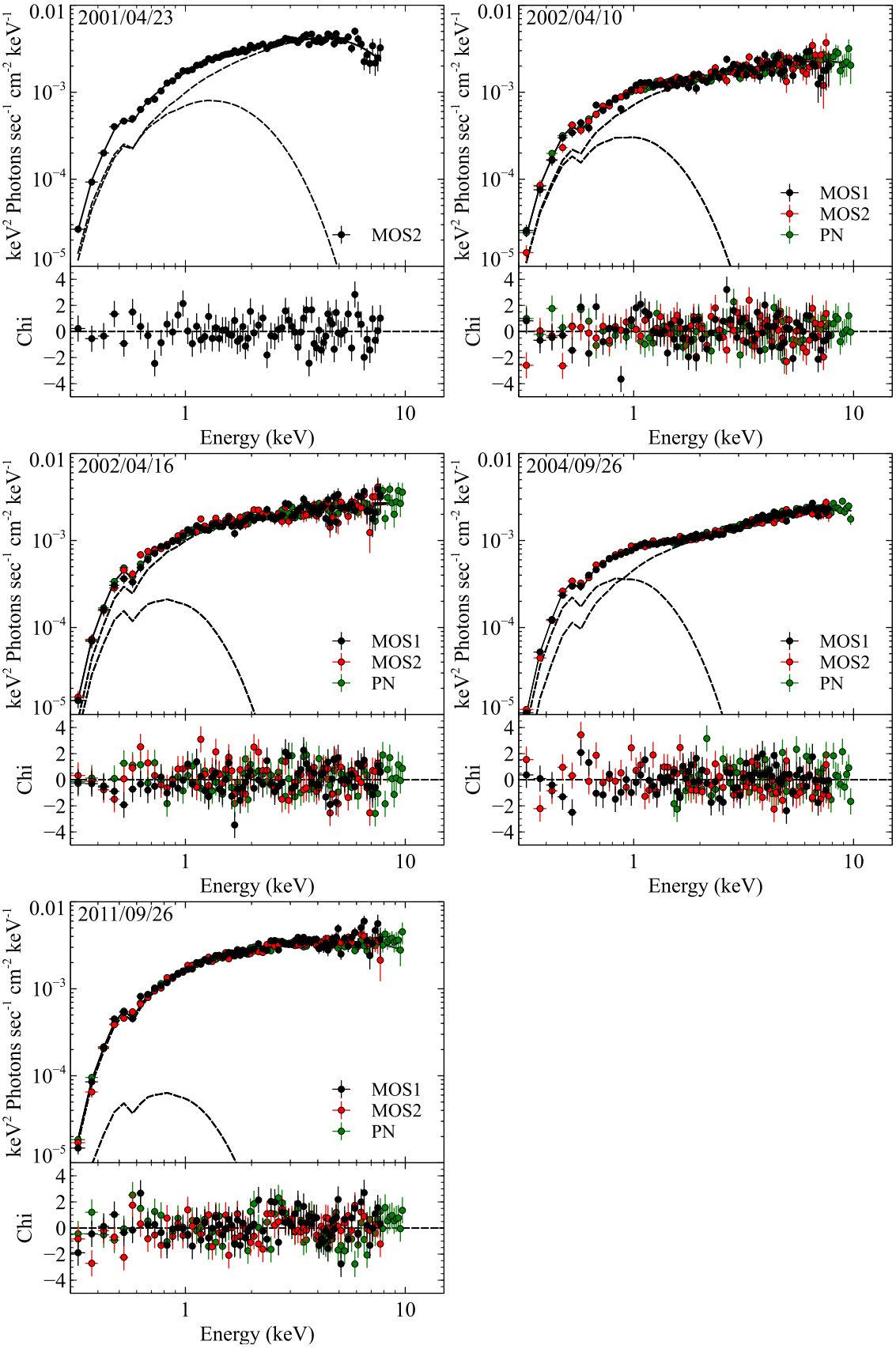

Figure 5.14. Spectra of Holmberg IX X-1 fitted and deconvolved with the MCD+THC model (top) and their residuals (bottom). The contributions of the MCD and THC components are drawn with the spectra in dashed lines.

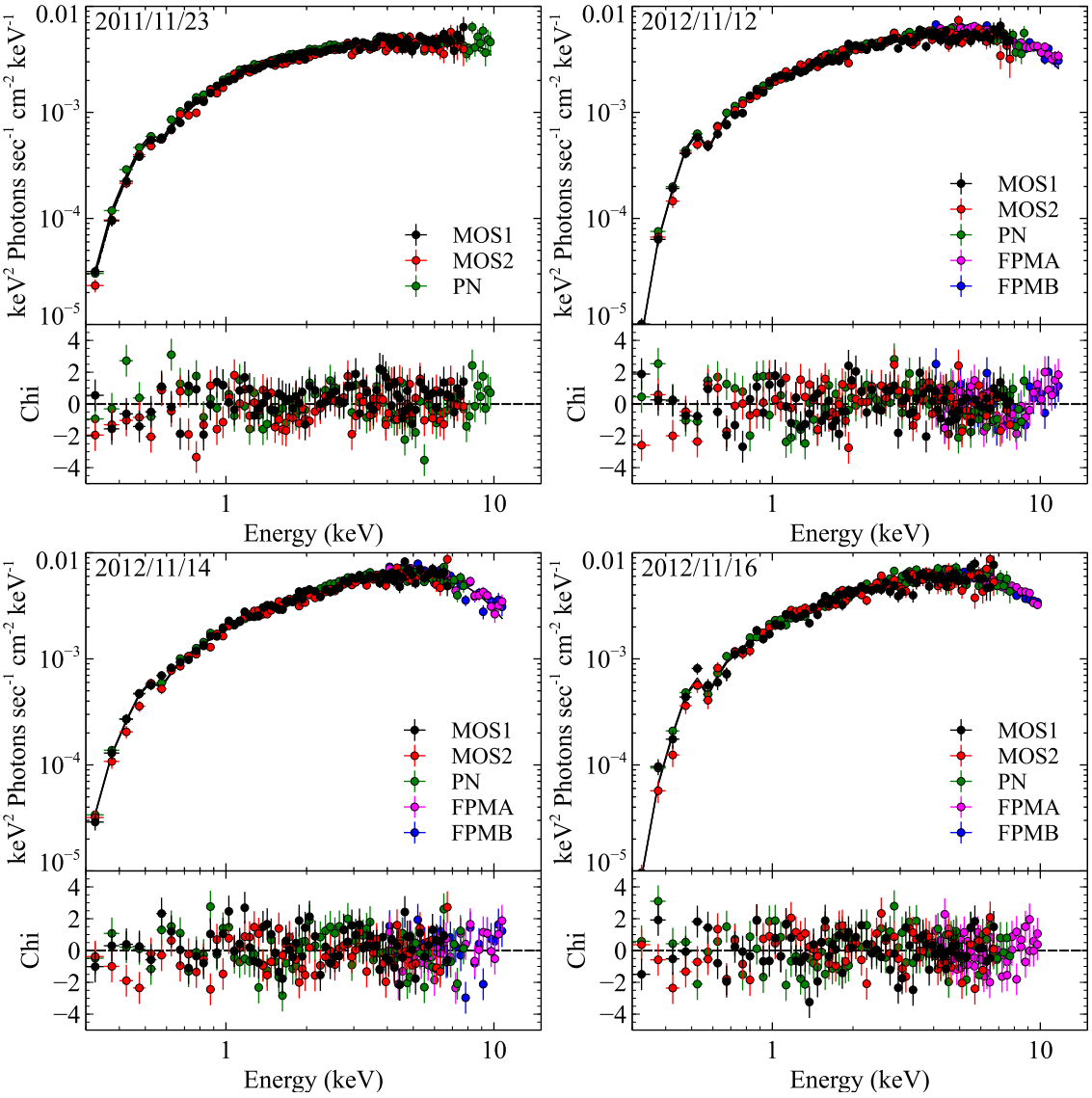

Figure 5.14. Continued.

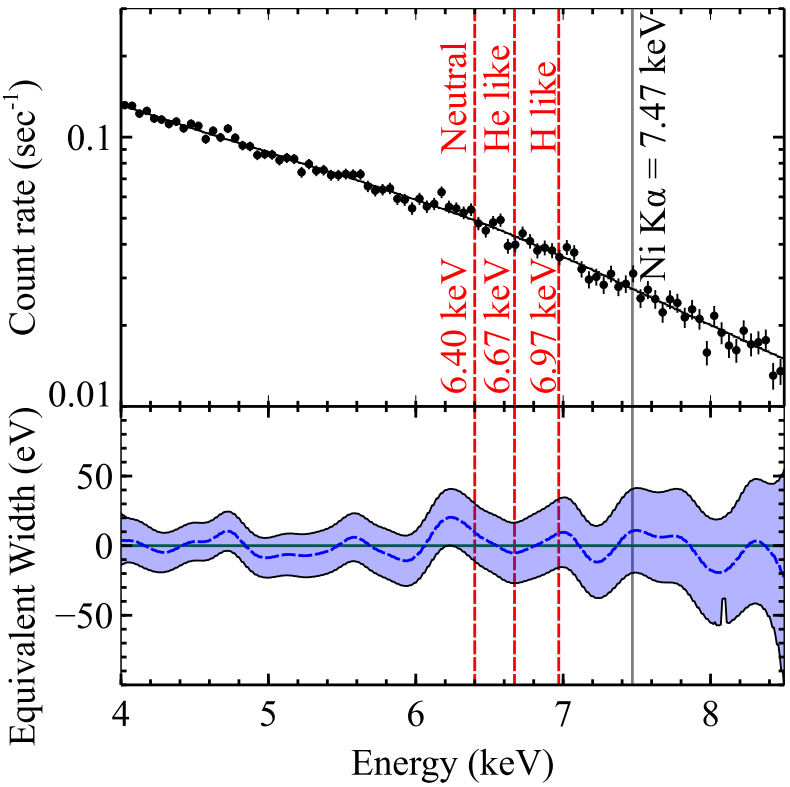

Figure 5.15. (Top) The stacked EPIC PN spectrum of Holmberg IX X-1. (Bottom) The allowed equivalent widths of narrow emission/absorption lines, of which the line center is fixed to a given energy. The X-ray spectrum is fitted with a cutoff PL model (solid line). The blue dashed line represents the best fit equivalent width, while the light blue band is 99% confidence region.

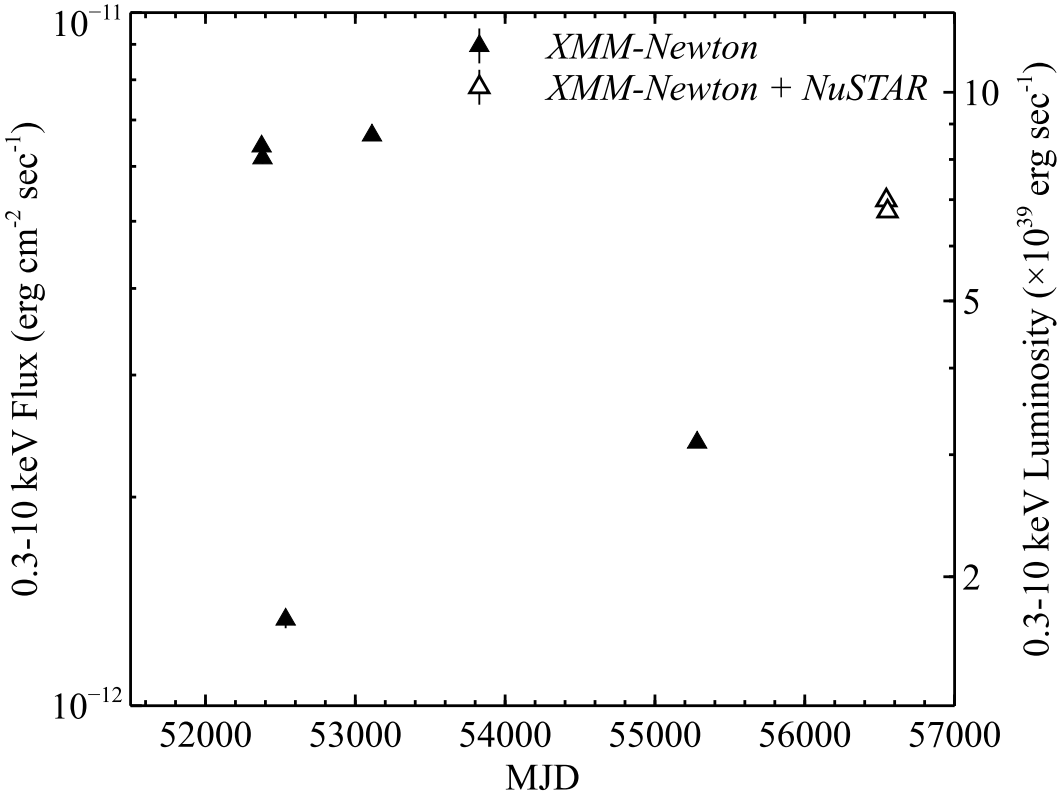

Figure 5.16. Long term variability of Holmberg II X-1.

5.4 Holmberg II X-1

5.4.1 Intensity variations

There were 7 observations of Holmberg II X-1 between 2002/04/10 and 2013/09/17. Five times with *XMM-Newton*, and three times with *XMM-Newton* combined with *NuSTAR*. As can be seen in figure 5.16, the source changed its luminosity by a factor of five around the average luminosity of 7×10^{39} erg sec^{-1}, which is in a middle range among the sources in the present thesis. The luminosity was calculated by assuming an isotropic emission at the distance of the Holmberg II galaxy, 3.3 Mpc.

5.4.2 Broad band spectra and their variations

The PL ratios of the Holmberg II X-1 spectra are presented in figure 5.17. They are again split in two groups in terms of the $0.3 - 10$ keV luminosity. Those with luminosities higher than 5×10^{39} erg sec^{-1} are shown in the left panel, and the rest are in the right panel. As is common in the other ULXs, Holmberg II X-1 exhibits stronger variability above 1 keV and showed the two-humped PL state spectrum on several occasions. However, unlike the other three ULXs shown in the previous sections, the continuum slope of the PL component was always soft. Hence the low energy hump is relatively stronger than the higher energy PL continuum. Especially, at the lowest luminosity (2002/09/18), the spectrum became extremely soft and the cutoff energy has decreased as well, which is somewhat similar to the lowest luminosity spectrum of NGC 1313 X-1.

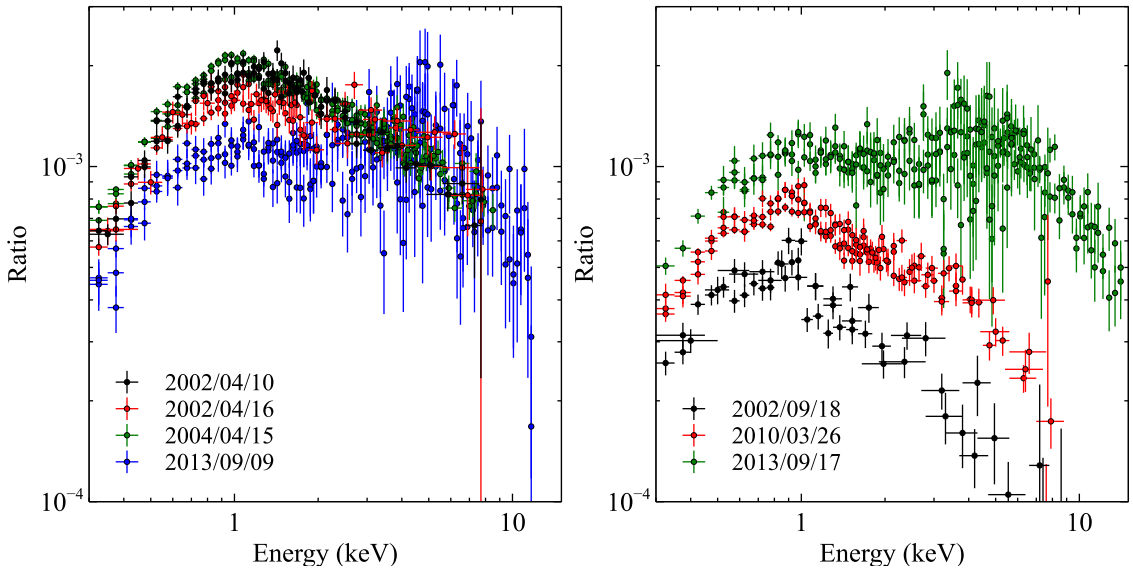

Figure 5.17. Ratios between the X-ray spectra of Holmberg IX X-1, and a response-folded PL model with $\Gamma = 2$. Spectra with luminosities higher than 5×10^{39} erg sec^{-1} are shown in the left panel, and those with lower luminosities in the right panel.

5.4.3 Model fitting and results

In spite of the different spectral shapes from the other ULXs, the MCD+THC modeling was still successful to explain the spectra of Holmberg II X-1 as summarized in table 5.4. As can be seen from the fitted X-ray spectra in figure 5.18, the cutoff energy, i.e. the coronal temperature is poorly constrained in some spectra due to its soft continuum shape and low S/N ratio above 7 keV. However, apart from those, the common characteristics of the ULXs (low $T_{\rm in}$ disk with cool and thick corona) holds in this source as well.

While the luminosity changed over $(1.9 - 8.9) \times 10^{39}$ erg sec^{-1}, $T_{\rm in}$ and $N_{\rm H}$ were both constant within the errors. Instead, the spectral shape variation was mostly carried by changes in the THC component, as easily expected from figure 5.17. Especially in the lowest-luminosity spectrum, $T_{\rm e}$ became much lower than in the others (0.8 keV), which is similar to the soft spectrum observed in NGC 1313 X-1.

Table 5.4: Physical parameters obtained from the spectral fitting.

Date[a] YY/MM/DD	N_H[b]	T_e (keV)	Γ	τ[c]	T_{in} (keV)	R_{raw}[d]	R_{tot}[e]	L_{disk}[f]	L_X[g]	χ^2/ν (ν)
XMM-Newton										
02/04/10	0.5 ± 0.2	> 3.8	$2.59^{+0.05}_{-0.14}$	< 18	0.21 ± 0.05	< 2.4	3.9	3.8	8.9	1.13 (227)
02/04/16	0.4 ± 0.2	> 2.0	$2.2^{+0.3}_{-0.2}$	< 11	$0.22^{+0.03}_{-0.02}$	$2.3^{+1.2}_{-0.6}$	3.5	3.8	8.7	1.20 (202)
02/09/18	$0.4^{+0.4}_{-0.3}$	$0.8^{+1.0}_{-0.3}$	< 2.6	> 15	$0.19^{+0.06}_{-0.04}$	$2.6^{+2.0}_{-0.9}$	3.0	3.7	1.9	0.98 (147)
04/04/15	0.4 ± 0.1	$3.7^{+5.5}_{-1.0}$	$2.39^{+0.08}_{-0.07}$	7	0.21 ± 0.03	$1.9^{+0.5}_{-0.4}$	4.1	4.2	9.3	1.2 (160)
10/03/26	0.3 ± 0.1	$1.4^{+0.3}_{-0.2}$	2.1 ± 0.1	15	0.21 ± 0.02	$2.4^{+0.5}_{-0.4}$	2.9	2.1	3.5	1.09 (209)
XMM-Newton+NuSTAR										
13/09/09	0.7 ± 0.3	$2.2^{+0.5}_{-0.3}$	1.88 ± 0.07	13	$0.19^{+0.03}_{-0.02}$	$3.8^{+1.9}_{-1.2}$	4.7	3.7	7.0	1.05 (246)
13/09/09	$0.3^{+0.3}_{-0.2}$	$2.4^{0.2}_{-0.1}$	1.92 ± 0.06	12	0.20 ± 0.03	$2.8^{+1.7}_{-1.0}$	3.8	2.9	6.9	1.03 (258)

a: Date of observation.

b: Intrinsic column density of equivalent Hydrogen in units of 10^{21} cm^{-2}.

c: Optical depth of the coronal electron cloud.

d: Apparent inner-disk radius of the un-scattered accretion disk component in units of 1000 km.

e: Inner-disk radius of the overall disk component in units of 1000 km. Calculated from equation 5.3

f: Bolometric luminosity of the accretion disk component in units of 10^{39} erg sec^{-1}.

g: Absorbed $0.3 - 10$ keV band luminosity in units of 10^{39} erg sec^{-1}.

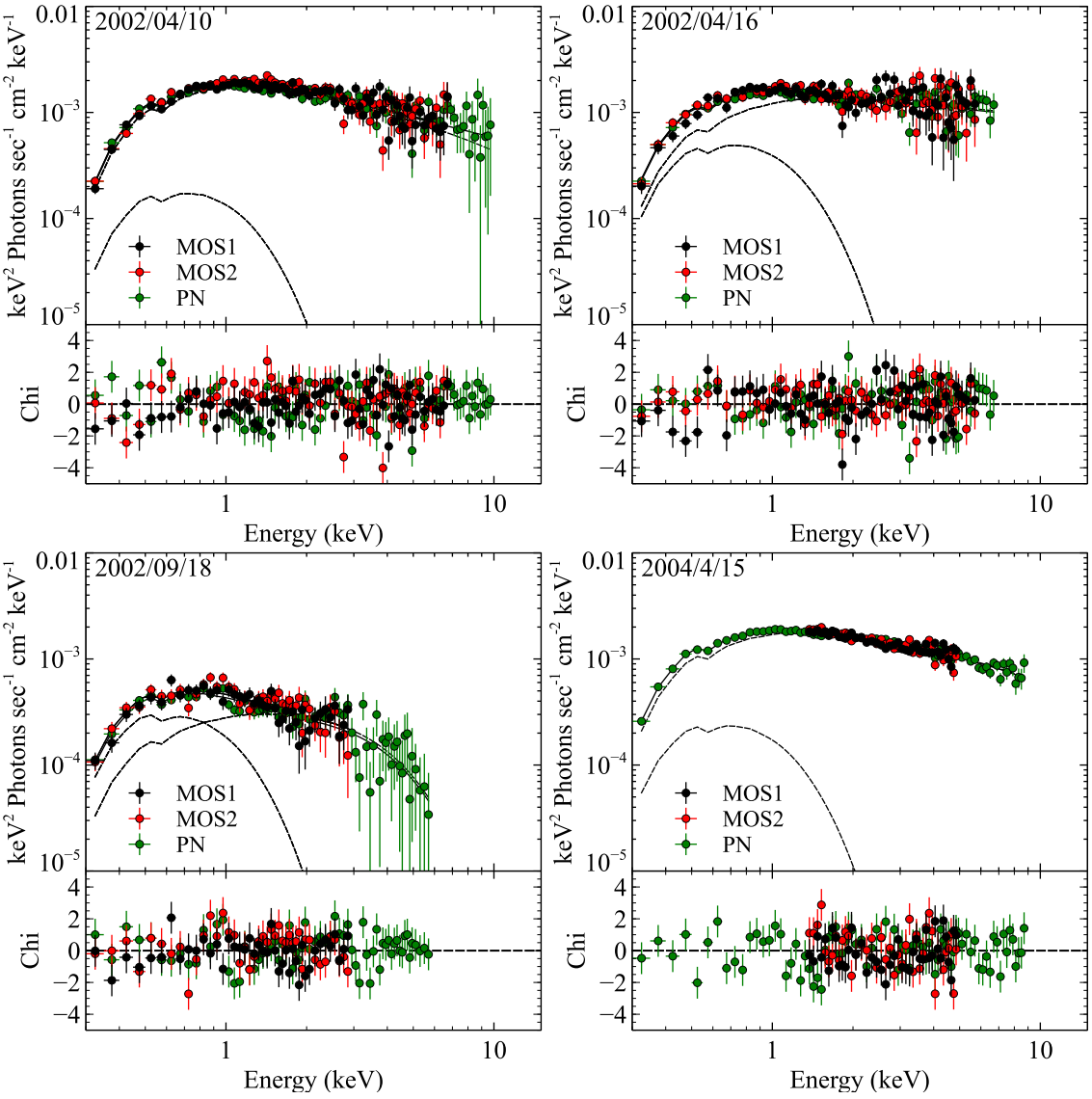

Figure 5.18. Spectra of Holmberg II X-1 fitted and deconvolved with the MCD+THC model (top) and their residuals (bottom). The contributions of the MCD and THC components are drawn with the spectra in dashed lines.

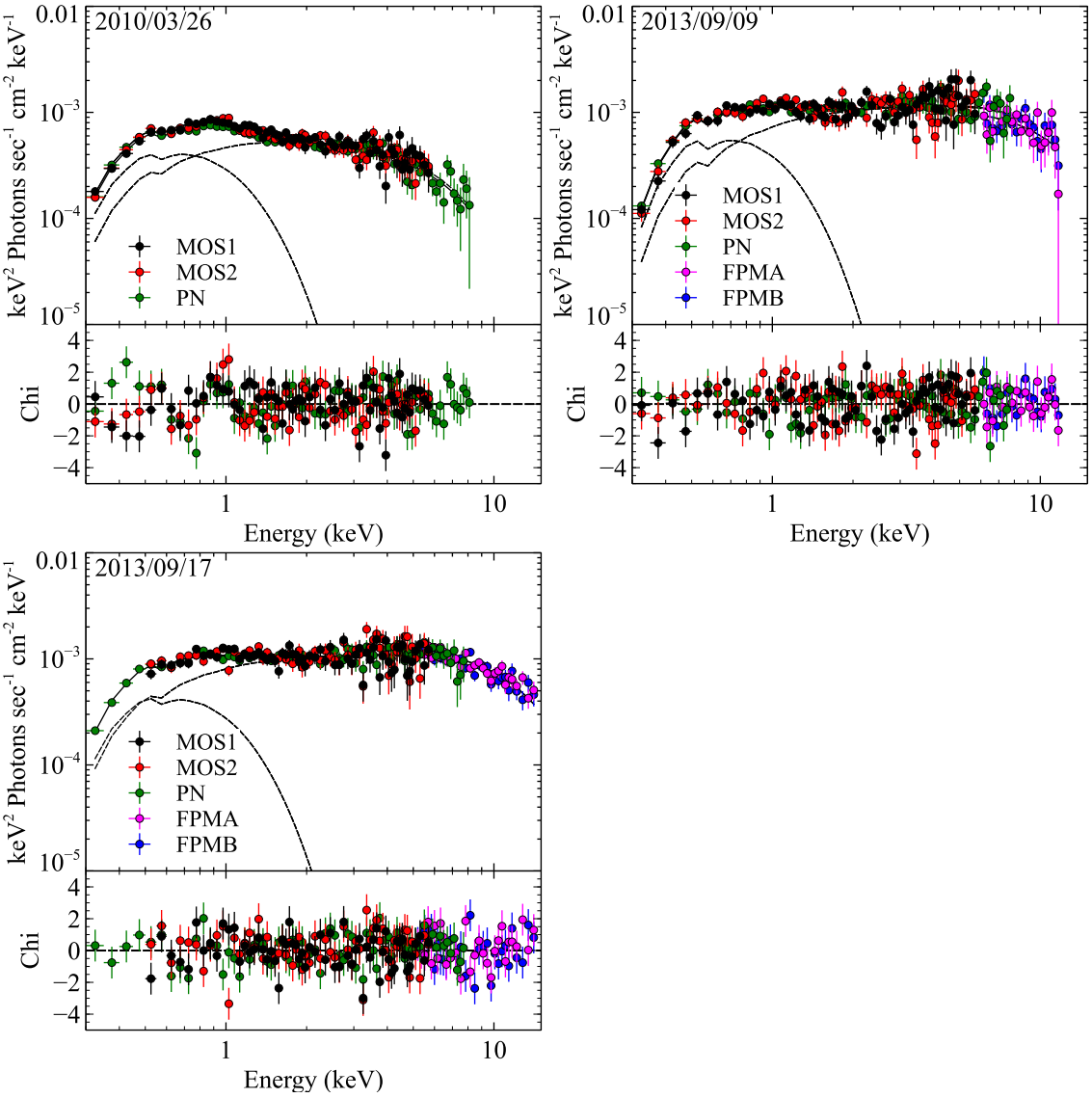

Figure 5.18. Continued.

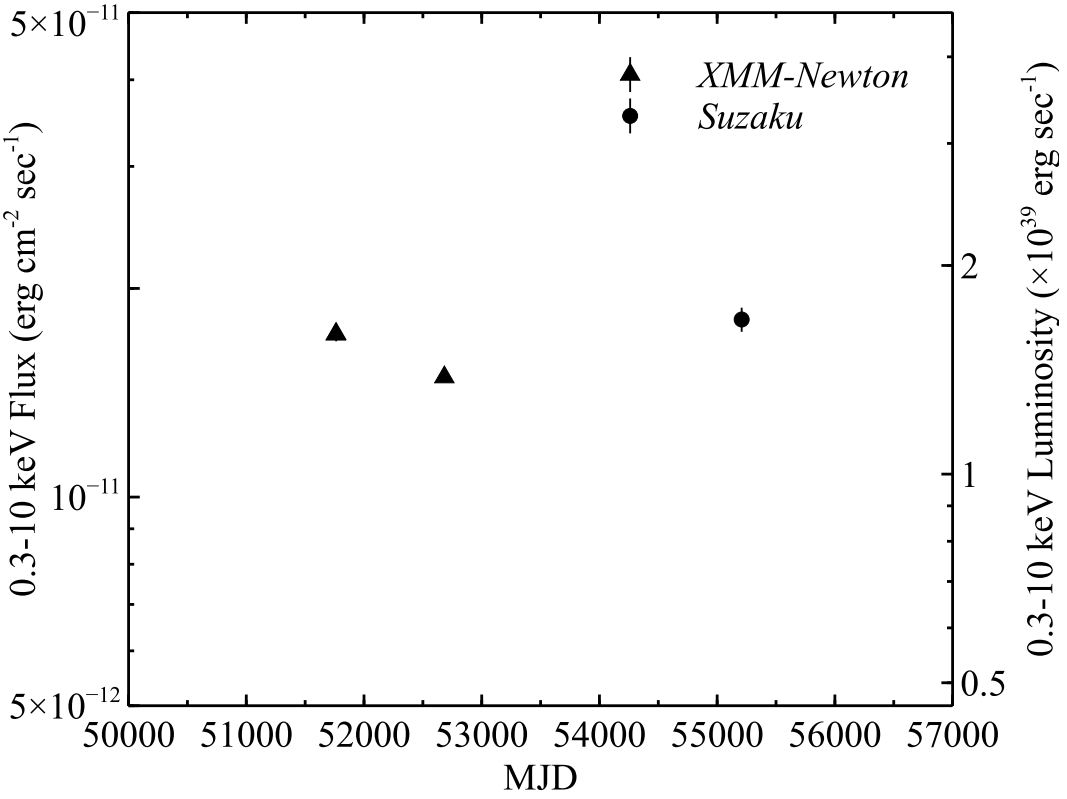

Figure 5.19. Long term variability of M33 X-8.

5.5 M33 X-8

This is the ULX with the lowest average luminosity in our sample (section 4.2.5). It is located at the center region of the spiral galaxy M33. Although it is less luminous than the others, it has relatively high flux ($\sim 10^{-11}$ erg cm^{-2} sec^{-1}) because M33 belongs to our local group of galaxies.

As shown in figure 5.19, M33 X-8 did not vary very much, around the average of $\sim 1.4 \times 10^{39}$ erg sec^{-1} in $0.3 - 10$ keV.

Figure 5.20 presents the PL ratios of 4 observations of M33 X-8. Unlike the other sources, the spectrum resided in the Disk-like state on all occasions. Nevertheless, the spectral changes were limited to > 1 keV, and no local spectral features are present, just like in the other ULXs studied so far.

We fitted the spectra of M33 X-8 with the same MCD+THC model employed in the previous sources. The results are summarized in table 5.5. The model was successful to explain the round-shaped spectra of M33 X-8. Since the spectra have convex shapes with a low energy break at ~ 1.0 keV, we obtained higher $T_{\rm in}$ (~ 0.4 keV) than from the PL-states spectra of the other sources ($T_{\rm in} \sim 0.2$ keV). No directly visible disk component was required. Thus, the spectra of M33 X-8 posses all characteristics of the Disk-like state of ULXs, which we have confirmed in the previous sources.

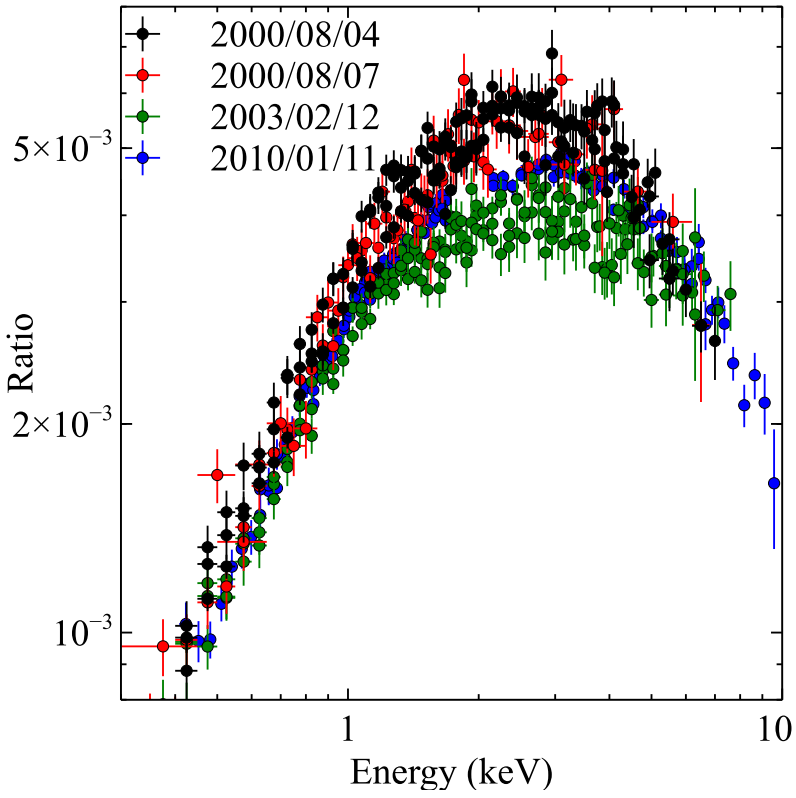

Figure 5.20. Ratios between the X-ray spectra of M33 X-8 and a response-folded PL model with $\Gamma = 2$.

Table 5.5: Physical parameters obtained from the spectral fitting.

Date[a] YY/MM/DD	N_H[b] (keV)	T_e	Γ	τ[c] (keV)	T_{in}	R_{raw}[d]	R_{tot}[e]	L_{disk}[f]	L_X[g]	χ^2/ν (ν)
				XMM-Newton						
00/08/04	$0.3^{+0.2}_{-0.1}$	$1.19^{+0.2}_{-0.08}$	$1.8^{+0.2}_{-0.1}$	19	0.4 ± 0.1	< 0.2	0.4	0.5	1.7	1.21 (204)
00/08/07	$0.2^{+0.2}_{-0.1}$	$1.6^{+1.6}_{-0.7}$	< 3.2	> 8	$0.53^{+0.3}_{-0.07}$	< 0.3	0.2	0.4	1.6	1.12 (172)
03/02/12	$0.25^{+0.09}_{-0.08}$	$2.2^{+1.1}_{-0.4}$	2.1 ± 0.1	11	$0.41^{+0.08}_{-0.04}$	< 0.1	0.3	0.3	1.4	1.10 (213)
				Suzaku						
10/01/11	0.12 ± 0.08	$1.9^{+0.2}_{-0.1}$	$2.06^{+0.08}_{0.06}$	12	0.5 ± 0.05	< 0.06	0.2	0.3	1.5	1.27 (136)

a: Date of the observation.

b: Intrinsic column density of equivalent Hydrogen in units of 10^{21} cm^{-2}.

c: Optical depth of the coronal electron cloud.

d: Apparent inner-disk radius of the un-scattered accretion disk component in units of 1000 km.

e: Inner-disk radius of the overall disk component in units of 1000 km.

f: Bolometric luminosity of the accretion disk component in units of 10^{39} erg sec^{-1}.

g: Absorbed $0.3 - 10$ keV band luminosity in units of 10^{39} erg sec^{-1}.

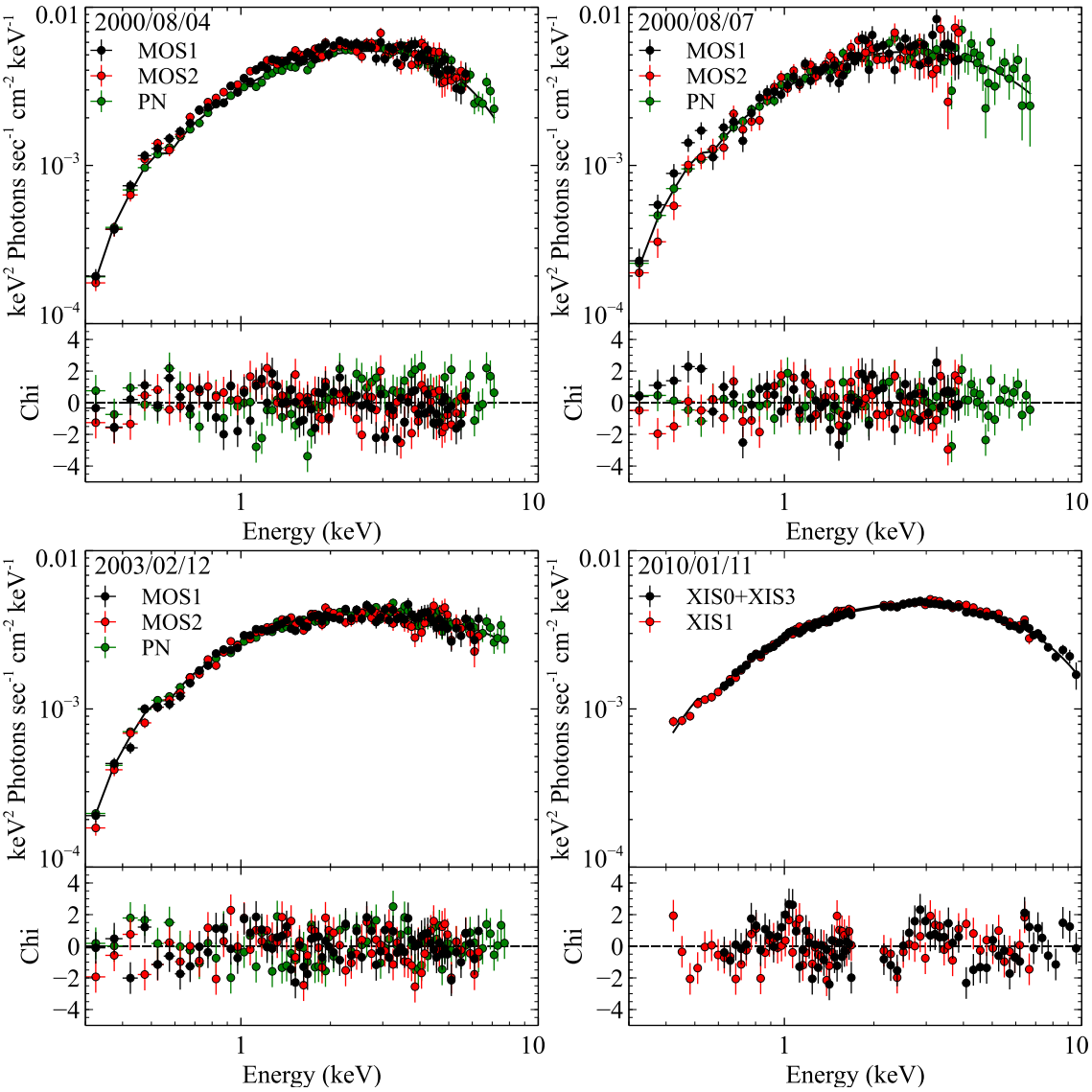

Figure 5.21. Spectra of M33 X-8 fitted and deconvolved with the MCD+THC model (top panels) and their residuals (bottom panels). The contributions of the MCD and THC components are drawn with the spectra in dashed lines.

5.6 The other ULXs

5.6.1 M83 ULX1/ULX2

These are ULXs associated with the arms of a face-on spiral galaxy M83 at a distance of 4.61 Mpc (section 4.2.6), which are as less luminous as M33 X-8. Unlike M33 X-8, both showed spectral transitions as can be seen in the PL ratio shown in figure 5.22 and figure 5.23. At the dimmest moment, both resided in the PL states with soft excesses at $\sim$ 0.8 keV, which are similar to the concave PL state observed in Holmberg IX X-1, Holmberg II X-1, and NGC 1313 X-1, but with lower cutoff energy at $\sim$ 3 keV. As the sources got brighter, both spectra became more convex toward the Disk-like state. ULX1 showed harder continuum in the Disk-like state than the ULX2.

We similarly fitted the spectra with the MCD+THC modeling. The model was successful to reproduce the spectra of both ULXs as summarized in table 5.6, figure 5.24, and figure 5.25. The spectra were less absorbed, which indicated 5×10^{20} cm^{-2} or even less. Due to the low cutoff energies, $T_{\rm e}$ was significantly low ($<$ 1.5 keV) throughout the observations. While the spectra showed $T_{\rm in}$ of $\sim$ 0.2 keV in the PL states, the spectra in the Disk-like state tended to exhibit slightly higher temperature of $T_{\rm in} = 0.3 - 0.4$ keV.

5.6.2 NGC 4190 X-1

NGC 4190 is a dwarf galaxy located at a distance of 3.5 Mpc, hosting a ULX called X-1 (section 4.2.6). PL ratios of the X-1 are shown in figure 5.26. It exhibited convex spectra with roll over at 4 keV at the dimmest, at 6 keV at the brightest. Although it became twice brighter from 2010/06/06 to 2010/11/25, the source has been resided in a similarly convex spectral state.

Results of the spectral fitting with the MCD+THC modeling are presented in table 5.7 and figure 5.27. The $0.3 - 10$ keV luminosity was $(3.6 - 8.5) \times 10^{39}$ erg sec^{-1}, which is in the middle range among our ULX sample. Due to the convex spectral shape, the spectra exhibited low $T_{\rm e}$ of 0.8- $- 1.6$ keV and high $T_{\rm in}$ of $0.2 - 0.4$ keV, making two temperatures close to one another.

5.6.3 NGC 253 ULX1

This is a ULX in the starburst galaxy NGC 253 (section 4.2.6). In this galaxy, there are another neighboring ULX called ULX2. Since it is less luminous than the ULX1, the source is excluded from the present analysis. According to the PL ratio in figure 5.28, the source resided in single spectral shape, which has as hard continuum ($\Gamma \sim 1.6$) as those in Holmberg IX X-1, and IC 342 X-1. Since the host galaxy is nearly edge on, the spectra are strongly absorbed at low energy band ($N_{\rm H} \sim 4 \times 10^{21}$ cm^{-2}).

The MCD+THC modeling successfully reproduced the spectra of NGC 253 ULX1. The results of the spectral fitting are shown in table 5.8 and figure 5.29. The $0.3 - 10$ keV luminosity distributed in $1.5 - 2.3 \times 10^{39}$ erg sec^{-1}, assuming isotropic emission from a distance of 3.2 Mpc (table 4.1). It is a one of the lowest luminosity among our ULX sample. Although the spectral shape seemed convex in the PL ratio, they actually required directly visible disk components in lower energy band. Hence, the spectra has slightly concave shape, exhibiting low $T_{\rm in}$ of $0.12 - 0.16$ keV. Due to low cutoff energy at $\sim$ 4 keV, obtained electron temperatures, $T_{\rm e} = 1.1 - 1.4$ keV, are lower than those in the representative ULXs such as Holmberg IX X-1 and NGC 1313 X-1 ($T_{\rm e} = 2.5 - 3$ keV).

5.6.4 NGC1313 X-2

This is a ULX which reside in NGC 1313. It is located with a $\sim 6'$ separation from X-1 (section 5.2). It exhibited luminosity between $2.2 - 4.8 \times 10^{39}$ erg sec^{-1}, which is in middle to lower regime among the present sample. As can be seen in the PL ratios (figure 5.30) of the spectra, X-2 always resided in the Disk-like state. As we have seen in other ULXs, the spectrum was stable below 1 keV, and the harder component showed strong variability.

The spectra were successfully fitted with the MCD+THC model (figure 5.31). Although the obtained $T_{\rm in}$ is relatively lower than those obtained in other Disk-like state spectra (e.g, NGC 1313 X-1; 0.9 keV), since the cutoff is at lower energy as well, the appearance of the spectrum is consistent with that of the Disk-like state. Furthermore, the spectra required no or little contribution from the directly visible disk component. Thus, the spectra posses the characteristics of the Disk-like state spectrum.

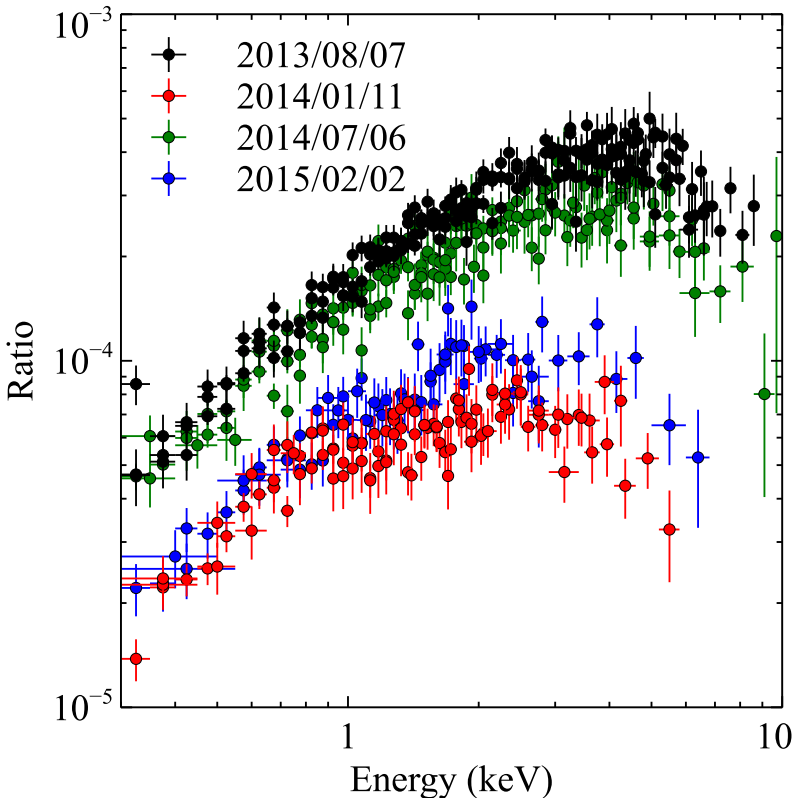

Figure 5.22. Ratios between the X-ray spectra of M83 ULX1 and a response-folded PL model with $\Gamma = 2$.

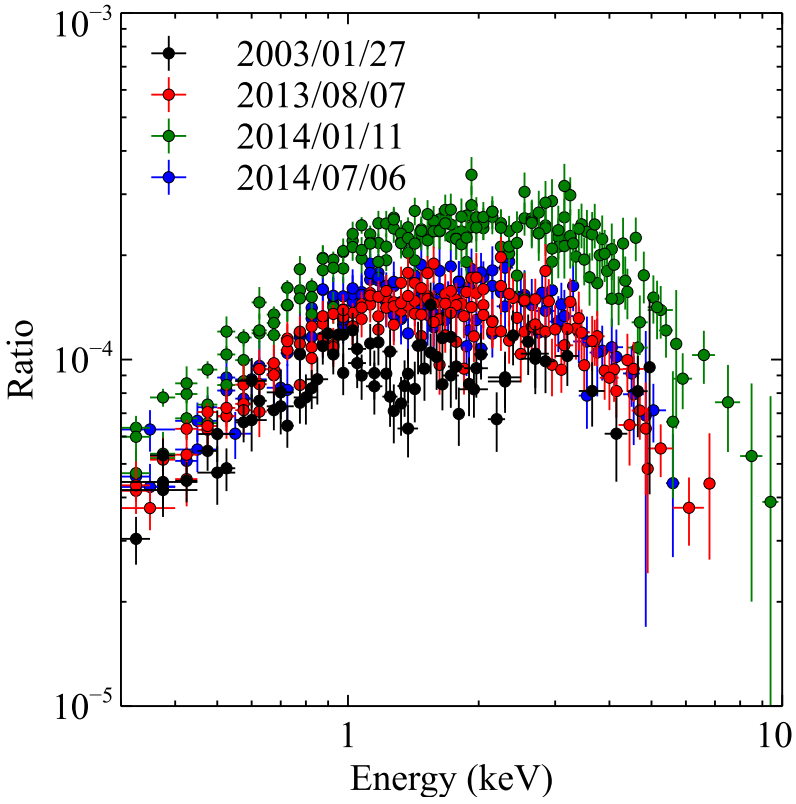

Figure 5.23. Ratios between the X-ray spectra of M83 ULX2 and a response-folded PL model with $\Gamma = 2$.

Table 5.6: Parameters obtained from the spectral fitting in M83 ULX1 and ULX2.

Date[a] YY/MM/DD	N_H[b]	T_e (keV)	Γ	τ[c]	T_{in} (keV)	R_{raw}[d]	R_{tot}[e]	L_{disk}[f]	L_X[g]	χ^2/ν (ν)
ULX1 *XMM-Newton*										
13/08/07	< 0.4	$1.35^{+0.1}_{-0.09}$	$1.58^{+0.05}_{-0.1}$	22	$0.28^{+0.16}_{-0.03}$	< 0.6	0.8	0.5	3.1	1.08 (222)
14/01/11	$0.8^{+0.7}_{-0.5}$	$0.9^{+0.3}_{-0.2}$	1.6 ± 0.3	28	$0.21^{+0.09}_{-0.05}$	$0.8^{+1.2}_{-0.4}$	1.0	0.3	1.1	0.82 (171)
14/07/06	< 8.2	1.3 ± 0.1	$1.6^{+0.07}_{-0.2}$	21	$0.28^{+0.2}_{-0.05}$	< 0.3	0.7	0.4	2.3	1.03 (227)
15/02/02	$1.1^{+1.1}_{-0.8}$	$0.9^{+0.3}_{-0.3}$	$1.7^{+0.2}_{-0.4}$	23	$0.17^{+0.1}_{-0.05}$	< 0.6	2.0	0.5	0.8	0.81 (150)
ULX2 *XMM-Newton*										
03/01/27	$0.4^{+0.4}_{-0.3}$	$0.71^{+0.2}_{-0.07}$	< 1.7	> 27	0.29 ± 0.06	$0.7^{+0.3}_{-0.2}$	0.7	0.4	0.8	1.26 (143)
13/08/07	$0.2^{+0.2}_{-0.1}$	$0.76^{+0.2}_{-0.05}$	< 2.1	> 19	$0.40^{+0.05}_{+0.1}$	0.4 ± 0.1	0.4	0.5	1.2	1.09 (195)
14/01/11	$0.1^{+0.2}_{-0.1}$	$0.9^{+0.2}_{-0.1}$	< 2.1	> 17	0.4 ± 0.1	< 0.5	0.5	0.8	2.5	1.12 (217)
14/07/06	0.5 ± 0.3	$0.73^{+0.3}_{-0.08}$	< 2.1	20.1	0.3 ± 0.1	$0.5^{+0.3}_{-0.2}$	0.6	0.4	1.2	1.15 (177)

a: Date of the observation.

b: Intrinsic column density of equivalent Hydrogen in units of 10^{21} cm^{-2}.

c: Optical depth of the coronal electron cloud.

d: Apparent inner-disk radius of the un-scattered accretion disk component in units of 1000 km.

e: Inner-disk radius of the overall disk component in units of 1000 km.

f: Bolometric luminosity of the accretion disk component in units of 10^{39} erg sec^{-1}.

g: Absorbed $0.3 - 10$ keV band luminosity in units of 10^{39} erg sec^{-1}.

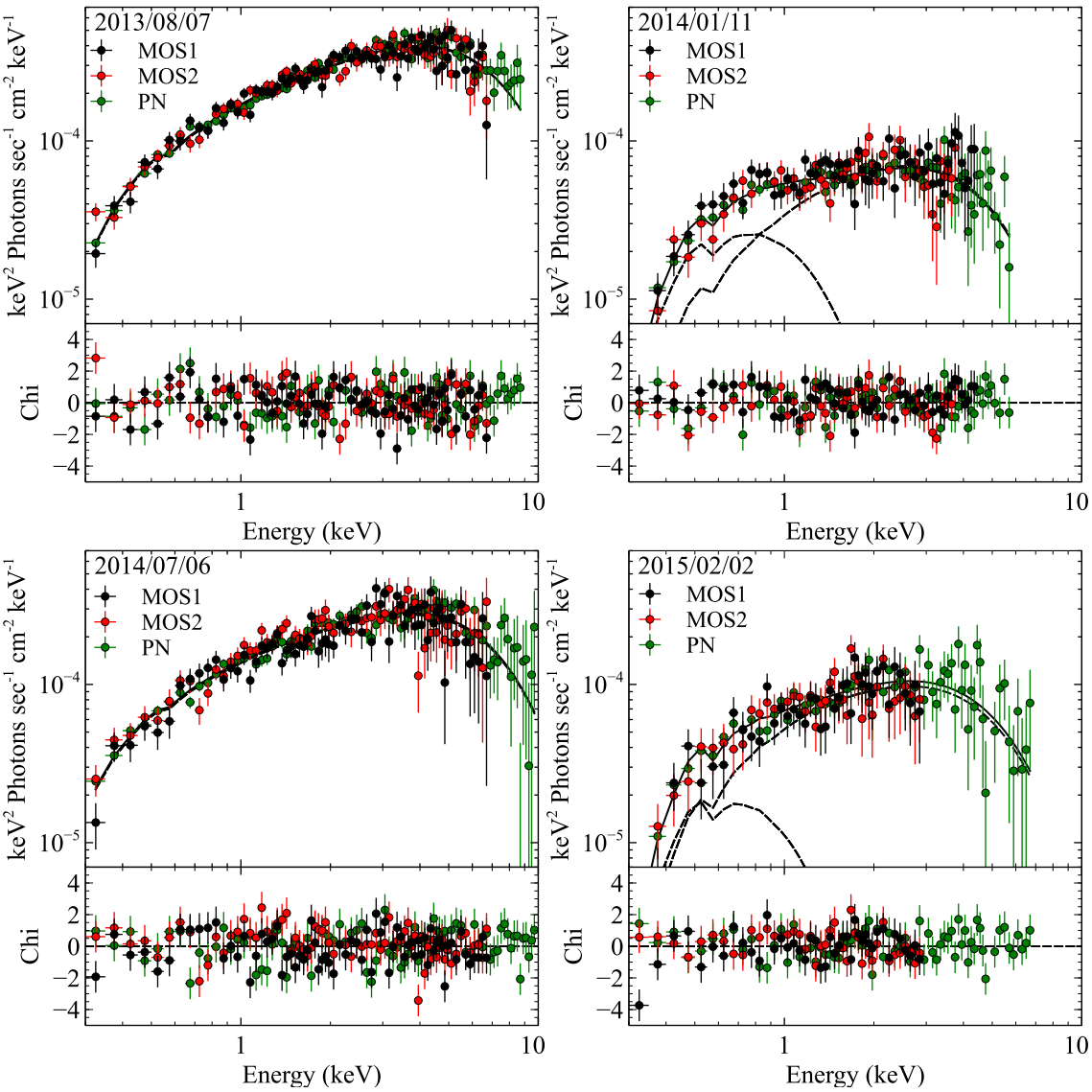

Figure 5.24. Spectra of M83 ULX1 fitted and deconvolved with the MCD+THC model (top panels) and their residuals (bottom panels). The contributions of the MCD and THC components are drawn with the spectra in dashed lines.

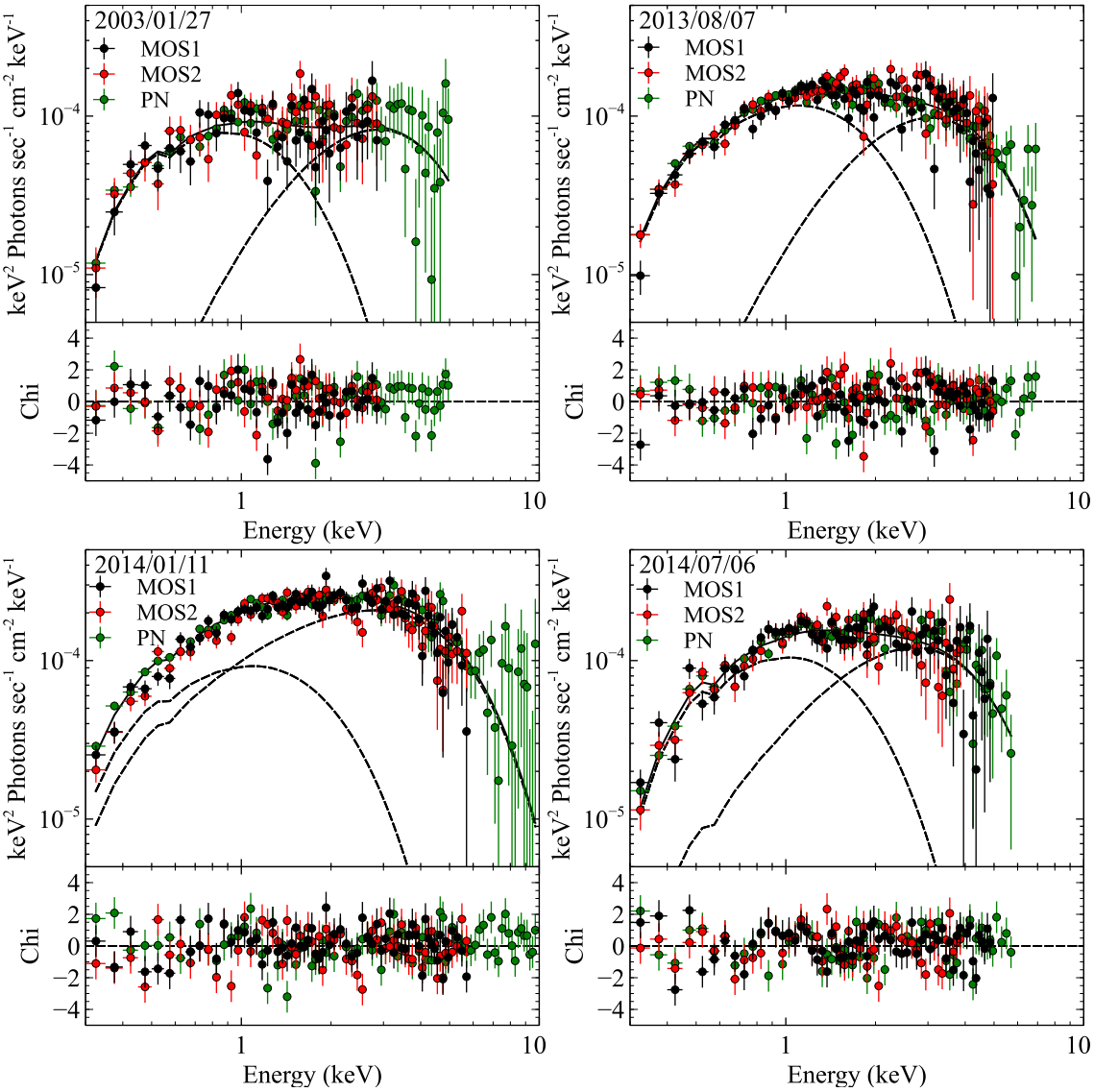

Figure 5.25. Spectra of M83 ULX2 fitted and deconvolved with the MCD+THC model (top panels) and their residuals (bottom panels). The contributions of the MCD and THC components are drawn with the spectra in dashed lines.

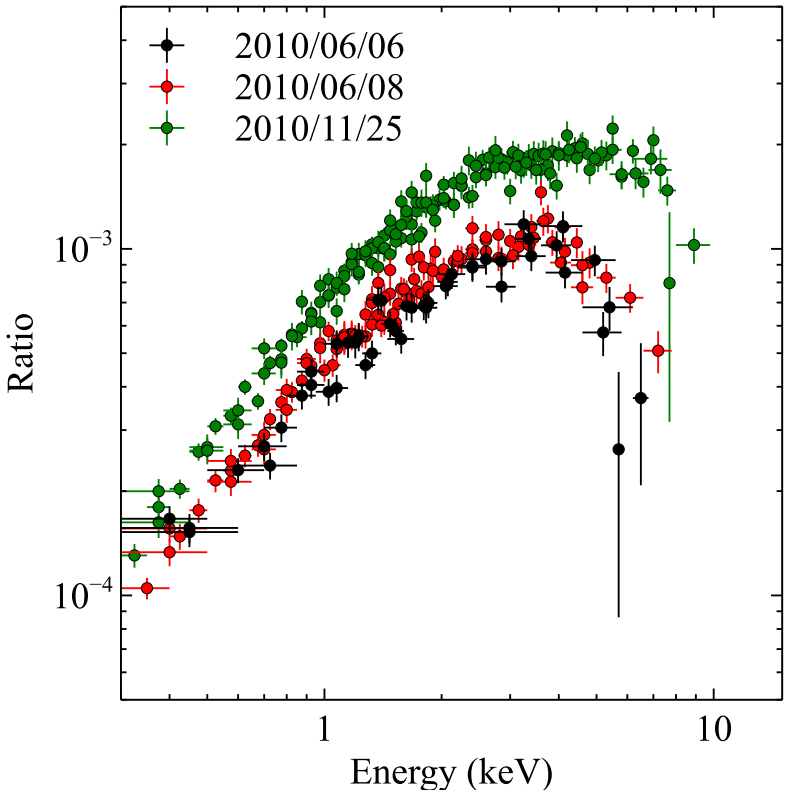

Figure 5.26. Ratios between the X-ray spectra of NGC4190 X-1 and a response-folded PL model with $\Gamma = 2$.

Table 5.7: Parameters obtained from the spectral fitting in NGC 4190 X-1.

Date[a] YY/MM/HH	N_H[b]	T_e (keV)	Γ	τ[c]	T_{in} (keV)	R_{raw}[d]	R_{tot}[e]	L_{disk}[f]	L_X[g]	χ^2/ν (ν)
XMM-Newton										
10/06/06	0.5 ± 0.4	$0.83^{+0.15}_{-0.04}$	< 2.2	> 18	$0.41^{+0.08}_{-0.2}$	$0.47^{+0.62}_{-0.14}$	0.52	0.9	3.6	1.15 (202)
10/06/08	$0.9^{+0.6}_{-0.4}$	$1.08^{+0.09}_{-0.1}$	$1.55^{+0.09}_{-0.12}$	25	$0.2^{+0.2}_{-0.1}$	< 1.7	1.4	0.4	4.5	1.19 (197)
10/11/25	0.6 ± 0.2	$1.6^{0.2}_{-0.3}$	< 1.7	> 18	$0.42^{+0.5}_{-0.1}$	< 0.5	0.6	1.2	8.5	1.08 (237)

a: Date of the observation.

b: Intrinsic column density of equivalent Hydrogen in units of 10^{21} cm^{-2}.

c: Optical depth of the coronal electron cloud.

d: Apparent inner-disk radius of the un-scattered accretion disk component in units of 1000 km.

e: Inner-disk radius of the overall disk component in units of 1000 km.

f: Bolometric luminosity of the accretion disk component in units of 10^{39} erg sec^{-1}.

g: Absorbed $0.3 - 10$ keV band luminosity in units of 10^{39} erg sec^{-1}.

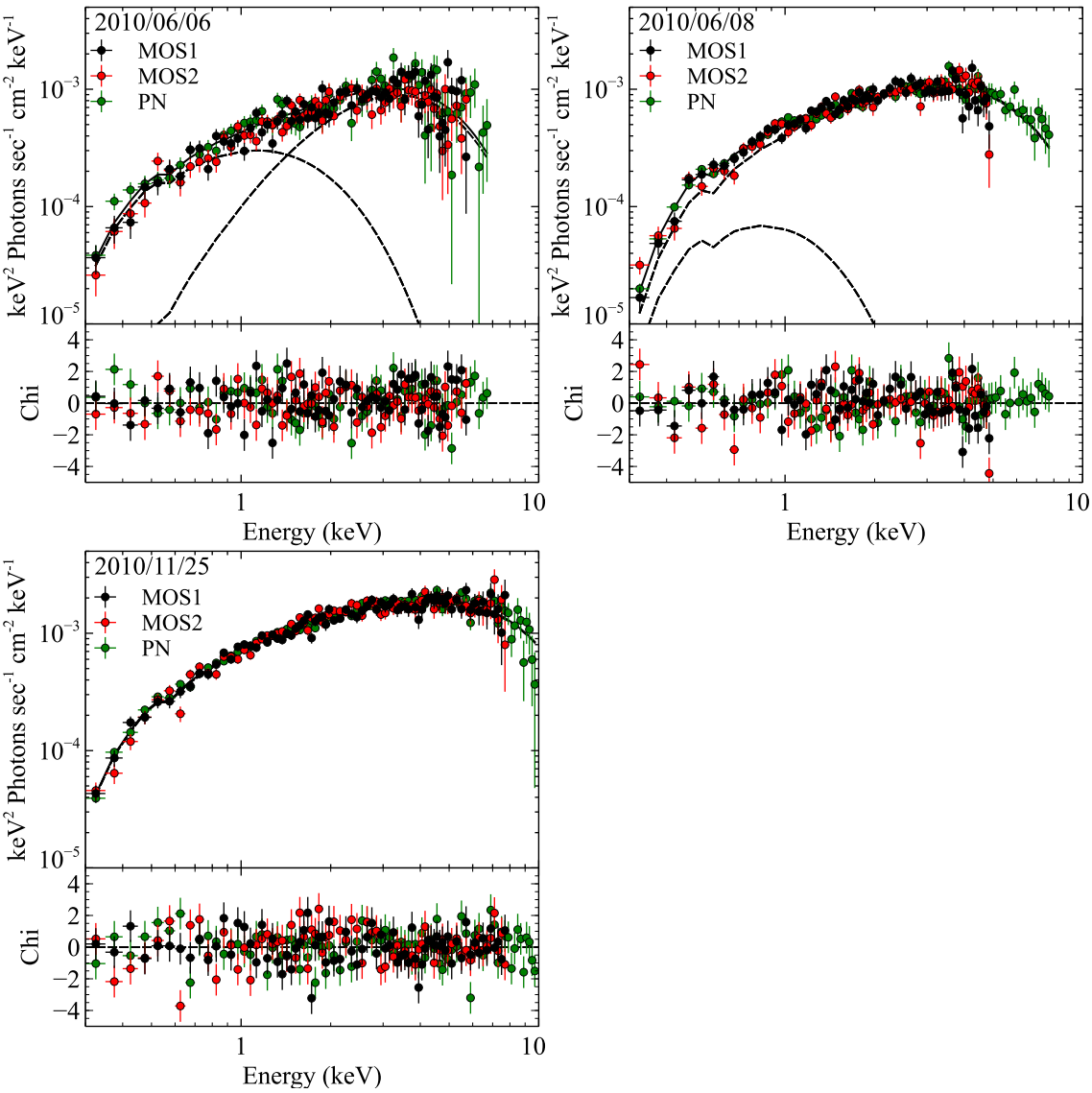

Figure 5.27. Spectra of NGC4190 X-1 fitted and deconvolved with the MCD+THC model (top panels) and their residuals (bottom panels). The contributions of the MCD and THC components are drawn with the spectra in dashed lines.

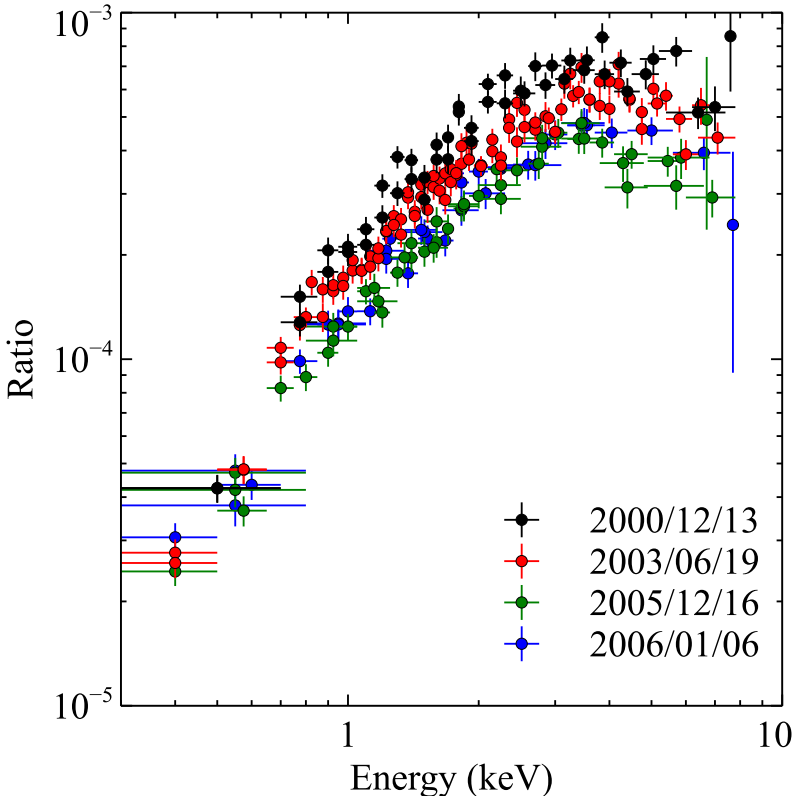

Figure 5.28. Ratios between the X-ray spectra of NGC253 ULX1 and a response-folded PL model with $\Gamma = 2$.

Table 5.8: Parameters obtained from the spectral fitting in NGC 253 ULX1.

Date[a] YY/MM/HH	N_H[b]	T_e (keV)	Γ	τ[c]	T_{in} (keV)	R_{raw}[d]	R_{tot}[e]	L_{disk}[f]	L_X[g]	χ^2/ν (ν)
XMM-Newton										
00/12/13	6^{+2}_{-3}	$1.4^{+0.3}_{-0.2}$	1.7 ± 0.2	19	$0.12^{+0.08}_{-0.02}$	$16.2^{+37.9}_{-15.1}$	16.7	7.4	2.3	1.27 (150)
03/06/19	4 ± 2	$1.4^{+0.2}_{-0.1}$	1.6 ± 0.1	21	$0.16^{+0.07}_{-0.03}$	$5.0^{+10.9}_{-4.0}$	5.4	2.1	1.9	1.26 (145)
05/12/16	3 ± 2	$1.1^{+0.2}_{-0.1}$	1.5 ± 0.2	27	$0.16^{+0.17}_{-0.04}$	$3.1^{+13.8}_{-2.8}$	3.4	0.8	1.3	1.05 (217)
06/01/06	5 ± 2	$1.4^{+0.5}_{-0.2}$	1.6 ± 0.2	19	$0.13^{+0.07}_{-0.03}$	$10.2^{+31.2}_{-8.7}$	10.5	3.9	1.5	1.19 (177)

a: Date of the observations.

b: Intrinsic column density of equivalent Hydrogen in units of 10^{21} cm^{-2}.

c: Optical depth of the coronal electron cloud.

d: Apparent inner-disk radius of the un-scattered accretion disk component in units of 1000 km.

e: Inner-disk radius of the overall disk component in units of 1000 km.

f: Bolometric luminosity of the accretion disk component in units of 10^{39} erg sec^{-1}.

g: Absorbed $0.3 - 10$ keV band luminosity in units of 10^{39} erg sec^{-1}.

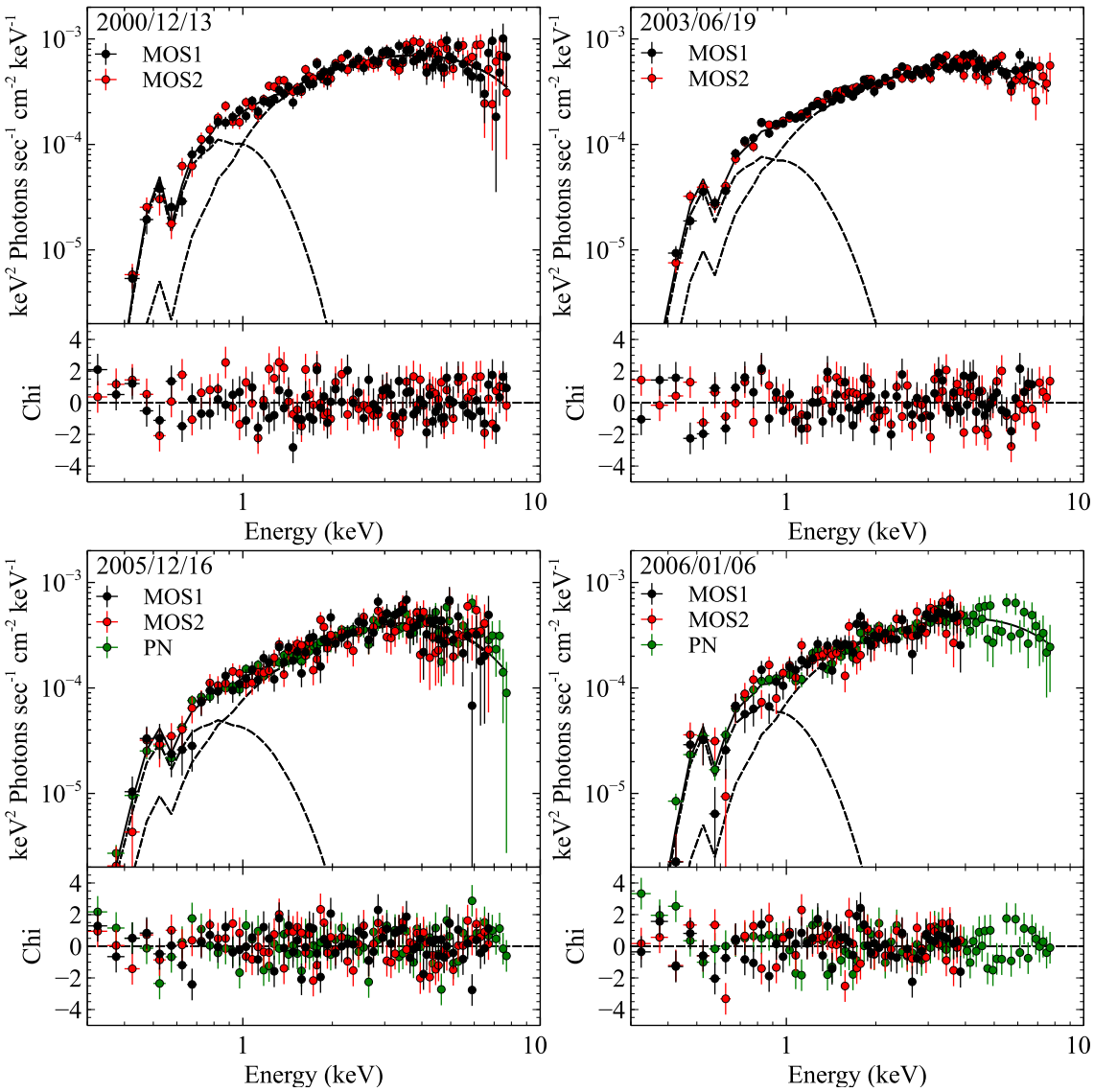

Figure 5.29. Spectra of NGC253ULX1 fitted and deconvolved with the MCD+THC model (top panels) and their residuals (bottom panels). The contributions of the MCD and THC components are drawn with the spectra in dashed lines.

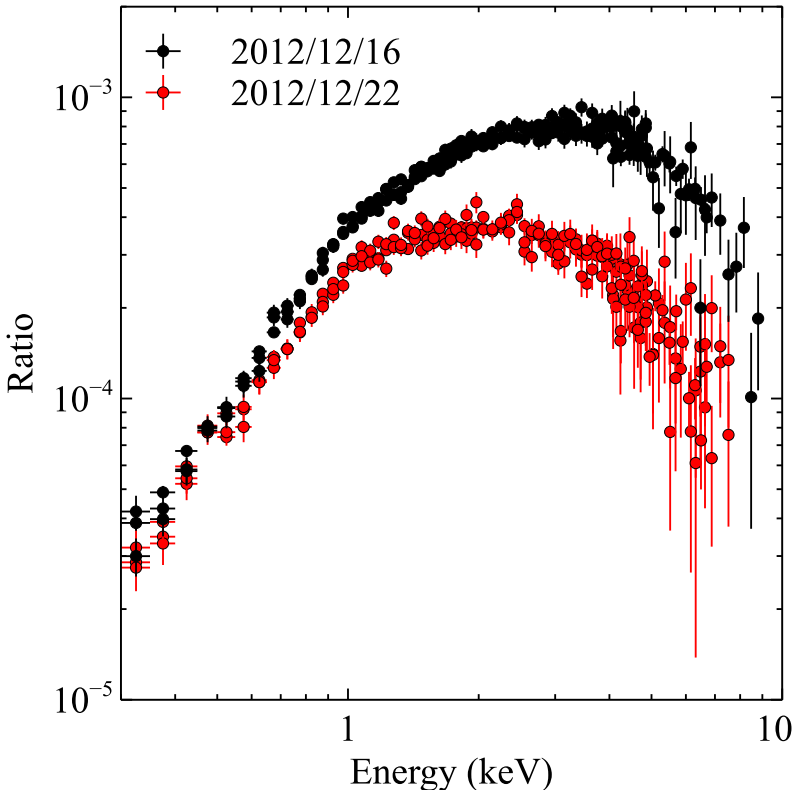

Figure 5.30. Ratios between the X-ray spectra of NGC 1313 X-2 and a response-folded PL model with $\Gamma = 2$.

Table 5.9: Parameters obtained from the spectral fitting in NGC 1313 X-2.

Date[a] YY/MM/HH	N_H[b]	T_e (keV)	Γ	τ[c]	T_{in} (keV)	R_{raw}[d]	R_{tot}[e]	L_{disk}[f]	L_X[g]	χ^2/ν (ν)
XMM-Newton+NuSTAR										
12/12/16	$1.7^{+0.3}_{-0.2}$	1.17 ± 0.05	$1.69^{+0.05}_{-0.08}$	21	$0.28^{+0.09}_{-0.06}$	$0.6^{+0.5}_{-0.2}$	1.3	1.3	4.8	1.16 (239)
12/12/22	$1.9^{+0.5}_{-0.3}$	1.07 ± 0.09	$2.02^{+0.08}_{-0.13}$	17	$0.21^{+0.08}_{-0.06}$	< 2.4	2.0	1.0	2.2	1.14 (229)

a: Date of the observation.

b: Intrinsic column density of equivalent Hydrogen in units of 10^{21} cm^{-2}.

c: Optical depth of the coronal electron cloud.

d: Apparent inner-disk radius of the un-scattered accretion disk component in units of 1000 km.

e: Inner-disk radius of the overall disk component in units of 1000 km.

f: Bolometric luminosity of the accretion disk component in units of 10^{39} erg sec^{-1}.

g: Absorbed $0.3 - 10$ keV band luminosity in units of 10^{39} erg sec^{-1}.

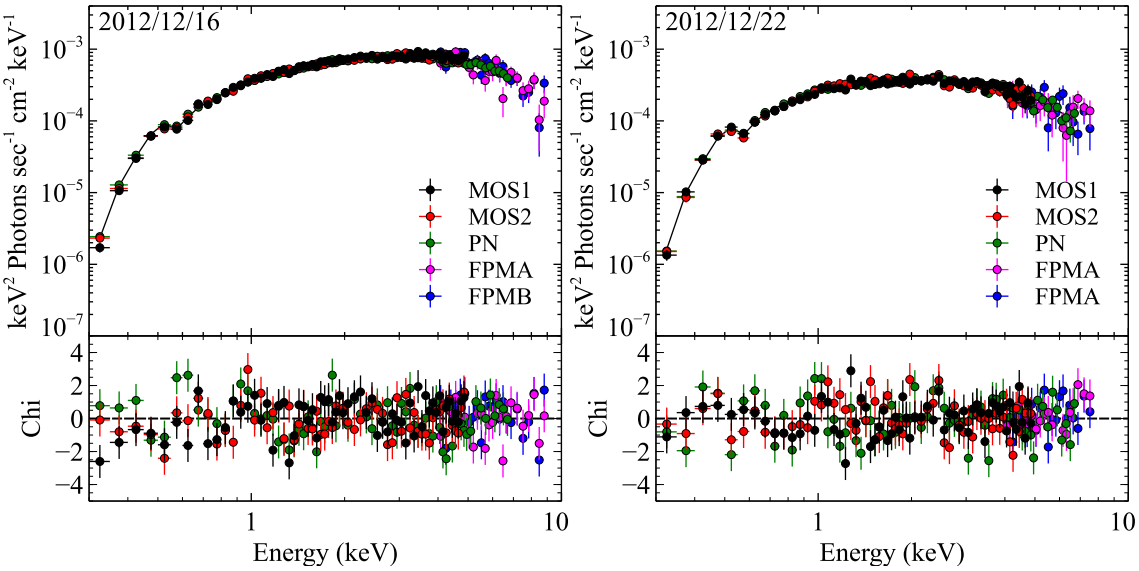

Figure 5.31. Spectra of NGC 1313 X-2 fitted and deconvolved with the MCD+THC model (top panels) and their residuals (bottom panels). The contributions of the MCD and THC components are drawn with the spectra in dashed lines.

6 Discussion

6.1 Summary of the Results

Employing the MCD+THC modeling, we fitted altogether 60 spectra from the 10 ULXs, typically in the 0.3–10 keV range, and up to $\sim$ 20 keV when the *NuSTAR* data sets are available. The model has given acceptable fits to all the spectra, regardless of the complex spectral changes seen in many sources. Based on this success, we regard the MCD+THC modeling as physically meaningful, rather than as merely empirically representing the spectra. The MCD component, with the innermost disk temperatures of $T_{\rm in} = 0.2 - 0.6$ keV, explained the softest end of the spectra, and supplied seed photons to the THC process. The THC component carried a major fraction of the spectrum above $\sim$ 1.5 keV, and its Comptonizing corona was in all cases found to be cool ($T_{\rm e} = 1.0 - 3$ keV) and optically thick ($\tau > 10$). The spectral changes of individual sources were mainly detected in > 1 keV, where the THC dominates, and some showed rather large changes in the THC spectral slope (e.g., NGC 1313 X-1; $1.7 \leq \Gamma \leq 2.3$).

As presented in figure 6.1, the absorption column density $N_{\rm H}$ was stable in all ULXs within a factors of three. In addition, their $N_{\rm H}$ was always less than 10^{22} cm^{-2} after separating out the Galactic line-of-sight contribution. Some showed even lower absorption as $N_{\rm H} < 10^{21}$ cm^{-2}. Furthermore, the values of $N_{\rm H}$ are not significantly correlated with $L_{\rm X}$, either in individual objects, or among the sample spectra as a whole.

Another important result is that the sample spectra were all confirmed to be quite featureless. Using a stacked high-quality *XMM-Newton* EPIC PN spectrum of Holmberg IX X-1, we searched for local spectral deviations from the MCD+THC continuum fit, including in particular narrow Fe-Kα lines. However, no Fe-K line features (either in emission or absorption) were found in the 4.0–8.5 keV range, beyond a 99%-confidence upper limit of $<$ 30 eV in equivalent width. We repeated the same analysis on other two representative ULXs, IC 342 X-1 and NGC 1313 X-1, which have similarly high statistics above Fe-K edge as Holmberg IX X-1. As shown in figure 6.2, these spectra required no Fe- K lines (either emission or absorption) either, and gave similarly stringent limits of -20 eV to 60 eV in IC 342 X-1, and -20 eV to 35 eV in NGC 1313 X-1, both in terms of the equivalent width.

6.2 Spectral Continua

6.2.1 Spectral state transitions and threshold luminosities

In figure 6.3, we present a series of typical spectra from 6 of the present ULX sample objects. To make their luminosities directly comparable, the figure ordinate has been converted to a unit of luminosity per decade, by assuming isotropic emission and utilizing the source distances given in

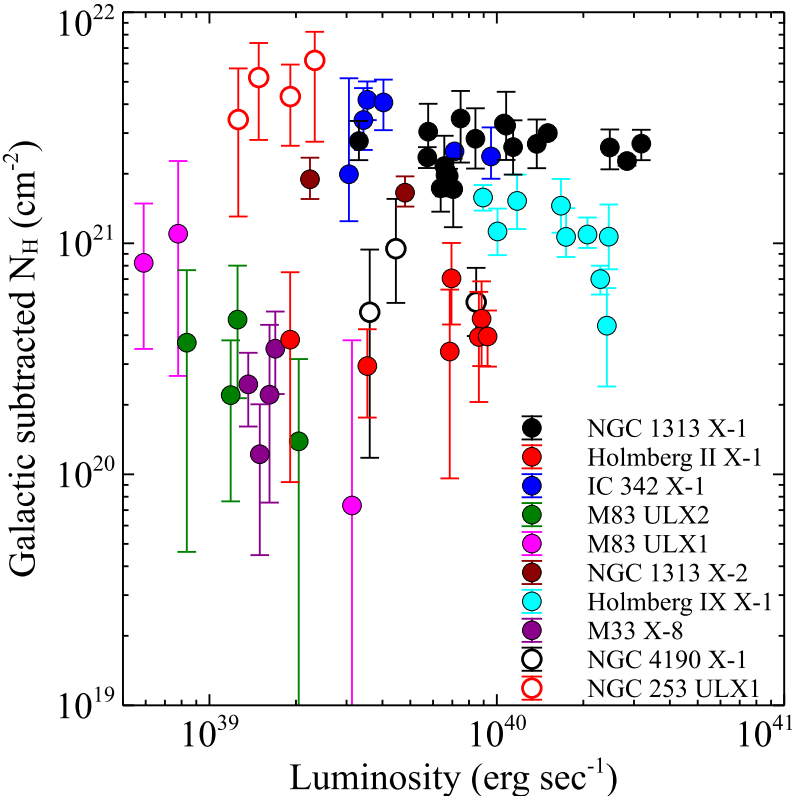

Figure 6.1. Correlation between L_X and N_H of all the sample spectra, where the Galactic line-of-sight contribution to N_H was removed.

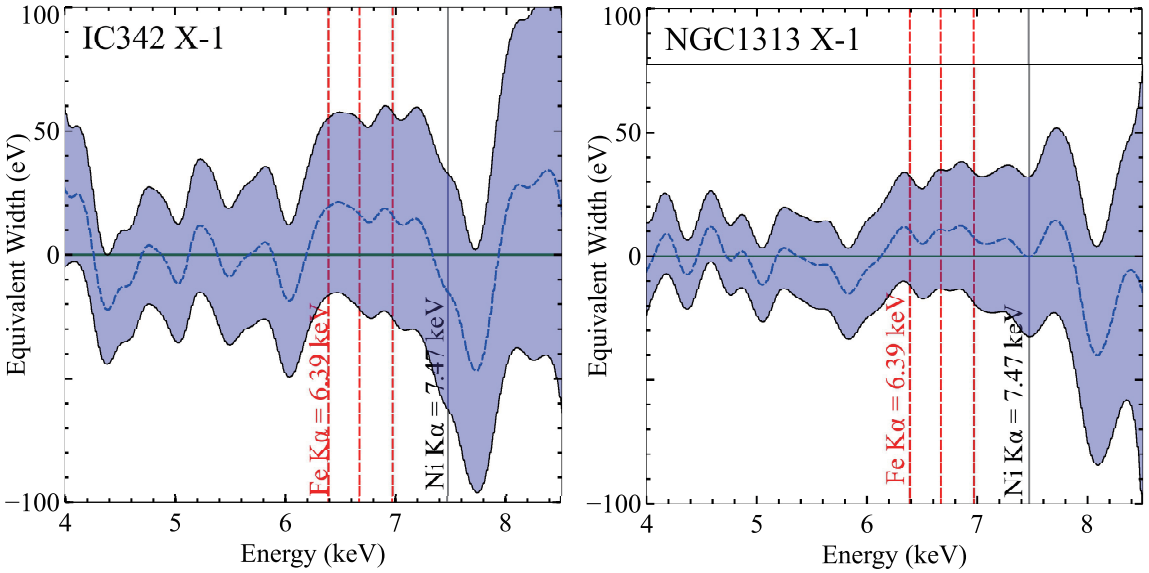

Figure 6.2. Allowed equivalent widths for narrow $\sigma = 10$ eV emission/absorption lines in NGC 1313 X-1 (right panel), and IC 342 X-1 (left panel).

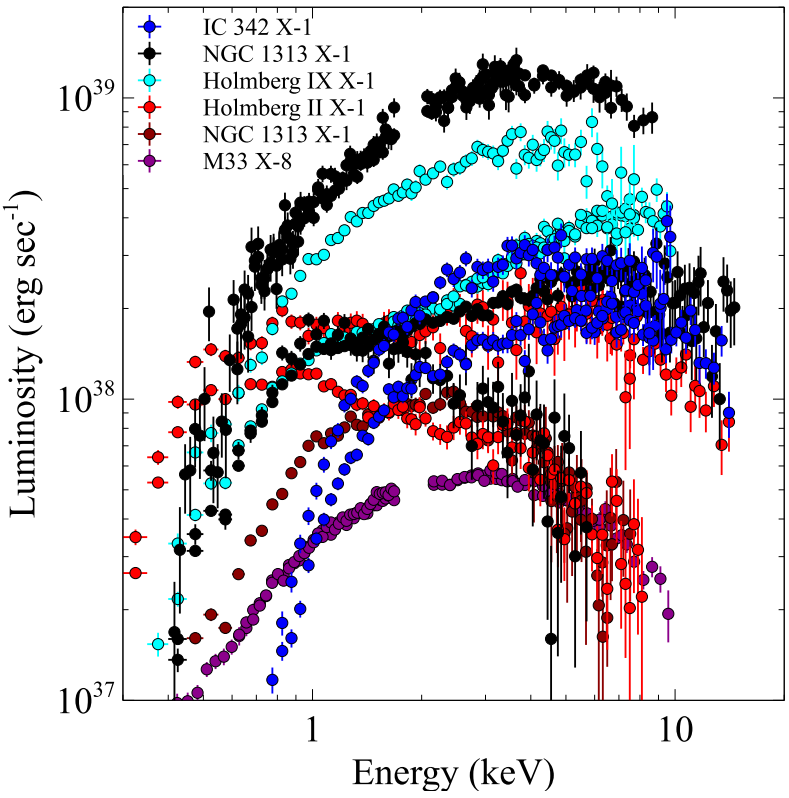

Figure 6.3. Spectra with representative shapes from 6 ULXs. Ordinate is in units of luminosity.

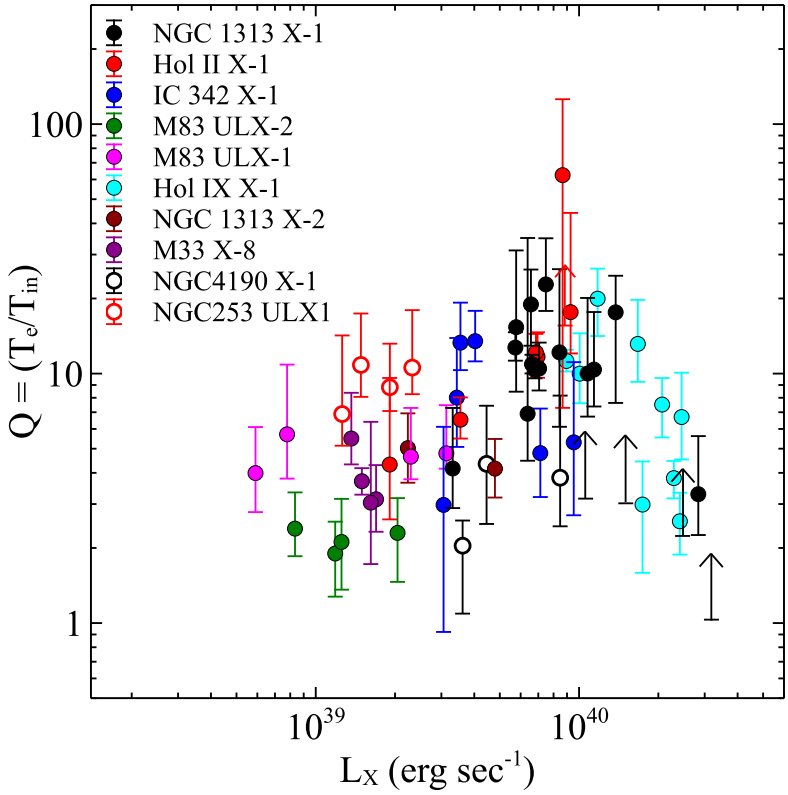

Figure 6.4. Correlation between L_X and Q for the sample spectra.

table 4.1. When figure 6.3 is examined for the behavior of individual objects, we find a common tendency (except in those sources which did not exhibit transitions) that the spectrum becomes more convex as the luminosity increases, and the system enters the Disk-like state. No object in our sample behaves in the opposite sense. However, when the same figure is examined as a whole, the spectral shape is not a simple single-valued function of the luminosity; in NGC 1313 X-2 and M33 X-8, for example, the Disk-like state is realized at a considerably *lower* luminosities than the PL state of IC 342 X-1 and NGC 1313 X-1. In other words, the Disk-like vs PL transition threshold luminosity, to be denoted $L_{\rm c}$, is seen to depend significantly on the objects, and scatter nearly by an order of magnitude within our sample.

Generally, BHBs are know to take, in the order of increasing luminosity, four characteristic spectral states; the Low/Hard state, the High/Soft state, the Very High state, and the Slim Disk state (section 2.1.2). The transition between adjacent states is considered to occur at a well-defined range in their Eddington ratio, $\eta \equiv L/L_{\rm edd}$. For example, the Low/Hard to High/Soft state transitions occur at $\eta \sim 0.1$, and those from the High/Soft to Very High states at $\eta \sim 0.3$ (Kubota and Makishima 2004). It is therefore natural to assume that the spectral transitions of ULXs also take place at a certain range of η. Then, the observed large scatter in the transition luminosity among the present sample suggests that their masses are widely spread.

6.2.2 Characterization of the spectral shapes

Since identifying the spectral state only by the apparent spectral shapes is sometimes ambiguous, we need to introduce a parameter that can more quantitatively discriminate the Disk-like and the PL states. For that purpose, we employ a parameter $Q \equiv T_{\rm e}/T_{\rm in}$, which represents the balance point between the radiative cooling and the Compton heating (Kobayashi et al. 2016). As shown by Makishima (2014), we generally find $Q > 10$ for "hot and thin" coronae in BHBs and LMXBs in their Low/Hard state, whereas $Q < 5$ for "cool and thick" coronae in their High/Soft state, as well as in the Very High state of BHBs.

Figure 6.4 shows a scatter plot of our ULX sample spectra, on the plane of the luminosity and the new parameter Q. Thus, the value of Q gradually increases with the luminosity, up to $Q > 10$, but suddenly drops to $Q = 3 - 5$ at the highest luminosity. This is because the Disk-like state spectra tend to exhibit higher $T_{\rm in}$ and slightly lower $T_{\rm e}$ than the PL-state ones, so that the two temperatures become closer to each other. This may be interpreted that the higher disk emissivity in the Disk-like state more efficiently cools the corona, thus bringing the disk and the corona physically closer. Thus, Q can be regarded as a good indicator of the point where a source makes spectral transitions from the PL state to the Disk-like states.

If we estimate the transition luminosity $L_{\rm c}$ again in the $L_{\rm X}$ vs Q plane, the highest is those of NGC 1313 X-1 and Holmberg IX X-1, $L_{\rm c} = (2-3) \times 10^{40}$ erg sec^{-1}. On the other hand, the lowest $L_{\rm c}$ among the sample should be $< 1.5 \times 10^{39}$ erg sec^{-1} of M33 X-8, because it has never been observed in the PL state. Thus, the values of $L_{\rm c}$ among the ULX sample have a range of nearly an order of magnitude. As already mentioned in the previous subsection, and employed partially by Mizuno et al. (2007), this wide scatter in $L_{\rm c}$ is considered to reflect similar scatter in the ULX mass among the sample. If we assume that M33 X-8 has a mass of $\sim 10\ M_\odot$, the maximum ULX mass among the sample (of NGC 1313 X-1 and Holmberg IX X-1) will reach 100 $M_\odot$, which is in

the intermediate mass regime. Here, a point of particular importance is that the above argument holds regardless of the basic interpretation of ULXs, whether they are shining at super-Eddington luminosities or are sub-Eddington objects.

6.3 Estimation of the Mass of ULXs via Standard Accretion Disk Physics

In this section, we estimate the masses of the ULXs from a method relying on physics of the standard accretion disk. Since we derived the overall inner-disk radius $R_{\rm tot}$ by utilizing 5.3 in the individual ULXs, we are able to estimate their mass from equation 2.6 by assuming that the obtained $R_{\rm tot}$ values are equivalent to their ISCOs. Before doing that we need to examine whether such solid radii are present in our ULX sample.

Figure 6.5 presents correlations between $T_{\rm in}$ and $R_{\rm tot}$ for all ULX data sets analyzed in the present thesis. Thus, $R_{\rm tot}$ and $T_{\rm in}$ are negatively correlated, indicating that the inner-disk radius is variable in the ULXs. According to equation 2.2, if $R_{\rm in}$ was changed with constant mass accretion rate $\dot{m}$, then $R_{\rm tot}$ should follow a function of $R_{\rm tot} \propto T_{\rm in}^{-3/4}$, which is presented in dashed lines in figure 6.5. The upper most line and the one in the middle represent ones with 1000 times and 100 times the mass accretion rate of that in the lower most one, respectively. Except for the data points of NGC 1313 X-1 around $T_{\rm in} = 0.18 - 2.0$ keV, they are roughly aligned on the relation, which can be interpreted that the inner-disk radius shrunk toward the central objects with $\dot{m}$ unchanged.

Although this varying $R_{\rm in}$ seems unnatural from the prospects of ISCO, such changes in $R_{\rm in}$ are widely seen in the Galactic BHBs. For example, the accretion disk of Cyg X-1 in the Low/Hard state is known to be truncated at ~ 2 times further out its ISCO (Makishima et al. 2008). As the source increases its mass accretion rate toward the High/Soft state, $R_{\rm in}$ gets smaller and eventually becomes identical to its ISCO. If the central BH increases its mass accretion rate even further, the spectral shape shifts to the Very High state, in which the disk is again truncated at further out its ISCO (e.g., $1.3 - 2.2$ times the ISCO in GX 339-4; Tamura et al. 2012). Therefore, we are allowed to interpret this negative correlation seen in the ULXs as signs that the disks in the ULXs are similarly truncated at particular radii, and the $R_{\rm in}$ moved toward the ISCO as they shifted their spectral states.

Since $R_{\rm in}$ is variable, we cannot determine which radii correspond to ISCOs of the ULXs. However, their minimum values may be utilized for estimating upper limits to the masses of the ULXs. The estimated upper limits are summarized in table 6.1. Since there is no reasonable evidence that BHs in ULXs are all Schwarzschild BHs, we also derived upper limits assuming Kerr BHs with a specific amount of spin. Although, we do not have any clear measurements of BH spin in ULXs or any other BHBs, gravitational event GW150914 gave an good reference. According to Abbot et al. (2016), the BH generated in GW150914 is estimated to have final spin value of $0.67^{+0.05}_{-0.07}$. If we assume that the BHs in ULXs have similar amount of spin, then the ISCO can get closer down to $\sim 1.5 R_{\rm S}$ ($\alpha = 1/2$ in equation 2.6). Hence, we derived two upper limits on ULXs mass, those assuming Schwarzschild BHs ($\alpha = 1$) and those assuming Kerr BHs with a spin of ~ 0.67 ($\alpha \sim 1/2$).

Although the result indicates that some ULXs favor to harbor BHs with relatively closer to the

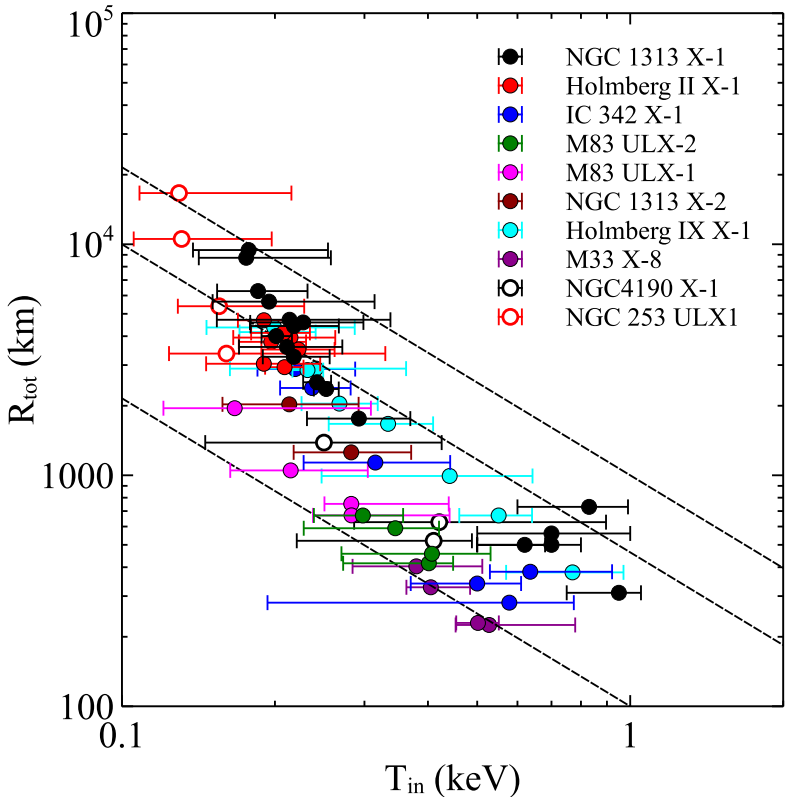

Figure 6.5. Correlation between T_{in} and R_{tot}. Dashed line represent relations of R_{tot} with constant mass accretion rate. The upper two lines have 100, 1000 times higher mass accretion rate than the lowest one.

Table 6.1: Estimated upper limit on mass for each ULX in the present thesis.

Object	$\alpha = 1$	$\alpha = 1/2$
Holmberg IX X-1	$\leq 50\ M_\odot$	$\leq 100\ M_\odot$
Holmberg II X-1	$\leq 340\ M_\odot$	$\leq 680\ M_\odot$
IC 342 X-1	$\leq 30\ M_\odot$	$\leq 60\ M_\odot$
NGC 1313 X-1	$\leq 30\ M_\odot$	$\leq 60\ M_\odot$
NGC 1313 X-2	$\leq 120\ M_\odot$	$\leq 240\ M_\odot$
M83 ULX1	$\leq 70\ M_\odot$	$\leq 140\ M_\odot$
M83 ULX2	$\leq 50\ M_\odot$	$\leq 100\ M_\odot$
M33 X-8	$\leq 30\ M_\odot$	$\leq 60\ M_\odot$
NGC 4190 X-1	$\leq 50\ M_\odot$	$\leq 100\ M_\odot$
NGC 253 ULX1	$\leq 340\ M_\odot$	$\leq 380\ M_\odot$

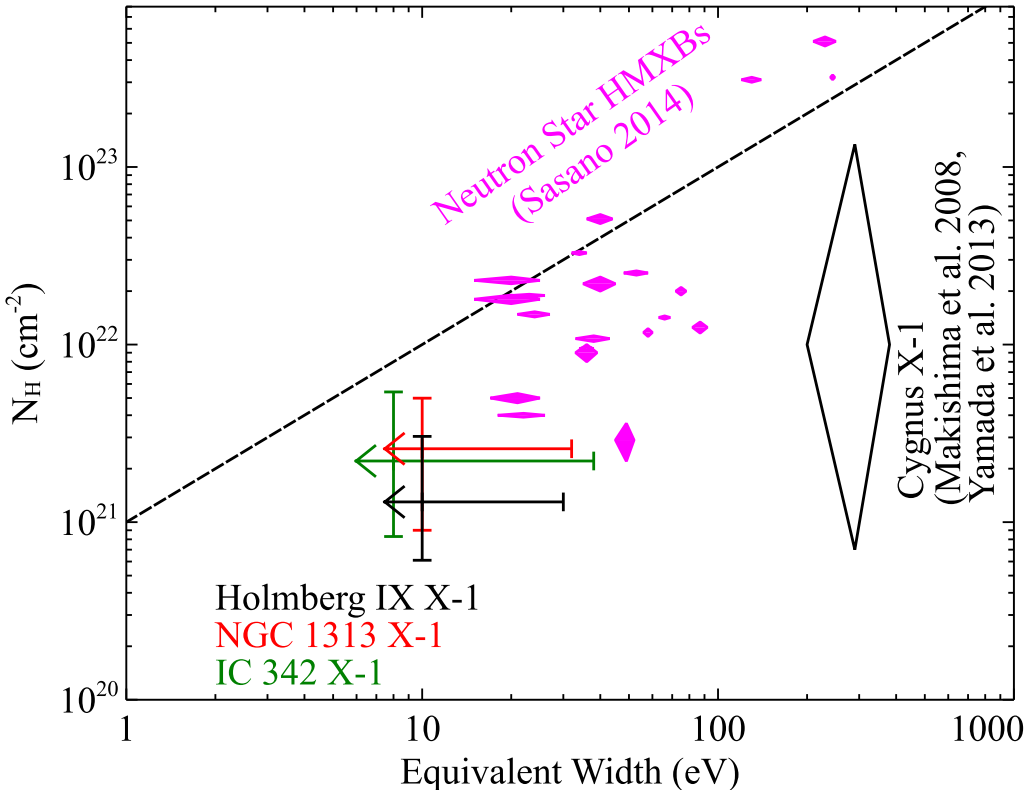

Figure 6.6. Correlation between $N_{\rm H}$ (Galactic contribution removed) and the equivalent width of Iron Kα emission line. Values for Galactic HMXB are plotted with diamond markers (Sasano 2014, Makishima et al. 2008, Yamada et al. 2013), while those of ULXs are plotted with error bars and arrows. Dashed line represents expected line equivalent width from a spherically isotropic gas with a column density $N_{\rm H}$ (Inoue 1985).

stellar mass (e.g., IC 342 X-1; $\leq 30\ M_\odot$), if we allow BHs to have as high spin as the one generated in GW150914, they still reside in the regime of intermediate or slightly massive BHs.

6.4 Absence of Spectral Features

Including Cyg X-1 (subsection 2.1.1), Galactic X-ray binary systems with relatively massive ($>$ 10 $M_\odot$) companion stars are called High Mass X-ray Binaries (HMXBs), in which the massive stars supply matters to the central compact objects (stellar mass BHs or neutron stars). In order to explain their persistent high luminosities, ULXs are often considered as HMXBs with considerably high mass accretion rates. In fact, recent observations indicate that some ULXs possibly have massive B-type companions (e.g., Motch et al. 2014).

Figure 6.6 shows a scatter plot between $N_{\rm H}$ and the equivalent width of Iron Kα lines, in several Galactic HMXBs and three ULXs from the present sample. Massive stars are generally known to launch strong stellar winds with a typical velocity of $\sim$ 2000 km sec^{-1}. Although some fraction of the wind materials are captured by the compact objects, the rest escape the binaries. These ejected matters inevitably interrupt the X-rays from the central emission regions, and give photoelectric absorptions with high equivalent Hydrogen column densities of $N_{\rm H} = 10^{22-24}$ cm^{-2}. In addition, stellar winds and the photosphere of the companion stars also give rise to strong fluorescence

lines, especially the Kα emission line from iron in the spectra of Galactic HMXBs. Thus, as shown in figure 6.6, the Galactic HMXBs usually show both high absorptions and strong fluorescence lines. Furthermore, variations in the stellar winds cause both $N_{\rm H}$ and the Iron Kα equivalent width to vary, as indicated by diamonds in figure 6.6.

In contrast, ULXs do not show strong spectral absorption; their $N_{\rm H}$ values were always less than 10^{22} cm^{-2}, and sometimes even lower as $N_{\rm H} < 10^{21}$ cm^{-2}. These values are an order of magnitude lower than those of the HMXBs. In addition, the values of $N_{\rm H}$ were stable in all ULXs within a factors of three, without particular correlation with $L_{\rm X}$. The Iron Kα lines were also absent, with upper limits of $30 - 40$ eV in terms of the equivalent width. As a result, ULXs are distributed in figure 6.1 in a distinct region from the other HMXBs.

According to computational simulations of super-critical accretion flows, optically-thick outflows are launched from the accretion disks due to the strong radiation pressure (Kawashima et al 2012). Like the stellar winds, such outflows are also expected to produce strong reprocessing features such us absorption, fluorescence emission lines, and absorption edges. In fact, the Narrow Line Seyfert 1 galaxy 1H 0707$-$495, considered to be accreting at a high rate, exhibits strong blue shifted Iron-K absorption lines in its spectrum (Hagino et al. 2016). Thus, the featureless ULX spectra strongly argues against the presence of such massive outflows, and of massive companions.

One possible explanation to the above puzzles is that the materials surrounding ULXs are completely ionized due to their strong X-ray illumination under super-critical accretion. However, as previously described in Kobayashi et al. (2017), accretion flows onto BHs with higher mass accretion rates tend to be less ionized, because smaller and smaller fractions of the accreting matters will actually be converted into radiation, thus leaving the subsequent accretion flows less ionized. Thus, the super-critical accretion scenario has a larger difficulty in explaining the observed featureless spectra, compared to more ordinary sub-critical accretion scenarios. These results urge us to cast doubt to the generally accepted view, that ULXs are accreting from massive companions.

6.5 Possible Interpretation of ULXs

From the discussion made in the previous sections, the conditions for the possible accretion geometry that can explain the observational facts are as follows,

- In order to generate the observed luminosities $L_{\rm X} \sim 10^{39-40}$ erg sec^{-1}, the sources have large mass accretion rates.
- The masses of the compact objects have at least an order of magnitude in range.
- Surrounding matters are efficiently accreted onto central objects, leaving less materials which can account for any kind of reprocessing features.

Especially from the third condition, since strong reprocessing features are inevitable as long as we allow massive companion stars to be present, we consider an alternative system that requires no companion star as an possible candidate to explain the ULXs.

If a BH with mass $M_{\rm BH}$ enters a dense gas region with mass density of ρ, with relative velocity of v, the BH accretes matter via Bondi-Hoyle-Lyttleton accretion. It accretes matters within a spherical region with a specific radius namely a Bondi radius $R_{\rm b}$, which is a distance represents

where the gravitational pull from the BH and kinetic energies of matters balance. In short, it is the maximum radius that the BH can capture the matters, and it can be written as,

$$R_{\rm b} = \frac{2GM_{\rm BH}}{v^2} \ , \tag{6.1}$$

where G is the gravitational constant. Accordingly, the mass accretion rate in this system $\dot{M}$ can be obtained by combining these $R_{\rm b}$, v, and ρ as

$$\dot{M} = \rho\pi R_{\rm b}^2 v = \frac{4\pi G^2 M_{\rm BH}^2 \rho}{v^3} \ . \tag{6.2}$$

If the energy is released as radiation with an efficiency of η, then the luminosity can be written by using equation 6.2 as,

$$L = \eta \dot{M} c^2 = \frac{4\pi G^2 M_{\rm BH}^2 c^2 \eta \rho}{v^3} \ , \tag{6.3}$$

where c is the light velocity. If we scale the respective parameters as, $M_2 \equiv M_{\rm BH}/(100\ M_\odot)$, $n = \rho/\mu m_{\rm p}$, $\mu = 0.13$, $n_2 \equiv n/(100\ {\rm cm}^{-3})$, $v_1 \equiv v/(10\ {\rm km\ sec}^{-1})$, where μ, $m_{\rm p}$ and n are mean molecular weight, proton mass, and number density of the gas region, respectively, equation 6.3 can be rewritten as

$$L = 4 \times 10^{37} M_2^2 n_2 v_1^{-3} {\rm erg\ sec}^{-1} \tag{6.4}$$

(Mii and Totani 2005). Here, we assumed the radiation efficiency as $\sim 10\%$, which is an expected value for a Bondi-Hoyle-Lyttleton accretion. Thus, the luminosity from Bondi-Hoyle-Lyttleton accretion is sensitive to BH mass ($\propto M_{\rm BH}^2$), which means that heavier BHs are favored to explain the high luminosities of ULXs under similar gas and velocity conditions.

After Nakamura et al. (2016), let us assume that an intermediate mass BH with a mass of $M_{\rm BH} = 100\ M_\odot$ enters a dense and cold gas region with a typical number density of $n = 100$, with a relatively low velocity of $v = 1$ km sec^{-1}. Then the luminosity calculated with equation 6.4 reaches the ULX regime of $L = 10^{40}$ erg sec^{-1}. Furthermore, if we assume a typical size for the dense gas region, $\sim$ a few pc, then the column density through the gas region is of the order of 10^{21} cm^{-2}. If furthermore the gas region is spherical and uniform, the expected equivalent width of the Fe-Kα line arising from the gas region becomes, from figure 6.1, a few eV, which is consistent with the observational result obtained in ULXs (figure 6.1 and figure 6.6). However, it is still unknown whether the emission lines from the accreting matters within the Bondi radius can be as weak as observed. Since we have very poor knowledge on the actual emissions from BH systems powered by Bondi-Hoyle-Lyttleton accretion, theoretical modeling of the expected Fe-K line within the Bondi radius is difficult. Instead, we may draw an analogy from observational results of those systems which are as similar as possible to what we are considering here.

Be binaries are HMXB systems with Be-type companion stars. Since they usually show X-ray outbursts synchronized with their binary periods, it is considered that the Be primary stars have circumstellar disks around them, and the compact objects (usually magnetized neutron stars) accrete matters via Bondi-Hoyle-Lyttleton accretion only when they enter these circumstellar disks of their companions. The largest difference from the other HMXBs is that these Be stars lack dense stellar winds, and hence the wind-capture accretion does not take place in these systems. Because of this, as a matter of fact, Fe-Kα lines in Be binaries are weaker, a few tens eV, than those in the other HMXBs, and the observed $N_{\rm H}$ is smaller as well. Although the central objects are not BHs, these Be binaries can be used as a good test case.

The Fe-K line from a Be binary is a sum of two contributions; fluorescence from the Be envelope, and that from the accretion stream from the Bondi radius to the neutron star. Since we want to know the latter, let us theoretically estimate the former, and subtract from the observations. Silaj et al. (2010) and Takagi (2013) reported that the circumstellar disks of Be HMXBs have a typical density of $\sim 10^{-14}$ g cm^{-3}, with radius of $\sim 10R^*$ and thickness of $\sim (1-4)R^*$, where R^* is the radius of the Be star which is typically $10R_\odot \sim 7 \times 10^{11}$ cm. For simplicity, let us assume that the circumstellar disk is roughly flat and has a thickness of $\sim 3R^*$, and the compact object is at the disk center during an outburst. As a result, the fluorescence Fe-K line from the irradiated circumstellar disk has been calculated to be ~ 10 eV, which accounts for $1/2-1/3$ of the observed line strengths. Thus, the emission lines from the region closest to the compact object, namely the remainders are expected to be $\sim 10-20$ eV in the equivalent width. Supposing the same conditions to ULXs, the expected equivalent width is < 30 eV; a few eV from the assumed gas region, and < 20 eV from the innermost accretion flows. This is consistent with the present observational results.

Although the presence of massive and isolated BHs were not known, the gravitational wave event GW150914 detected with LIGO (section 2.1.1) has clearly proved that BHs heavier ($\sim 60\ M_\odot$) than the stellar mass really exist (Abbot et al. 2016), and presumably they are more abundant in the universe than we have expected. In addition, a resent radio observation revealed that one molecular cloud of near our Galactic center shows evidence of large velocity dispersion inside it, which can be interpreted as a trace of disruption by a passage of a massive BH with a mass of $\sim 10^5\ M_\odot$ (e.g., Oka et al. 2016). From all these considerations, we suggest a possibility that ULXs are intermediate mass BHs, with an order of magnitude of range in their mass distribution ($\sim$ 100-$-$ 1000 $M_\odot$), shining at sub-Eddington regime by accreting via Bondi-Hoyle-Lyttleton accretion as they drift into region of relatively high inter-stellar gas density. This scenario is also consistent with the fact that ULXs are found preferentially in regions with high star formation rates.

7 Conclusion

In the present thesis, we analyzed 60 spectra of 10 luminous ULXs in nearby (< 5 Mpc) galaxies. The results of our work can be summarized as follows.

1. Regardless of their spectral state, the X-ray spectra of ULXs were successfully reproduced by a combination of multi-color disk component and its thermal Comptonization. All of them required cool and thick coronae ($T_{\rm e} = 1.0 - 3.0$ keV, $\tau > 10$), while the inner disk temperature showed positive correlation with their luminosity ($T_{\rm in} = 0.15 - 0.9$ keV).
2. Although the spectra above ~ 1.5 keV were often variable, these below 1 keV were relatively constant, indicating low and stable absorption column densities with $N_{\rm H} < 5 \times 10^{21}$ cm^{-2}.
3. The spectra did not bear any local features that deviate from the continuum model. Around the energy where Iron Kα lines are expected the allowed equivalent widths of narrow emission/absorption lines were less than 50 eV at 99% confidence level.
4. The temperature ratio $Q \equiv T_{\rm e}/T_{\rm in}$ successfully indicates whether the spectrum is in the Disk-like state or in the PL state. The critical luminosity where the spectral transition occurs scattered nearly an order of magnitude among the ULX sample, which suggests that ULXs have similarly large scatter in their masses. This argues against their interpretation as stellar mass (e.g., $5 - 20\ M_{\odot}$) BHs under super-critical accretion.
5. Compared to other Galactic accretion X-ray binary systems with high mass companions, the ULX spectra are amazingly featureless. Also, their spectra are only weakly absorbed, without strong variations in $N_{\rm H}$. The featureless spectra cannot be attributed to photoionization.
6. Combining the observational facts altogether, as an possible solution, ULXs could be interpreted as intermediate mass BHs with an order of magnitude range in their mass, fed by dense interstellar medium region via Bondi-Hoyle-Lyttleton accretions, instead of accreting matters from massive companion stars.

Acknowledgement

First of all, I would like to express my best gratitude to Prof. Kazuo Makishima and Ass. Prof. Kazuhiro Nakazawa. Prof. Makishima gave me precious advices on the entire thesis, even after he retired the university of Tokyo and moved to RIKEN. He also taught me the fundamental way of thinking as an experimental astrophysicist, which will surely be a guid line in my entire life. His passion and devotion to science were so astonishing that always made me realize that "I still have much to learn". Ass. Prof. Nakazawa, gave me a lot of helpful advices not only on writing this thesis but also on experiments with *Hitomi* Hard X-ray Imager (HXI). His powerful and motivated character always encouraged me, especially during the tough days in the vicinity of the lunch of *Hitomi*. I am very proud of this five years, working with such magnificent supervisors.

I would like to appreciate my colleague, Mr. Murakami. His overwhelming intelligence has always stimulated me and gave great feedbacks to my work. I was and will always be very proud to have such a brilliant person as a colleague. I would also like to thanks my seniors, Dr. Hirofumi Noda, Mr. Shunsuke Torii, Mr. Terukazu Nishida, Dr. Daigo Umemoto, and other present/previous members of the laboratory, Dr. Zhongly Zhang, Dr. Gu Liyi, Dr. Hideki Uchiyama, Mr. Katsuma Miyake, Mr. Ko Ono, Mr. Yuichi Kato, Mr. Yoshihiro Furuta, Miss Yuki Murota, Mr. Yuki Wada, Mr. Kazufumi Okuda, Mr. Hiromasa Suzuki, Miss Manami Seino. The joyful moments I shared with them are precious memories. Especially, I cannot help expressing my extra gratitude to those who worked together for *Hitomi* HXI. Although the satellite was sadly lost, the difficulties and hard working days that I went through with them are priceless experiences.

Finally, I would like to thanks my parents, little brother and sister, grand parents, and other relatives in Mexico and USA. This thesis would not be finished without their kind supports.

Bibliography

Abbot, B. P., et al. Observation of Gravitational Waves from a Binary Black Hole Merger. *Physical Review Letters*, 116, 061102, February 2016. doi: 10.1103/PhysRevLett.116.061102 url: http://journals.aps.org/prl/abstract/10.1103/PhysRevLett.116.061102

Aschenbach, B., In-orbit Performance of the *XMM-Newton* X-ray Telescopes: Images and Spectra, *Proceedings of SPIE*, 4496, January 2002. doi:10.1117/12.454367 url: http://proceedings.spiedigitallibrary.org/proceeding.aspx?articleid=894243

Bachetti, M., Vikram, R., Walton, D. J., Barret, D., Harrison, F. A., Boggs, S. E., Christensen, F. E., Graig, W. W., Fabian, A. C., Furst, F., Grefenstette, B. W., Hailey, C. J., Hornschemeier, A., Madsen, K. K., Miller, J. M., Ptak, A. F., Stern, D., Webb, N. A., & Zhang, W. W., The Ultraluminous X-ray Sources NGC 1313 X-1 and X-2: a Broadband Study with *NuSTAR* and *XMM-Newton*, *The Astrophysical Journal*, 778, 163, December 2013. doi: 10.1088/0004-637X/778/2/163 url: http://ads.nao.ac.jp/abs/2013ApJ...778..163B

Barré, H., Nye, H., & Janin, G., An Overview of the XMM Observatory System, *ESA bulletin 100*, December 1999. url: http://www.esa.int/esapub/bulletin/bullet100/BARRE.pdf

Bolton, C. T., Identification of Cygnus X-1 with HDE 226868, *Nature*, 235, 271, February 1972, doi: 10.1038/235271b0 url: http://ads.nao.ac.jp/abs/1972Natur.235..271B

Cseh, D., Kaaret, P., Corbel, S., Grisé, F., Lang, C., Körding, E., Falcke, H., Jonker, P. G., Miller-Jones, J. C. A., Farrell, S., Yang, Y. J., Paragi, Z., & Frey, S., Unveiling Recurrent Jets of the ULX Holmberg II X-1: Evidence for a Massive Stellar-Mass Black Hole?, *Monthly Notices of the Royal Astronomical Society*, 439, 1, March 2014. doi: 10.1093/mnrasl/slt166 url: http://ads.nao.ac.jp/abs/2014MNRAS.439L...1C

Dickey, J. M., & Lockman, F. J., HI in the Galaxy, *Annual Review of Astronomy and Astrophysics*, 28, 215, 1990. doi: 10.1146/annurev.aa.28.090190.001243 url: http://ads.nao.ac.jp/abs/1990ARA%26A..28..215D

Done, C., Gierlinski, M., & Kubota, A., Modelling the Behaviour of Accretion Flows in X-ray Binaries, *Astronomy and Astrophysics Review*, 15, 1D, December 2007. doi: 10.1007/s00159-007-0006-1 url: http://ads.nao.ac.jp/abs/2007A%26ARv..15....1D

Ezoe, Y., Naoko, I., Makishima, K., Study of the Long-Term X-Ray Variability of a Possible Quasar RX J0957.9+6903 with *ASCA*, *Publications of the Astronomical Society of Japan*, 53, 69, February 2001. doi: 10.1093/pasj/53.1.69 url: http://ads.nao.ac.jp/abs/2001PASJ...53..69E

Fabbiano, G., & Trinchieri, G., X-ray Observations of Spiral Galaxies. II. Images and Spectral Parameters of 13 Galaxies, *The Astrophysical Journal*, 315, 46, April 1987. doi: 10.1086/165113 url: http://adsabs.harvard.edu/abs/1987ApJ...315...46F

Giacconi, R., Gorenstein, P., Gursky, H., & Waters, J. R., An X-ray Survey of the Cygnus Region. *The Astrophysical Journal*, 148, L119, June 1967. doi:10.1086/180028 url: http://ads.nao.ac.jp/abs/1967ApJ...148L.119G

Gladstone, J. C., Roberts, T. P., & Done, C., The Ultraluminous State, *Monthly Notices of the Royal Astronomical Society*, 397, 1836, August 2009, doi: 10.1111/j.1365-2966.2009.15123.x url: http://ads.nao.ac.jp/abs/2009MNRAS.397.1836G

Hagino, K., Odaka, H., Done, C., Tomaru, R., Watanabe, S., & Takahashi, T., A Disc Wind Interpretation of the Strong Fe Kα Features in 1H 0707-495, *Monthly Notices of the Royal Astronomical Society*, 461, 3954, 3963, October 2016. doi: 10.1093/mnras/stw1579. url: http://ads.nao.ac.jp/abs/2016MNRAS.461.3954H

Harrison, F. A., Craig, W. W., Christensen, F. E., Hailey, C. J., Zhang, W. W., Boggs, S. E., Stern, D., Cook, W. R., Forster, K., Giommi, P., Grefenstette, B. W., Kim, Y., Kitaguchi, T., Koglin, J. E., Madsen, K. K., Mao, P. H., Miyasaka, H., Mori, K., Perri, M., Pivovaroff, M. J., Puccetti, S., Rana, V. R., Westergaard, N. J., Willis, J., Zoglauer, A., An, H., Bachetti, M., Barrière, N. M., Bellm, E. C., Bhalerao, V., Brejnholt, N. F., Fuerst, F., Liebe, C. C., Markwardt, C. B., Nynka, M., Vogel, J. K., Walton, D. J., Wik, D. R., Alexander, D. M., Cominsky, L. R., Hornschemeier, A. E., Hornstrup, A., Kaspi, V. M., Madejski, G. M., Matt, G., Molendi, S., Smith, D. M., Tomsick, J. A., Ajello, M., Ballantyne, D. R., Balokovìc, M., Barret, D., Bauer, F. E., Blandford, R. D., Niel Brandt, W., Brenneman, L. W., Chiang, J., Chakrabarty, D., Chenevez, J., Comastri, A., Dufour, F., Elvis, M., Fabian, A. C., Farrah, D., Fryer, C. L., Gotthelf, E. V., Grindlay, J. E., Helfand, D. J., Krivonos, R., Meier, D. L., Miller, J. M., Natalucci, L., Ogle, P., Ofek, E. O., Ptak, A., Reynolds, S. P., Rigby, J. R., Tagliaferri, G., Thorsett, S. E., Treister, E., & Urry, C. M., The Nuclear Spectroscopic Telescope Array (*NuSTAR*) High-Energy X-ray Mission, *The Astrophysical Journal*, 770, 103, June 2013. doi: 10.1088/0004-637X/770/2/103 url: http://ads.nao.ac.jp/abs/2013ApJ...770..103H

Heida, M., Torres, M. A. P., Jonker, P. G., Servillat, M., Repetto, S., Roberts, T. P., Walton, D. J., Moon D.-S., & Harrison, F. A., Discovery of a Red Supergiant Counterpart to RX J004722.4-252051, a ULX in NGC 253, *Monthly Notices of the Royal Astronomical Society*, 453, 3510, August 2015. doi:10.1093/mnras/stv1853 url: http://ads.nao.ac.jp/abs/2015MNRAS.453.3510H

Inoue, H., *Tenma* Observations of Bright Binary X-ray Sources, *Space Science Review*, 40, 317, 1985, doi: doi:10.1007/BF00212905, url: http://link.springer.com/article/10.1007/BF00212905

Isobe, N., Kubota, A., Sato, H., Mizuno, T., *Suzaku* Investigation into the Nature of the Nearest Ultraluminous X-ray Source, M33 X-8, *Publications of the Astronomical Society of Japan*, 64, 119, December 2012. doi: 10.1093/pasj/64.6.119 url: http://ads.nao.ac.jp/abs/2012PASJ...64..119I

Jansen, F., Lumb, D., Altieri, B., Clavel, J., Ehle, M., Erd, C., Gabriel, C., Guainazzi, M., Gondoin, P., Much, R., Munoz, R., Santos, M., Schartel, N., Texier, D., & Vacanti, G., *XMM-Newton* Observatory, *Astronomoy and Astrophysics*, 365, 1, October 2001. doi: 10.1051/0004-6361:20000036 url: http://ads.nao.ac.jp/abs/2001A%26A...365L...1J

Kawashima, T., Ohsuga, K., Mineshige, S., Yoshida, T., Heinzeller, D., & Matsumoto, R., Comptonized Photon Spectra of Supercritical Black Hole Accretion Flows with Applica-

tion to Ultraluminous X-ray Sources, *The Astrophysical Journal*, 752, 18, June 2012. doi: 10.1088/0004-637X/752/1/18 url: http://ads.nao.ac.jp/abs/2012ApJ...752...18K

Kitaguchi, T., Grefenstette, B. W., Harrison, F. A., Miyasaka, H., Bhalerao, V. B., Cook IIIa, W. R., Mao, P. H., Rana, V. R., Boggs, S. E., Zoglauer, A. C., Spectral Calibration and Modeling of the NuSTAR CdZnTe Pixel Detectors, *Proceedings of SPIE*, 8145, 2011. doi: 10.1117/12.896972 url: http://proceedings.spiedigitallibrary.org/proceeding.aspx?articleid=1342185

Kobayashi, S., Nakazawa, K., & Makishima, K., A New Characterization of the Compton Process in the ULX Spectra, *Astronomische Nachrichten*, 337, 479, 484, May 2016. doi: 10.1002/asna.201612333. url: http://ads.nao.ac.jp/abs/2016AN....337..479K

Kobayashi, S. B., Nakazawa, K., Makishima, K., *Suzaku* Observations of Spectra Variations of the Ultra-Luminous X-ray Source Holmberg IX X-1, *Publications of the Astronomical Society of Japan*, 69, 1, 4, February 2017. doi: 10.1093/pasj/psw108. url: http://ads.nao.ac.jp/doi/10.1093/pasj/psw108

Koyama, K., Tsunemi, T., Dotani, T., Bautz, M. W., Hayashida, K., Tsuru, T., Matsumoto, H., Ogawara, Y., Ricker, G. R., Doty, J., Kissel, S. E., Foster, R., Nakajima, N., Yamaguchi, H., Mori, H., Sakano, M., Hamaguchi, K., Nishiuchi, M., Miyata, E., Torii, K., Namiki, M., Katsuda, S., Matsuura, D., Miyauchi, T., Anabuki, N., Tawa, N., Ozaki, M., Murakami, H., Maeda, Y., Ichikawa, Y., Prigozhin, G. Y., Boughan, E. A., LaMarr, B., Miller, E. D., Burke, B. E., Gregory, J. A., Pillsbury, A., Bamba, A., Hiraga, J. S., Senda, A., Katayama, H., Kitamoto, S., Tsujimoto, M., Kohmura, T., Tsuboi, Y., & Awaki, H., X-ray Imaging Spectrometers (XIS) on Board *Suzaku*, *Publications of the Astronomical Society of Japan*, 59, 22, January 2007. doi: 10.1093/pasj/59.sp1.S23 url: http://adsabs.harvard.edu/abs/2007PASJ...59S..23K

Kubota, A., X-ray Study of Optically-thick Accretion Disks around Stellar Black Holes -The Standard Accretion Disk and Beyond-, *PhD thesis, the University of Tokyo*, December 2001. url: http://www-utheal.phys.s.u-tokyo.ac.jp/paper/pdfs/dron/2001_kubota.pdf

Kubota, A., Done, C., Makishima, K., Another Interpretation of the Power-Law-Type Spectrum of an Ultraluminous Compact X-ray Source in IC 342, *Monthly Notices of the Royal Astronomical Society*, 337, 11, December 2002. doi: 10.1046/j.1365-8711.2002.06043.x url: http://ads.nao.ac.jp/abs/2002MNRAS.337L..11K

Kubota, A., & Makishima, K., The Three Spectral Regimes Found in the Stellar Black Hole XTE J1550-564 in its High/Soft State, *The Astrophysical Journal*, 601, 428, 438, January 2004. doi: 10.1086/380433. url: http://ads.nao.ac.jp/abs/2004ApJ...601..428K

Luangtip, W., Roberts, T. P., & Done, C., The X-ray Spectral Evolution of the Ultraluminous X-ray Source Holmberg IX X-1, *Monthly Notices of the Royal Astronomical Society*, 460, 4417, 4432, May 2016. doi: 10.1093/mnras/stw1282 url: http://ads.nao.ac.jp/abs/2016MNRAS.460.4417L

Makishima, K., Maejima, Y., Mitsuda, K., Bradt, H. V., Remillard, R. A., Tuohy, I. R., Hoshi, R., & Nakagawa, M., Simultaneous X-ray and Optical Observations of GX 339-4 in an X-ray High State, *The Astrophysical Journal* 308, 635, 643, September 1986. doi:10.1086/164534 url: http://ads.nao.ac.jp/abs/1986ApJ...308..635M

Makishima, K., Kubota, A., Mizuno, Ohnishi, T., Tashiro, M., Aruga, Y., Asai, K., Dotani, T., Mitsuda, K., Ueda, Y., Uno, S., Yamaoka, Ebisawa, K., Kohmura, Y., & Okada, K., The Nature of Ultraluminous Compact X-ray Sources in Nearby Spiral Galxies, *The Astrophysical Journal*, 535, 632, 643, June 2000. doi: 10.1086/308868 url: http://ads.nao.ac.jp/abs/2000ApJ...535..632M

Makishima, K., Takahashi, H., Yamada, S., Done, C., Kubota, A., Dotani, T., Ebisawa, K., Itoh, T., Kitamoto, S., Negoro, H., Ueda, Y., & Yamaoka, K., *Suzaku* Results on Cygnus X-1 in the Low/Hard state, *Publications of the Astronomical Society of Japan*, 60, 585, 604, June 2008. doi: 10.1093/pasj/60.3.585 url: http://ads.nao.ac.jp/abs/2008PASJ...60..585M

Makishima, K., Zhang, Z., Noda, H., Torii, S., Sakurai, S., Kobayashi, S., Ono, K., Nakazawa, K., Sugizaki, M., Yamada, S., *Institute of Space and Astronautical Science Space Science Symposium*, January 2014. url: http://www.isas.jaxa.jp/j/researchers/symp/sss14/paper/P3-004.pdf

Middleton, M. J., Sutton, A. D., Roberts, T. P., X-ray Spectral Evolution in the Ultraluminous X-ray Source M33 X-8, *Monthly Notices of the Royal Astronomical Society*, 417, 464, October 2011. doi: 10.1111/j.1365-2966.2011.19285.x url: http://ads.nao.ac.jp/abs/2011MNRAS.417..464M

Mii, H., & Totani, T., Ultraluminous X-Ray Sources: Evidence for Very Efficient Formation of Population III Stars Contributing to the Cosmic Near-Infrared Background Excess?, *The Astrophysical Journal*, 628, 873, 878, August 2005. doi: 10.1086/430942. url: http://ads.nao.ac.jp/abs/2005ApJ...628..873M

Mineshige, S., & Ohsuga, K., Supercritical Accretion Flow?, *ASP Conference Series*, 373, October 2007. url: http://ads.nao.ac.jp/abs/2007ASPC..373...85M

Mitsuda, K., Inoue, H., Koyama, K., Makishima, K., Matsuoka, M., Ogawara, Y., Shibazaki, N., Suzuki, K., & Tanaka, Y., Energy Spectra of Low-Mass Binary X-ray Sources Observed from *Tenma*, *Publications of the Astronomical Society of Japan*, 36, 741, 759, 1984. ISSN 0004-6264. url: http://ads.nao.ac.jp/abs/1984PASJ...36..741M

Mitsuda, K., Bautz, M., Inoue, H., Kelley, R. L., Koyama, K., Kunieda, H., Makishima, K., Ogawara, Y., Petre, R., Takahashi, T., Tsunemi, H., White, N. E., Anabuki, N., Angelini, L., Arnaud, K., Awaki, H., Bamba, A., Boyce, K., Brown, G. V., Chan K. W., Cottam, J., Dotani, T., Doty, J., Ebisawa, K., Ezoe, Y., Fabian, A. C., Figueroa, E., Fujimoto, R., Fukazawa, Y., Furusho, T., Furuzawa, A., Gendreau, K., Griffiths, R. E., Haba, Y., Hamaguchi, K., Harrus, L., Hashinger, G., Hatsukade, I., Hayashida, K., Henry, P. J., Hiraga, J. S., Holt, S. S., Hornschemeier, A., Hughes, J. P., Hwang, U., Ishida, M., Ishisaki, Y., Isobe, N., Itoh, M., Iyomoto, N., Kahn, S. M., Kamae, T., Katagiri, H., Kataoka, J., Katayama, H., Kawai, N., Kilbourne, C., Kinugasa, K., Kissel, S., Kitamoto, S., Kohama, M., Kohmura, T., Kokubun, M., Kotani, T., Kotoku, J., Kubota, A., Madejski, G. M., Maeda, Y., Makino, F., Markowitz, A., Matsumoto, C., Matsumoto, H., Matsuoka, M., Matsushita, K., McCammon, D., Mihara, T., Misaki, K., Miyata, E., Mizuno, T., Mori, K., Mori, H., Morii, M., Moseley, H., Mukai, K., Murakami, H., Murakami, T., Mushotzky, R., Nagase, F., Namiki M., Negoro, H., Nakazawa, K., Nousek, J. A., Okajima, T., Ogasaka, Y., Ohashi, T., Oshima, T., Ota, N., Ozaki, M., Ozawa, H., Parmar, A. N., Pence, W. D., Porter, F. S., Reeves, J. N., Ricker,

G. R., Sakurai, I., Sanders, W. T., Senda, A., Serlemitsos, P., Shibata, R., Soong, Y., Smith, R., Suzuki, M., Szymkowiak, A. E., Takahashi, H., Tamagawa, T., Tamura, K., Tamura, T., Tanaka, Y., Tashiro, M., Tawara, Y., Terada, Y., Terashima, Y., Tomida, H., Torii, K., Tsuboi, Y., Tsujimoto, M., Tsuru, T., Turner, M. J. L., Ueda, Y., Ueno, S., Ueno, M., Uno, S., Urata, Y., Watanabe, S., Yamamoto, N., Yamaoka, K., Yamasaki, N. Y., Yamashita, K., Yamauchi, M., Yamauchi, S., Yaqoob, T., Yonetoku, & D., Yoshida A., The X-ray Observatory *Suzaku*, *Publications of the Astronomical Society of Japan*, 59, 1, January 2007. doi: 10.1093/pasj/59.sp1.S1 url: http://adsabs.harvard.edu/abs/2007PASJ...59S...1M

Miyawaki, R., Makishima, K., Yamada, S., Gandhi, P., Mizuno, T., Kubota, A., Tsuru, T. G., & Matsumoto, H., *Suzaku* Observation of M82 X-1: Detection of a Curved Hard X-ray Spectrum, *Publications of the Astronomical Society of Japan*, 61, 263, 278, January 2009. doi: 10.1093/pasj/61.sp1.S263 url: http://ads.nao.ac.jp/abs/2009PASJ...61S.263M

Mizuno, T., & Makishima, K., X-ray Observations of the Normal Spiral Galaxies with ASCA, *Advances in Space Research*, 25, 395, 2000. doi: 10.1016/S0273-1177(99)00766-8 url: http://ads.nao.ac.jp/abs/2000AdSpR..25..395M

Mizuno, T., Kubota, A., & Makishima, K., Spectral Variability of Ultraluminous Compact X-Ray Sources in Nearby Spiral Galaxies, *The Astrophysical Journal*, 554, 1282, June 2001. doi: 10.1086/321418 url: http://ads.nao.ac.jp/abs/2001ApJ...554.1282M

Mizuno, T., Miyawaki, R., Ebisawa, K., Kubota, A., Miyamoto, M., Winter, L. M., Ueda, Y., Isobe, N., Dewangan, G. C., Done, C., Griffiths, R. E., Haba, Y., Kokubun, M., Kotoku, J., Makishima, K., Matsushita, K., Mushotzky, R. F., Namiki, M., Petre, R., Takahashi, H., Tamagawa, T., & Terashima, Y., *Suzaku* Observation of Two Ultraluminous X-ray Sources in NGC 1313, *Publications of the Astronomical Society of Japan*, 59, 257, January 2007. doi: 10.1093/pasj/59.sp1.S257 url: http://ads.nao.ac.jp/abs/2007PASJ...59S.257M

Motch, C., Pakull, M. W., Soria, R., Grise, F., & Pietrzynski G., A Mass of Less Than 15 Solar Masses for the Black Hole in an Ultraluminous X-ray Source, *Nature*, 514, 198, October 2014, doi: 10.1038/nature13730 url: http://ads.nao.ac.jp/abs/2014Natur.514..198M

Nakamura, T., Nakano, H., & Tanaka, T., Detecting Quasinormal Modes of Binary Black Hole Mergers with Second-Generation Gravitational-Wave Detectors, *Physical Review D*, 93, 044048, February 2016. doi: 10.1103/PhysRevD.93.044048. url: http://ads.nao.ac.jp/abs/2016PhRvD..93d4048N

Oka, T., Mizuno, R., Miura, K., & Takekawa, S., Signature of an Intermediate-Mass Black Hole in the Central Molecular Zone of our Galaxy, *The Astrophysical Journal Letters*, 816, 7, January 2016. doi: 10.3847/2041-8205/816/1/L7. url: http://ads.nao.ac.jp/abs/2016ApJ...816L...7O

Oda, M., Gorenstein, P., Gursky, H., Kellogg, E., Schreier, E., Tananbaum, H., & Giacconi, R., X-ray Pulsations from Cygnus X-1 Observed from *Uhuru*. *The Astrophysical Journal*, 166, L1, May 1971. doi: 10.1086/180726 url: http://ads.nao.ac.jp/abs/1971ApJ...166L...1O

Pinto, C., Middleton, M. J., & Fabian, A. C., Resolved Atomic Lines Reveal Outflows in Two Ultraluminous X-ray Sources, *Nature*, 17417, 2016. doi: 10.1038/nature17417 url: http://ads.nao.ac.jp/abs/2016Natur.533...64P

Rana, V., Harrison, F. A., Bachetti, M., Walton, D. J., Furst, F., Barret, D., Miller, J. M., Fabian, A. C., Boggs, S. E., Christensen, F. C., Craig, W. W., Grefenstette, B. W., Hailey, C. J., Madsen, K. K., Ptak, A. F., Stern, D., Webb, N. A., & Zhang, W. W., The Broadband *XMM-Newton* and *NuSTAR* X-ray Spectra of two Ultraluminous X-ray Sources in the Galaxy IC 342, *The Astrophysical Journal*, 799, 121, February 2015. doi: 10.1088/0004-637X/799/2/121 url: http://ads.nao.ac.jp/abs/2015ApJ...799..121R

Sasano, M., X-ray Studies of Highly Magnetized Neutron Stars in Binary Systems with *Suzaku*, *PhD thesis, the University of Tokyo*, December 2014. url: http://hdl.handle.net/2261/60178

Serlemitsos, P. J., Soong, Y., Chan, K. W., Okajima, T., Lehan, J. P., Maeda, Y., Itoh, K., Mori, H., Iizuka, R., Itoh, A., Inoue, H., Okada, S., Yokoyama, Y., Itoh, Y., Ebara, M., Nakamura, R., Suzuki, K., Ishida, M., Hayakawa, A., Inoue, C., Okuma, S., Kubota, R., Suzuki, M., Osawa, T., Yamashita, K., Kunieda, H., Tawara, Y., Ogasaka, Y., Furuzawa, A., Tamura, K., Shibata, R., Haba, Y., Naitou, M., & Misaki, K., The X-ray Telescope onboard *Suzaku*, *Publications of the Astronomical Society of Japan*, 59, 9, January 2007. doi: 10.1093/pasj/59.sp1.S9 url: http://adsabs.harvard.edu/abs/2007PASJ...59S...9S

Shakura, N. I., & Sunyaev, R. A., Black Holes in Binary Systems: Observational Appearances, *Astronomy and Astrophysics*, 24, 1337, 1973. url: http://ads.nao.ac.jp/abs/1973A%26A...24..337S

Silaj, J., Jones, C. E., Tycner, C., Sigut, T. A. A., & Smith, A. D., A Systematic Study of Hα Profiles of Be Stars, *The Astrophysical Journal Supplement*, 187, 1, 228, March 2010. doi: 10.1088/0067-0049/187/1/228 url: http://ads.nao.ac.jp/abs/2010ApJS..187..228S

Smith, M. J. S., *XMM-Newton* Calibration Technical Note XMM-SOC-CAL-TN-0018, September 2015, url: http://xmm2.esac.esa.int/docs/documents/CAL-TN-0018.pdf

Sugiho, M., Kotoku, J., Makishima, K., Kubota, A., Mizuno, T., Fukazawa, Y., & Tashiro, M., A Possible X-ray Periodicity at Several Tens of Hours of an Ultraluminous Compact X-ray Source in IC 342, *The Astrophysical Journal*, 561, 73, November 2001. doi: 10.1086/324456 url: http://ads.nao.ac.jp/abs/2001ApJ...561L..73S

Sunyaev, R., & Titarchuk, L. G., Comptonization of X-rays in Plasma Clouds - Typical Radiation Spectra, *Astronomy and Astrophysics*, 86, 121, June 1980. url: http://ads.nao.ac.jp/abs/1980A%26A....86..121S

Takagi, T., Master Thesis, *Nihon University*, 2013.

Takano, M., Mitsuda, K., Fukazawa, Y., & Nagase, F., Properties of M33 X-8, the Nuclear Source in the Nearby Spiral Galaxy, *The Astrophysical Journal*, 436, 47, November 1994. doi: 10.1086/187629 url: http://ads.nao.ac.jp/abs/1994ApJ...436L..47T

Tamura, M., Kubota, A., Yamada, S., Done, C., Kolehmainen, M., Ueda, Y., & Torii, S., The Truncated Disk from *Suzaku* Data of GX 339-4 in the Extreme Very High State, *The Astrophysical Journal*, 753, 65, July 2012. doi: 10.1088/0004-637X/753/1/65 url: http://ads.nao.ac.jp/abs/2012ApJ...753...65T

Tawa, N., et al., *The Astronomical Society Japan Annual Meeting*, September 2006, url: http://www.astro.isas.ac.jp/suzaku/news/2006/1016/asj0609_suzaku_xis_bgd.pdf

Tawa, N., Hayashida, K., Nagai, M., Nakamoto, H., & Tsunemi, H., Reproducibility of Non-X-Ray Background for the X-Ray Imaging Spectrometer aboard *Suzaku*, *Publications of the Astronomical Society of Japan*, 60, 11, February 2008. doi: 10.1093/pasj/60.sp1.S11 url: http://ads.nao.ac.jp/abs/2008PASJ...60S..11T

Tsunoda, N., Kubota, A., Namiki, M., Sugiho, M., Kawabata, K., & Makishima, K., Detailed Spectral Study of an Ultra-Luminous Compact X-ray Source M81 X-9 in the Disk Dominated State, *Publications of the Astronomical Society of Japan*, 58, 1081, December 2006. doi: 10.1093/pasj/58.6.1081 url: http://ads.nao.ac.jp/abs/2006PASJ...58.1081T

van Katwijk, K., van der Laan, T., & Stramaccioni, Mechanical and Thermal Design of XMM, *ESA bulletin 100*, December 1999.

Vierdayanti, K., Done, C., Roberts, T. P., & Mineshige, S., X-ray Spectral Variability in the Ultraluminous X-ray Source Holmberg IX X-1, *Monthly Notices of the Royal Astronomical Society*, 403, 1206, April 2010. doi: 10.1111/j.1365-2966.2009.16210.x url: http://ads.nao.ac.jp/abs/2010MNRAS.403.1206V

Walton, D. J., Roberts, T. P., Mateos, S., & Heard, V., 2XMM Ultraluminous X-ray Source Candidates in Nearby Galaxies, *Monthly Notices of the Royal Astronomical Society*, 416, 1844, May 2011, doi:10.1111/j.1365-2966.2011.19154.x url: http://ads.nao.ac.jp/abs/2011MNRAS.416.1844W

Walton, D. J., Miller, J. M., Harrison, F. A., Fabian, A. C., Roberts, T. P., Middleton, M. J., & Reis, R. C., X-ray Outflows and Super-Eddington Accretion in the Ultraluminous X-ray Source Holmberg IX X-1, *The Astrophysical Journal Letters*, 773, 9, August 2013. doi: 10.1088/2041-8205/773/1/L9 url: http://ads.nao.ac.jp/abs/2013ApJ...773L...9W

Watarai, K., Fukue, J., Takeuchi, M., Mineshige, S., Galactic Black-Hole Candidates Shining at the Eddington Luminosity, *Publications of the Astronomical Society of Japan*, 52, 133, February 2000. doi:10.1093/pasj/52.1.133 url: http://ads.nao.ac.jp/abs/2000PASJ...52..133W

Wilms, J., Allen, A., & McCray, R., On the Absorption of X-rays in the Interstellar Medium, *The Astrophysical Journal*, 542, 914, October 2000. doi: 10.1086/317016 url: http://ads.nao.ac.jp/abs/2000ApJ...542..914W

XMM-Newton User Handbook, section 3.3, European Photon Imaging Camera (EPIC), url:http://xmm-tools.cosmos.esa.int/external/xmm_user_support/documentation/uhb/epic.html

XMM-Newton User Handbook, section 3.3.7.2, EPIC internal quiescent background, url:https://xmm-tools.cosmos.esa.int/external/xmm_user_support/documentation/uhb/epicintbkgd.html#uhb:fig:sm5

Yamada, S., Negoro, H., Torii, S., Noda, H., Mineshige, S., & Makishima, K., Highly Ionized Fe-K Absorption Line from Cygnus X-1 in the High/Soft State Observed with *Suzaku*, *The Astrophysical Journal*, 767, 35, April 2013. doi: 10.1088/2041-8205/767/2/L35. url: http://ads.nao.ac.jp/abs/2013ApJ...767L..35Y

Yoshida, T., Isobe, N., Mineshige, S., Kubota, A., Mizuno, T., & Saitou, K., Two Power-Law States of the Ultraluminous X-ray Source IC 342 X-1, *Publications of the Astronomical Society of Japan*, 65, 48, April 2013. doi: 10.1093/pasj/65.2.48 url: http://ads.nao.ac.jp/abs/2013PASJ...65...48Y

Zdziarski, A. A., Johnson, W. N., & Magdziarz, P., Broad-band γ-ray and X-ray Spectra of NGC 4151 and Their Implication for Physical Processes and Geometry, *Monthly Notices of the Royal Astronomical Society*, 283, 193, November 1996, doi: 10.1093/mnras/283.1.193 url: http://ads.nao.ac.jp/abs/1996MNRAS.283..193Z

Życki, P. T., Done, C., & Smith, D. A., The 1989 May Outburst of the Soft X-ray Transient GS 2023+338 (V404 Cyg), *Monthly Notices of the Royal Astronomical Society*, 309, 561, 575, November 1999. doi: 10.1046/j.1365-8711.1999.02885.x url:http://ads.nao.ac.jp/abs/1999MNRAS.309..561Z